Modèles de filaments pour la natation à l'échelle microscopique

Jessie Levillain

INSTITUT POLYTECHNIQUE DE PARIS

NNT : 2024IPPAX056

Thèse de doctorat

Modèles de filaments pour la natation à l'échelle microscopique

Thèse de doctorat de l'Institut Polytechnique de Paris
préparée à École polytechnique

École doctorale n°574 Ecole Doctorale de Mathématiques Hadamard (EDMH)
Spécialité de doctorat : Mathématiques appliquées

Thèse présentée et soutenue à Palaiseau, le 27 septembre 2024, par

JESSIE LEVILLAIN

Composition du Jury :

Sébastien Martin Professeur des Universités, Université Paris-Cité (MAP5)	Président
Astrid Decoene Professeure des Universités, Université de Bordeaux (IMB)	Rapportrice
Céline Grandmont Directrice de recherche, INRIA Paris	Rapportrice
Josselin Garnier Professeur des Universités, École polytechnique (CMAP)	Examinateur
Laëtitia Giraldi Chargée de recherche, INRIA Sophia Antipolis	Examinatrice
François Alouges Professeur des Universités, ENS Paris-Saclay (Centre Borelli)	Directeur de thèse
Aline Lefebvre-Lepot Directrice de recherche, CNRS, Fédération de mathématiques de CentraleSupélec	Co-encadrante

ÉCOLE POLYTECHNIQUE, INSTITUT POLYTECHNIQUE DE PARIS

CENTRE DE MATHÉMATIQUES APPLIQUÉES POLYTECHNIQUE

Jessie Levillain

Modèles de filaments pour la natation à l'échelle microscopique

Thèse de doctorat

27 septembre 2024

Président	Sébastien Martin	Professeur des Universités
Rapportrice	Astrid Decoene	Professeure des Universités
Rapportrice	Céline Grandmont	Directrice de Recherche
Examinateur	Josselin Garnier	Professeur des Universités
Examinatrice	Laëtitia Giraldi	Chargée de recherche
Directeur de thèse	François Alouges	Professeur des universités
Co-encadrante	Aline Lefebvre-Lepot	Directrice de recherche

À ma grand-mère, Lisette.

Abstract

The mathematics associated with swimming at the microscopic scale has been an active research area for about fifteen years, with numerous applications in biology and physics. Indeed, microorganisms moving in water play a crucial role in the origin and maintenance of life, and the physical principles governing their movements differ greatly from those that govern human swimming. Research in this field can also be applied to the design of micro-robots, paving the way for innovative applications in medicine, such as non-invasive surgery.

This thesis deals with the study of such microorganisms in a context where inertial forces are negligible compared to viscous forces in the surrounding fluid, a phenomenon characterized by a low Reynolds number.

The first two parts present new mathematical models of swimmers, composed of active arms, spheres, and passive springs. These models circumvent Purcell's scallop theorem, which states that a swimmer doing a reciprocal stroke cannot move, as it always returns to its initial position in the absence of inertia. The first model developed in this thesis is a four-sphere swimmer with two passive elastic arms. By varying the oscillation frequency of the active arm, the direction of the swimmer's displacement can be changed, making the system controllable with only one active degree of freedom. The model studied in the second chapter involves a large number of springs. A limiting model of this swimmer, where the number of springs tends to infinity, was then considered, transforming the swimmer into an elastic tail that compresses and extends along one single dimension.

In the third chapter, a proof of the convergence and well-posedness of a discrete model of an elastic microfilament at low Reynolds numbers is presented. This model consists of N rigid filaments immersed in a fluid, studied in 3D and whose movement is in two dimensions.

Finally, in the last chapter, models of activation mechanisms along a flagellum are introduced. Biologically, these activation mechanisms exist in the flagellum in an internal structure called the axoneme, in the form of molecular motors arranged in several rows. Based on a model of these motors from biophysics, two new systems are then studied. The first one represents a projection of the axoneme with two rows of motors and is analyzed both theoretically and numerically. The second one takes into account all rows of motors in the axoneme; its behavior is illustrated by numerical simulations.

Résumé

Les mathématiques associées à la natation à l'échelle microscopique constituent un domaine de recherche actif depuis une quinzaine d'années, avec de nombreuses applications en biologie et en physique. En effet, les micro-organismes se déplaçant dans l'eau jouent un rôle crucial dans l'origine et le maintien de la vie, et les principes physiques régissant leurs mouvements diffèrent grandement de ceux qui gouvernent la natation humaine. Les recherches dans ce domaine peuvent aussi être appliquées à la conception de micro sous-marins, ouvrant la voie à des applications innovantes en médecine, comme la chirurgie non-invasive.

Cette thèse porte sur l'étude de tels micro-organismes, dans un contexte où les forces inertielles sont négligeables par rapport aux forces visqueuses dans le fluide environnant, phénomène caractérisé par un faible nombre de Reynolds.

Les deux premières parties traitent de modèles mathématiques de nageurs, composés de bras actifs, sphères, et ressorts passifs. Ces modèles permettent de contourner le théorème de la coquille Saint-Jacques de Purcell, qui garantit qu'un nageur dont la brassée est un mouvement réciproque ne pourra jamais se déplacer, car il revient toujours à sa position initiale en l'absence d'inertie. Le premier modèle conçu au cours de cette thèse est un nageur à quatre sphères avec deux bras élastiques passifs. Faire varier la fréquence d'oscillation du bras actif permet de changer le signe du déplacement du nageur, rendant le système contrôlable, tout en n'ayant qu'un seul degré de liberté actif. Le modèle étudié dans le deuxième chapitre comporte, quant à lui, un grand nombre de ressorts. Un modèle limite de ce nageur où le nombre de ressorts tend vers l'infini a ensuite été considéré, transformant le nageur en une queue élastique se compressant et s'étendant unidimensionnellement.

Au cours du troisième chapitre, on présente une preuve de la convergence et du caractère bien posé d'un modèle discret de micro-filament élastique à bas nombre de Reynolds. Ce modèle en trois dimensions est composé de N filaments rigides, dont le mouvement est en deux dimensions.

Enfin, dans le dernier chapitre, des modèles des mécanismes d'activation le long d'un flagelle sont présentés. Du point de vue de la biologie, ces mécanismes d'activation sont présents dans le flagelle dans une structure interne, appelée axonème, sous la forme de moteurs moléculaires arrangés en plusieurs rangées. En se basant sur un modèle de ces moteurs issu de la biophysique, deux nouveaux systèmes sont ensuite étudiés. Le premier représente une projection de l'axonème dans laquelle deux rangées de moteurs sont présentes, et est étudié aussi bien théoriquement que numériquement. Le second prend en compte la totalité des rangées de moteurs dans l'axonème, son comportement est illustré par des simulations numériques.

Remerciements

En premier lieu, je souhaite exprimer mon immense gratitude envers mes encadrants, François et Aline. François, je me suis embarquée avec toi dans cette aventure un peu folle, basée sur un seul mot, les "micro-nageurs", dont je ne soupçonnais même pas qu'on en fasse un domaine des mathématiques, et je le referais encore sans hésiter si l'on me posait la question aujourd'hui. Aline, merci pour ton sens de l'organisation, ton aide a été inestimable tout au long de ma thèse. Surtout, merci à tous les deux pour toutes les heures de travail et moments passés ensemble, pour votre disponibilité, et pour votre énorme soutien aussi bien scientifique que moral durant ces trois ans.

J'aimerais ensuite remercier l'ensemble de mon jury, merci tout d'abord à Astrid Decoene et Céline Grandmont d'avoir accepté de consacrer une partie de leur temps précieux à rapporter ma thèse. Merci à Josselin Garnier, Laëtitia Giraldi et Sébastien Martin d'avoir bien voulu me faire l'honneur de faire partie de mon jury. Laëtitia, merci pour toutes ces discussions que nous avons eues ensemble, en école d'été aussi bien que chez toi, à l'INRIA. Josselin, merci également de m'avoir épaulée au sein de mon comité de suivi et d'avoir rendue possible ma participation à des conférences incroyables.

J'aimerais également remercier toutes les personnes avec qui j'ai pu travailler, ou qui m'ont ouvert de nouvelles horizons scientifiques et culturelles en conférence. Je souhaiterais tout particulièrement adresser un mot à mes collaborateurs sur trois projets de recherche.

Grazie a Fabio Freschi per tante cose, per l'anno a Torino, per tutti i pasti insieme, per il tuo aiuto e le tue lettere negli ultimi 4 anni. Non vedo l'ora di lavorare di nuovo insieme. Grazie anche a Antonio DeSimone e Irene Anello, per avermi ospitata a Trieste, e per il bello lavoro insieme. Irene, maintenant que tu parles aussi français, *franchement*, je tiens à te remercier dans la langue de Molière. Merci pour ton soutien et pour tous ces mois passés ensemble, tu es devenue une amie précieuse.

Thank you Kenta Ishimoto for inviting me to Kyoto, for all your help and our precious discussions together. My thanks also to Ms. Maekawa for the care you took in organizing my time in Japan. Merci également à Clément Moreau sans qui tout cela n'aurait pas été possible, qui a été à l'origine de notre collaboration et avec qui j'ai eu grand plaisir à travailler. Clément, merci également pour tes précieux conseils au cours de ma thèse, tu as été pour moi comme un grand frère qui a su me guider et me rassurer.

J'aimerais ensuite remercier tous les membres du CMAP et en particulier toute les équipes administrative et informatique qui a permis le bon déroulement de ma thèse. Merci à Nasséra pour la bonne humeur à toute épreuve dont elle a su faire part lorsqu'elle résolvait mes nombreux problèmes administratifs, et à Aldjia et Gaël pour leur aide. Au sein de l'IPP j'aimerais également remercier Sylvie, Houda, Auriane et Anaïs pour leurs

conseils. Merci également à Mariella Argiolas et Suk-Hee Joo pour leurs enseignements respectifs en italien et en coréen.

Merci enfin à la grande famille des anciens et actuels doctorants du CMAP, si nombreux que je ne pourrais tous les citer, pour cette entraide constante au sein du laboratoire, par ordre alphabétique Adam, Adriano, Amanda, Ana, Baptiste, Benjamin, Christoph, Claire, Clément, Constantin, Grégoire, Jules, Leila, Loïc, Louis, Luce, Madeleine, Mano, Manon, Margherita, Marta, Orso, Oskar, Quentin mon petit frère de thèse, Raphaël, Richard, Solange, Vanessa, Wanqing. Mention spéciale à Dominik, grâce à qui j'ai pu me lancer dans cette thèse les yeux fermés, et à Guillaume et Antoine que j'ai taraudés au quotidien avec mes questions plus ou moins utiles, et ce n'est pas prêt d'en être fini (et si j'étais un ver de terre, est-ce qu'on serait toujours amis ??).

Plus personnellement, je voudrais remercier tous ceux qui ont pu m'accompagner, en dehors du monde académique, rencontrés pendant ou bien avant. Merci à mes amis de longue date, Charlène, Morgane, Quentin et Valentin. Une pensée également à la mémoire de Monsieur Cahour qui, à travers ses défis et nos paris, m'a donné goût aux mathématiques. Merci à tous mes amis de l'ENS, à travers les départements et les promotions, et à notre petit groupe du département de maths, Antoine et Antoine, Armand, que j'ai eu le plaisir de retrouver au CMAP (ha! Je ne t'avais pas oublié, le meilleur pour la fin), Clément, Luc, Matéo, Mickaël, Raymond et Simon. Merci également à toute la team des physiciens et chimistes, je ne vous citerai pas tous par peur d'en oublier. Merci à Benjamin, Jen, Lorenzo et Thomas pour les mardis au PPSM, et pour mes bureaux du jeudi, Charles au GEEPs puis Nicolas au LATMOS. Merci à mes partenaires de grimpe que je ne pourrais encore une fois tous nommer: à mes amies de BettyBeta et Girls in Bleau, à des rencontres improbables comme Manon, Mengmeng, Stefan et au Club Caillou notamment avec Arthur, Bastien, Jérôme, Juliette, Théo. Merci également à Prune pour sa motivation et son enthousiasme, et pour m'avoir nourrie dans les moments critiques !

Enfin, merci à Paul pour son amour et son investissement au quotidien, et à ma famille, à ma mère, mon père, mon frère, mes grands-parents.

Contents

List of Figures

List of Tables

1 *Introduction*

1.1 *Contexte de la micro-natation*

La natation à l'échelle microscopique est un sujet de recherche qui a de multiples retentissements dans plusieurs domaines des sciences. En biologie, bien sûr, puisque les micro-organismes capables de se déplacer dans l'eau (des bactéries qui peuplent notre système digestif, aux spermatozoïdes qui permettent la reproduction) sont à l'origine et au maintien de la vie, mais également en physique, ou les principes auxquels sont confrontés ces organismes sont bien différents de ceux qui gouvernent nos capacités humaines de natation. Les applications de ces recherches, outre la compréhension fine des aptitudes de déplacement de micro-organismes, permettraient également de concevoir des micro sous-marins, ouvrant la voie à de multiples utilisations novatrices en médecine, comme la chirurgie non-invasive. Quels mécanismes imaginer pour propulser un micro sous-marin le plus efficacement possible ? La nature répond à cette question de façons fort différentes. Les bactéries, telles que E. Coli sont équipées de plusieurs flagelles attachées à la cellule par le biais d'un véritable axe rotatif. Lorsque les flagelles tournent à l'unisson, ils s'organisent en une structure en forme de tire-bouchon qui propulse la bactérie. À l'inverse, les spermatozoïdes ont plutôt un flagelle qui se détend comme un fouet. Encore plus étrange, certaines micro-algues, comme Eutreptiella, illustrée en Figure 1.2, lorsqu'elles utilisent le mode appelé *metaboly* adoptent un mouvement ample de déformation qui peut faire penser à un nageur de brasse. Enfin, les mathématiques sous-jacentes aux nombreuses questions qui se posent dans ce domaine ont ouvert un champ de recherche devenu extrêmement actif depuis un peu moins d'une quinzaine d'années.

Figure 1.1. La micro algue Eutreptiella de la famille des Euglénoïdes. L'image est prise alors qu'elle effectue un mouvement de type "Metaboly" [99].

1.2 *Modélisation des nageurs*

1.2.1 *Environnement fluidique et concept de la brassée*

L'étude des nageurs de taille microscopique révèle de très nombreuses particularités et a fait l'objet de nombreux travaux depuis l'article de E. M. Purcell [87]. Tous ces nageurs, considérés comme des solides déformables, sont traditionnellement dans un milieu fluide $\mathcal{F} \subset \mathbb{R}^d$ ($d = 2,\ 3$) régi par l'équation de Navier-Stokes sur un intervalle de temps $[0, T]$ (pour $T > 0$)

$$\begin{cases} \rho(\partial_t u + (u \cdot \nabla)u) - \mu\Delta u + \nabla p = \rho f, \\ \text{div } u = 0, \end{cases} \tag{1.1}$$

où $\rho > 0$ est la densité du fluide considéré, $u : \mathcal{F} \times [0, T] \to \mathbb{R}^d$ sa vitesse d'écoulement, $p : \mathcal{F} \times [0, T] \to \mathbb{R}$ sa pression, $\mu > 0$ sa viscosité et $f : \mathcal{F} \times [0, T] \to \mathbb{R}^d$ les forces volumiques externes. Le flux du fluide dans ces équations provient ensuite soit de la force f qui est prescrite et non nulle, soit de conditions sur le bord $\partial\mathcal{F}$ adaptées.

Des paramètres de l'équation (1.1), on peut extraire une grandeur sans dimension appelée nombre de Reynolds, représentant le ratio des forces inertielles par rapport aux forces visqueuses dans le système étudié $Re = \frac{\rho u L}{\mu}$, avec L une longueur caractéristique du système. En particulier, pour un micro-nageur, dont la taille est de l'ordre de quelques micromètres, dans l'eau, Re est de l'ordre de 10^{-4} à 10^{-5}. Dans cette configuration, on considère alors que le système est dépourvu d'inertie ($Re \approx 0$) et on néglige les termes correspondants dans l'équation de Navier-Stokes, qui devient alors une équation linéaire, appelée équation de Stokes

$$\begin{cases} \mu\Delta u + \nabla p = \rho f, \\ \text{div } u = 0. \end{cases} \tag{1.2}$$

À cause de l'absence d'inertie à bas nombre de Reynolds et de la linéarité des équations de Stokes, les écoulements deviennent réversibles. Purcell est le premier à énoncer le "Théorème de la coquille Saint-Jacques", qui utilise cette réversibilité pour déduire l'impossibilité de la natation à cette échelle à l'aide de mouvements réciproques. La natation se définit alors en mathématiques, comme *avancer dans un fluide en se déformant de manière cyclique en l'absence de propulsion par des forces extérieures*. Chaque cycle de déformation s'appelle une brassée. Une brassée peut donc être caractérisée comme un chemin fermé γ dans l'espace des formes du nageur [61]. Pour que le nageur avance, il doit avoir un déplacement non nul sur une période, soit, si sa vitesse est désignée par $u = \dot{x}$:

$$0 \neq \Delta x = \int_0^\tau \dot{x}(t)dt \tag{1.3}$$

où $\tau > 0$ est la durée d'une brassée. Purcell propose également des dispositifs simples permettant de contourner le théorème, basés sur des brassées périodiques mais non réciproques. De nombreux autres concepts ont depuis été développés (voir [35], [77] par exemple), et fonctionnent souvent sur des principes biomimétiques (cf. Le PushMePul-

lYou d'Avron et al. [16]). Un grand nombre de modèles ont été regroupés dans l'article de revue [60]. Tous ces systèmes se caractérisent par l'utilisation de deux dispositifs de contrôle habilement utilisés de façon synchrones.

En parallèle, plusieurs résultats de nature mathématique, faisant le lien entre le problème de la natation et la théorie du contrôle [6], ont également permis de donner un autre éclairage, et d'exprimer les concepts sous-jacents (comme par exemple, "Est-ce que le mécanisme est capable de se propulser à faible nombre de Reynolds ?") en termes de crochets de Lie de champs de vecteurs décrivant la dynamique du nageur. Même les notions d'efficacité de la natation, qui apparaissent pour la première fois dans les ouvrages de Lighthill [64], ont un pendant qui s'exprime en termes de contrôle optimal. Les trajectoires optimales deviennent ainsi des géodésiques dans des espaces sous-riemanniens [2], [6]. Cette approche fournit également un cadre pour mieux comprendre les brassées optimales que doit réaliser le nageur lorsqu'il a plusieurs contrôles à sa disposition. Ces deux aspects seront principalement explorés dans les deux premiers chapitres, sur des modèles mathématiques de nageurs.

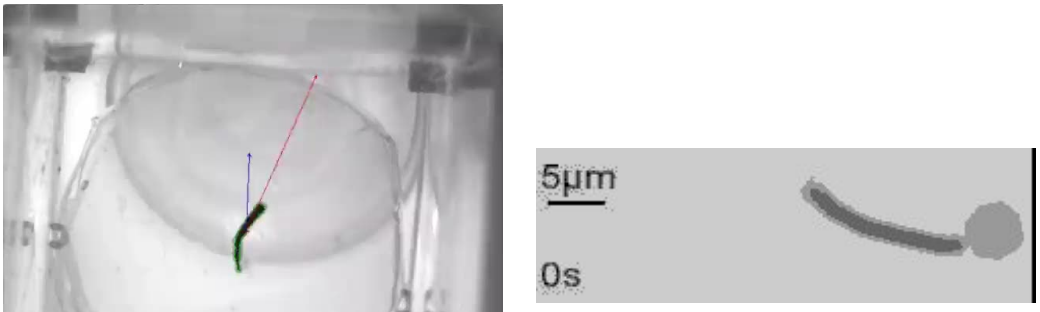

(a) **(b)**

Figure 1.2. (a) Un exemple de nageur magnéto-élastique réalisé dans l'équipe de S. Régnier. Il mesure quelques millimètres de long et est réalisé par impression 3D. Le milieu dans lequel il évolue, du silicone, assure le cadre à bas nombre de Reynolds. (b) Le nageur réalisé à l'ESPCI en 2005. La tête est un globule rouge et la queue (située à l'avant) est constituée de particules magnétiques reliées entre elles par des filaments d'ADN.

1.2.2 *Modèles mathématiques de nageurs*

Par la suite, on s'intéresse tout particulièrement aux micro-nageurs dotés de flagelles ou de bras, actifs ou passifs.

Dans le cas d'un cil ou d'un flagelle, on étudie en réalité un filament élastohydrodynamique. À faible nombre de Reynolds, les calculs mathématiques du mouvement et du déplacement de ces modèles de nageurs sont classiquement facilités par une théorie introduite par Gray et Hancock [46], appelée *Resistive Force Theory* (RFT). Cette approximation permet de relier la force de résistance hydrodynamique locale le long d'un filament du nageur à ses vitesses locales normales $e_n \cdot u$ et parallèles $e_t \cdot u$ via des

coefficients de friction normale $c_\perp$ et parallèle $c_\parallel$. On l'écrit généralement sous la forme, pour une tige de longueur L et $s \in [0, L]$

$$f(s) = -c_\perp(e_n \cdot u(s))e_n - c_\parallel(e_t \cdot u(s))e_t. \tag{1.4}$$

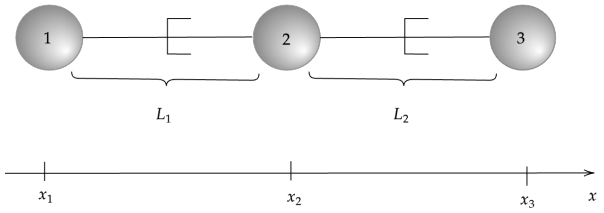

Figure 1.3. Nageur de A. Najafi et R. Golestanian à trois sphères. Chaque bras $i = 1, 2$ a une longueur $L_i(t)$ qui oscille en fonction du temps, et la position du centre de chaque sphère $j = 1, 2, 3$ est matérialisée par x_i le long de l'axe des x.

En ce qui concerne les modèles les plus simples et abstraits de nageurs en une dimension, on peut citer le nageur à trois sphères de A. Najafi et R. Golestanian [45], [77], illustré en Figure 1.3. Les trois sphères de rayon $a > 0$ de ce nageur sont reliées entre elles par deux bras extensibles de largeur négligeable, qui ont chacun un mouvement périodique prescrit L_i, et sont déphasés l'un par rapport à l'autre. Dans le cadre de ce nageur à trois sphères, on peut encore simplifier le calcul des équations de son mouvement, en considérant uniquement la résistance au fluide sur chacune des sphères. Les forces fluides $F = (F_i)_i$ appliquées sur chaque sphère et la vitesse des sphères $V = (V_i)_i$ sont ainsi reliées par ce qu'on appelle le tenseur d'Oseen [48], [81], contenant les *stokeslet*, solutions fondamentales de l'équation de Stokes (1.2). Comme l'éqaution de Stokes est linéaire, la relation entre F et V l'est également et on peut écrire $V = RF$ avec R que l'on appelle la matrice de résistance. Ici, dans l'approximation des petites variations $a/L_i \ll 1$, l'expression de R est simplifiée, elle est symétrique et $R_{ii} = \frac{1}{6\pi\mu a}$, tandis que $R_{ij} = \left(4\pi\mu \sum_{k=i}^{j-1} L_k\right)^{-1}$, pour $i \neq j$ [24]. Lorsqu'on regarde les brassées de ce nageur à trois sphères, on observe qu'elles forment des boucles d'aire non nulle dans l'espace des formes, grâce aux deux contrôles du système, ce qui permet d'avoir un déplacement du nageur à la fin d'une période.

E. Passov et Y. Or [83] ont ensuite déjoué cette hypothèse comme quoi une boucle d'aire non nulle ne pouvait être crée qu'avec aux moins deux contrôles en créant un nageur avec un seul degré de liberté actif. Pour cela, ils ont ajouté un lien élastique passif sur le premier nageur proposé par Purcell, comme décrit en Figure 1.4. Ils ont ainsi montré qu'un nageur avec un seul degré de liberté actif pouvait sortir du cadre du théorème de la coquille Saint-Jacques de Purcell. A. Montino et A. DeSimone [74] ont adapté ce concept au nageur à trois sphères, en remplaçant un des bras actifs de ce nageur par un élastique passif, qui se déphase naturellement d'une demie période par rapport à l'oscillation du bras actif, comme illustré en Figure 1.5.

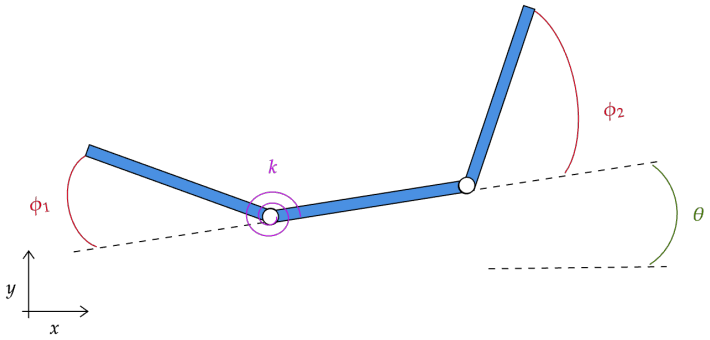

Figure 1.4. Nageur de Purcell [83] avec un lien élastique passif. Le nageur est composé de trois bras rigides, qui peuvent effectuer des rotations. Le bras de droite est ici considéré comme actif et a une rotation prescrite, tandis que celui de gauche réagit de manière passive au mouvement du nageur, grâce à un ressort de raideur k placé au niveau de la liaison pivot. Il se déphase naturellement par rapport à celui du bras actif, permettant ainsi au nageur d'avoir un mouvement périodique mais non réciproque.

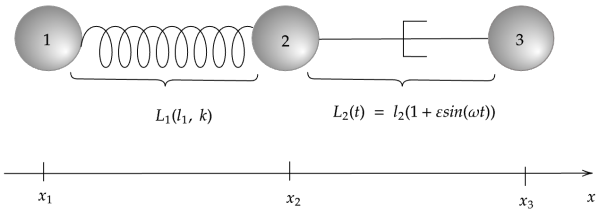

Figure 1.5. Nageur à trois sphères avec un bras élastique passif, comme présenté par Montino et DeSimone [74].

Cependant, on perd la contrôlabilité du nageur, qui ne peut plus avancer qu'avec le bras actif derrière. Plusieurs questions naturelles se posent ensuite, qui font l'objet des deux premiers chapitres de cette thèse. Tout d'abord, peut-on créer un nageur contrôlable avec un seul bras actif ? Ensuite, que se passe-t-il lorsque l'on rajoute plus de bras passifs ?

1.2.3 *Introduction à la biologie: structure des cils et flagelles*

Du côté expérimental, les travaux menés à l'ESPCI ([34], Figure 1.2(a)) ont permis, déjà depuis une quinzaine d'années, de construire des nageurs artificiels dont la taille n'excède pas quelques dizaines de microns. Plus récemment, les nageurs fabriqués par impression 3D par S. Régnier et son équipe ([37], [82], Figure 1.2(b)) ont considérablement simplifié la fabrication de ces micro-nageurs et ouvrent la voie à une réflexion approfondie sur la mise au point de mécanismes fonctionnels. Les dispositifs dans ces deux cas sont légèrement différents de ceux envisagés précédemment, puisque le nageur est propulsé par un champ magnétique extérieur. Ce champ agit sur le nageur en créant un couple magnétique qui déforme le nageur de façon non-réciproque, de façon à pouvoir créer un mouvement.

Les nageurs d'origine biologique, quant à eux, réussissent à se mouvoir et s'orienter sans être nécessairement propulsé par une force extérieure. On peut notamment observer que les cils et flagelles présentent tous un mouvement périodique caractéristique, leur permettant ainsi de nager aussi efficacement que possible dans un fluide visqueux. Afin de générer ce mouvement, une certaine forme d'activité interne le long du flagelle est nécessaire, comme l'a très tôt observé K. E. Machin [73]. Du point de vue de la biologie, cette activation est créée par une structure interne présente tout le long du flagelle, appelée axonème. Il est composé le plus souvent de neuf paires de microtubules, disposés en cylindre, et d'une paire centrale dans certains cas, comme illustré en Figure 1.6. En présence suffisante d'un composant chimique, l'AdénosineTriPhosphate (ATP),

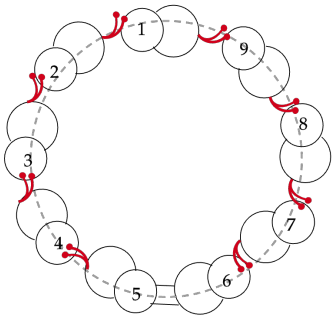

Figure 1.6. Vue en coupe simplifiée de la structure d'un axonème avec neuf paires de microtubules, sans paire centrale, avec un pont entre les doublets 5 et 6.

des moteurs moléculaires présents entre deux paires voisines de tubules fournissent un travail créant un glissement local entre elles, générant ainsi de la courbure le long du flagelle. Des liens de nexine, représentés par des ressorts de raideur $k > 0$ et reliant deux paires de tubules adjacentes entre elles, aident également à la création de cette courbure. Enfin, un pont reliant les doublets numérotés 5 et 6 est généralement présent, imposant ainsi un plan de battement préférentiel pour le flagelle.

Un modèle mathématique pour représenter un ensemble de moteurs se déplaçant le long d'un filament de période $\ell > 0$ a été présenté pour la première fois par F. Jülicher et J. Prost [57]. Il est basé sur deux hypothèses principales:

- ◇ Chaque moteur peut être seulement dans deux états; l'état 1 ou l'état 2. Lorsqu'il est dans un état i, il suit un potentiel physique W_i le long du filament, comme illustré en Figure 1.7. Le taux de transition d'un état i vers un état j est désigné par ω_i, qui dépend de la position du moteur ξ et de la quantité d'ATP, matérialisée par Ω;
- ◇ On s'intéresse à un grand nombre N de moteurs dans une cellule de périodicité de taille ℓ le long du filament, et on étudie la probabilité P de trouver le moteur dans l'état 1 au temps $t > 0$ et à la position $\xi \in [0, \ell]$.

Ce modèle s'écrit comme un système composé d'équations de réaction-convection et d'une équation intégro-différentielle provenant d'un bilan des forces sur le système

$$\begin{cases} \partial_t P(\xi,t) + v(t)\partial_\xi P(\xi,t) = -(\omega_1+\omega_2)P(\xi,t) + \omega_2/\ell \\ v(t) = \dfrac{1}{\eta}\left(\displaystyle\int_0^\ell d\xi P(\xi,t)\partial_\xi \Delta W(\xi) - kx(t)\right), \end{cases} \tag{1.5}$$

où $\omega_i = \omega_i(\xi;\Omega)$ et $\Delta W(\xi) = W_2(\xi) - W_1(\xi)$ et $v(t) = \dot{x}(t)$ représente la vitesse à laquelle se décale le filament du bas par rapport à celui du haut.

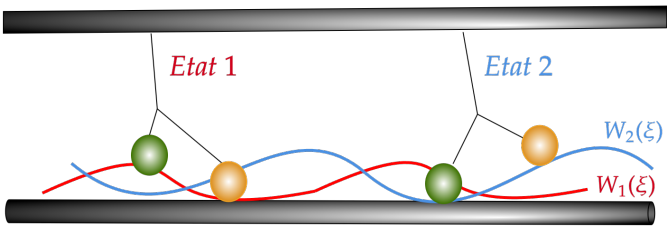

Figure 1.7. Moteurs moléculaire attachés à un filament par le haut, marchant sur un autre filament. Dans le cas du flagelle, ces moteurs sont des dynéines, comportant deux têtes qui s'attachent et se détachent alternativement du filament inférieur, créant ainsi cette "marche" à deux états.

Jülicher et Prost prédisent ensuite que, dans ce modèle, le système présente une bifurcation de Hopf qui dépend de Ω. Ainsi, il existerait un Ω_c critique en dessous duquel le système ne se mettrait pas en mouvement, et au dessus duquel il se mettrait à osciller.

1.3 *Synthèse des contributions de la thèse*

La thèse est divisée en quatre chapitres, organisés autour d'une problématique centrale, qui est de comprendre, modéliser et simuler efficacement le fonctionnement d'un micro-nageur flagellé, à toutes les échelles. Les deux premiers chapitres traitent de modèles mathématiques abstraits en une dimension, avec quelques questions d'optimisation des paramètres et de contrôlabilité. Le troisième porte sur un modèle discret de filament en trois dimensions, ayant un mouvement en deux dimensions. Il est plongé dans un fluide à bas nombre de Reynolds et on prouve la convergence du système d'équations qui le régissent vers celles d'un filament élastohydrodynamique continu. Dans le dernier chapitre, on s'intéressera aux mécanismes biologiques qui entretiennent la courbure d'un cil ou d'un flagelle, et à leur modélisation mathématique.

1.3.1 *Nageur bi-directionnel à deux bras passifs*

Le premier chapitre traite d'un nageur avec un seul bras actif L_2, entouré de deux ressorts L_1 et L_3, ayant chacun leur propre rigidité respective k_1 et k_3, illustré en haut de la Figure 1.8. Ce chapitre reproduit [63], soumis à *ESAIM Proceedings and Surveys*. De la même manière que dans les articles de référence [74], [77], mais cette fois-ci pour

un nageur à quatre sphères, on obtient le système d'équations différentielles ordinaires (EDO) régissant le mouvement et le déplacement du nageur en utilisant des bilans des forces bien choisis ainsi que des approximations liées à la RFT. Enfin, tout cela mène à une formule analytique explicite au premier ordre donnant le déplacement du nageur en fonction des paramètres du système, qui a pu être validée numériquement. En particulier, le cas d'intérêt de ce modèle est lorsque les deux rigidités sont différentes, $k_1 \neq k_3$. On peut ainsi observer qu'en fonction de la fréquence d'oscillation du bras actif, l'un ou l'autre des ressorts entre en résonance avec le bras, ce qui change le sens de déplacement du nageur, et permet donc de contrôler sa direction de propagation avec un seul contrôle.

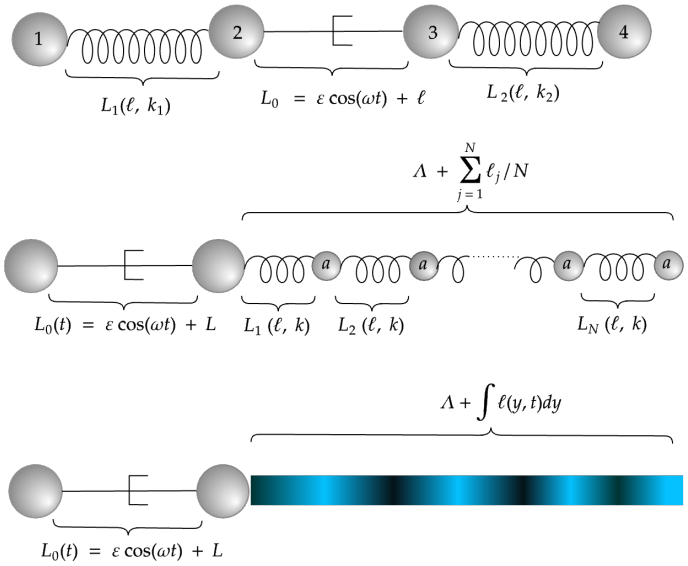

Figure 1.8. De haut en bas, trois modèles de nageurs avec un bras actif et un ou des bras passifs, qui se déplacent et bougent selon seulement une dimension: nageur à deux ressorts bi-directionnel, chaque ressort a une raideur différente (Chapitre 2); nageur à N ressorts et modèle limite de ce dernier, étudiés dans le Chapitre 3.

1.3.2 *Un modèle de nageur avec N bras passifs*

Dans le deuxième chapitre, qui reproduit [11] publié dans *AIMS Mathematics and Engineering*, on étudie cette fois-ci un nageur avec un nombre $N \in \mathbb{N}$ de ressorts (voir milieu de la Figure 1.8), et l'on cherche à trouver un modèle limite lorsque $N \to +\infty$. Ce nageur a une longueur fixe au repos $L + \Lambda$ indépendante de N, et un bras actif dont les caractéristiques ne dépendent pas non plus du nombre de ressorts, qui a un mouvement prescrit L_0. Tous les paramètres du système sont ensuite mis à l'échelle en fonction de N. Chaque bras passif L_i est ainsi défini pour $1 \leq i \leq N$ et $t \geq 0$ par $L_i(t) = \dfrac{\Lambda}{N} + \dfrac{\ell_i(t)}{N}$, avec $\dfrac{\ell_i(t)}{N}$ qui représente ainsi une petite variation de longueur. De même, pour un rayon caractéristique $\tilde{a}$ et une raideur caractéristique $\tilde{k}$ donnés, on définit

le rayon de chaque sphère $a = \tilde{a}/N$ et la raideur de chaque ressort $k = \tilde{k}N$. Ainsi, plus il y a de sphères et de bras passifs, plus la taille de ces deux dernier réduit, ce qui est compensé par la raideur des ressorts qui augmente. Dans ce modèle, l'ensemble des ressorts peuvent individuellement s'étendre et se rétracter, créant une oscillation en une dimension de la partie passive du nageur. Lorsque N augmente, on peut envisager un modèle limite du nageur, qui aurait toujours un bras actif, puis une sorte de flagelle passif qui se compresse et s'étend toujours en une seule dimension, que l'on désigne par la suite comme le "modèle continu", matérialisé en bas de la Figure 1.8.

On étudie également la dynamique et le déplacement à la fois du modèle à N ressorts, et de son modèle limite. Dans les deux cas, le nageur arrive à se déplacer, de la même manière que celui de Montino et DeSimone [74] dans une seule direction, mais l'onde de compression-dilatation des ressorts ne se propage pas efficacement le long du nageur, ce qui rejoint les observations de Machin [73] précédemment évoquées. Des mécanismes d'activation qui pourraient permettre la bonne propagation de cette onde sont présentés dans le dernier chapitre. Enfin, une preuve formelle de la convergence du nageur discret vers son pendant continu est présentée, basée sur l'étude du modèle discret comme une forme particulière de discrétisation éléments finis avec du *mass lumping* du modèle continu [88], [100]. Cette preuve constitue déjà un premier pas vers des schémas de discrétisation rapides et efficaces pour la simulation numérique d'un filament dans un fluide à bas Reynolds.

1.3.3 *Preuve de convergence d'une formulation semi-analytique discrète d'un filament à bas Reynolds*

Le troisième chapitre porte justement sur la convergence de modèles de filaments discrets, un article à ce sujet est en cours de rédaction. On peut y trouver de nombreuses applications concrètes pour les nageurs munis de flagelles ou de cils, ou encore les microtubules ou les faisceaux de filaments. Néanmoins, le couplage de l'élastodynamique d'un filament inextensible avec les interactions hydrodynamiques impliquant le fluide de Stokes environnant dans des simulations numériques soulève de nombreuses difficultés, en raison de divers facteurs tels que la non-linéarité géométrique, l'interaction fluide non locale ou la prise en compte de l'inextensibilité du filament. Dans la littérature, on retrouve à la fois des simulations utilisant des méthodes des éléments finis classiques, ainsi que des approches semi-analytiques, mais sans preuve de convergence. En particulier, on s'intéresse au modèle du nageur N-link [2], [44], [75], une méthode semi-analytique robuste, qui se comporte visuellement comme un filament élastohydrodynamique continu. Le nageur N-link est illustré en Figure 1.9, et comporte N segments rigides inextensibles qui bougent dans un plan. Au cours du temps, l'angle entre deux segments peut varier, ce qui change la forme du nageur et peut lui permettre de se déplacer.

L'objet de ce chapitre est double: tout d'abord, montrer que le système d'équations régissant le N-link est bien posé, puis prouver la convergence de ce modèle vers les équations d'un filament continu lorsque N tend vers l'infini. Les résultats sont démontrés pour plusieurs ensembles de conditions aux bords, permettant d'étudier un filament libre ou attaché à une tête.

Dans tout le chapitre, un résultat clé permet aux deux preuves d'aboutir. Il s'agit d'une loi de conservation de l'énergie dans le nageur qui, tout en garantissant la pertinence du modèle d'un point de vue de la physique, permet dans un premier temps d'inverser le système linéaire d'équations caractérisant le nageur, et donc d'appliquer le théorème de Cauchy-Lispchitz au problème. Pour la convergence, la preuve repose sur des interpolations bien choisies des quantités caractérisant le nageur, que l'on peut ensuite borner dans un espace garantissant une convergence et une régularité satisfaisante de la solution. Ces bornes s'obtiennent en partie grâce à l'estimation d'énergie précédemment mentionnée, mais aussi grâce au Lemme d'Aubin-Lions-Simon [14], [23], qui fournit un critère de compacité.

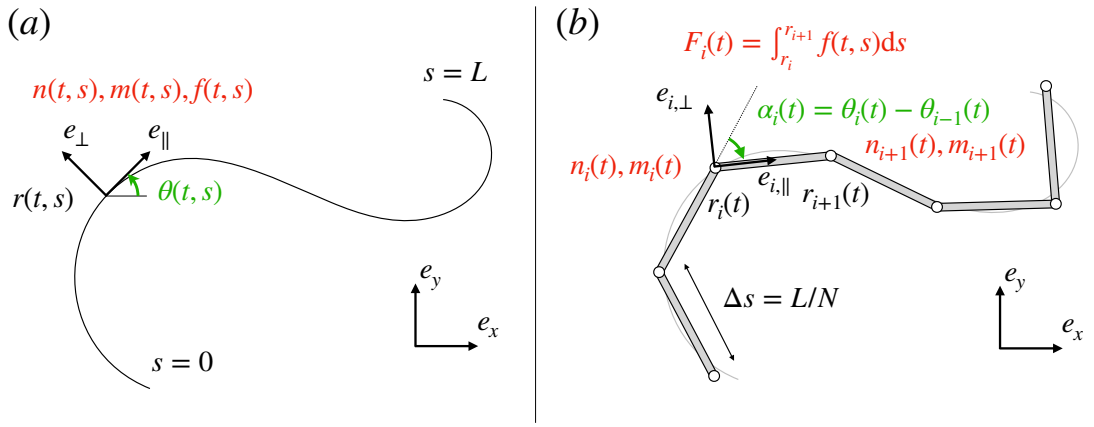

Figure 1.9. Diagramme et notations pour (a) un modèle de filament continu élastohydrodynamique à bas Reynolds et (b) le modèle du nageur N-link.

1.3.4 *Modèles mathématiques de mécanismes d'activation le long d'un flagelle*

Le dernier chapitre porte sur les mécanismes d'activation le long d'un flagelle, et leur modélisation mathématique. Un article regroupant les résultats du chapitre est en cours de rédaction. Tout d'abord, une étude détaillée du modèle de F. Jülicher et J. Prost, pour une rangée de moteurs moléculaires, est présentée. Des simulations numériques illustrent notamment les résultats annoncés dans les articles de référence [55]–[58], [86]: le système n'oscille qu'en présence de liens de nexine, et d'une quantité suffisante d'ATP. Des considérations concernant la pertinence des hypothèses simplificatrices usuelles du point de vue de la chimie du modèle sont également présentées en Section 5.8.2. Cependant, l'oscillation de la courbure créée par ce modèle a lieu autour d'une courbure

d'équilibre non nulle, ce qui va à l'encontre de ce que l'on peut observer en regardant le battement d'un flagelle.

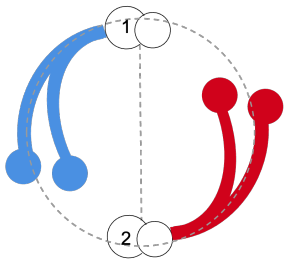

Figure 1.10. Modèle à deux couches, constituant une projection simplifiée de l'axonème. La rangée de moteurs attachée à la paire de tubules 1 marche sur la paire 2, et inversement.

Pour tenter de trouver une oscillation de la structure autour d'une courbure nulle, et afin de reproduire la structure cylindrique de l'axonème, un deuxième modèle est présenté. Il consiste en deux rangées de moteurs opposées l'une à l'autre, illustré par la Figure 1.10. Les précédentes simulations sont adaptées à ce modèle et une preuve formelle du caractère bien posé de ce modèle a été écrite. Nous avons également pu prouver, grâce au théorème de la variété centrale [106], que ce système à deux couches (et également le modèle de F. Jülicher et J. Prost) présentait une bifurcation de Hopf supercritique en fonction de la concentration en ATP.

Enfin, on introduit un dernier modèle avec N rangées de moteurs moléculaires, appelé modèle à N couches. N est arbitraire dans la partie théorique, mais lorsque l'on fixe $N = 8$, on étudie réellement un axonème à 9 paires de microtubules comme illustré en Figure 1.6. Pour le modèle N couches, des simulations numériques ainsi que des pistes pour une étude théorique sont présentées. On peut observer numériquement différents types de synchronisations spontanées entre les différentes couches, en fonction des conditions initiales choisies.

Qu'est-ce que le merveilleux ? Ce que nous ne comprenons pas.

Alexandre Dumas, Le Comte de Monte-Cristo

2 *A bi-directional low-Reynolds-number swimmer with passive elastic arms*

This chapter reproduces [63], written in collaboration with François Alouges, Antonio DeSimone, Akash Choudhary, Sankalp Nambiar and Ida Bochert, accepted for publication in the journal *ESAIM Proceedings and Surveys*.

2.1 *Introduction*

One of the many features of low-Reynolds-number swimming [20], [31], [95] is the *Scallop Theorem* stated by Purcell in his celebrated lecture [87], which forbids any net motion produced by *reciprocal* shape changes of the swimmer. Several mechanisms have been, since then, proposed to overcome the scallop theorem (see [60] and the many references therein), most of them using strategies to create non trivial loops, i.e. closed curves with non zero surface, in the shape space of the swimmer. Simple examples are given by the three link swimmer [87], the three sphere swimmer [77], the Push-Me-Pull-You [16] or Purcell's rotator [35]. All of these examples use two degrees of freedom in the shape activated periodically in time with a phase lag in order to produce the loop.

Furthermore, the efficiency of such systems has also been extensively studied in the literature, and we refer the interested to the examples given in [5], [10], [15], [97].

Strikingly, the constraint of having at least two degrees of freedom can be overcome, if one considers in the system, a passive elastic link. Indeed, the mechanism, discovered in [83], consists of a three-link swimmer with only one activatable joint, the other being a rotational spring. Due to hydrodynamic interactions, a periodic activation of the controlled parameter induces an out of phase periodic motion of the spring, permitting to describe a loop in the shape space. So far, two swimmers have been proposed in that direction: the three-link swimmer [83] and the three-sphere swimmer [74]. The latter, being an adaptation of the one proposed in [77], is simpler to analyze because, due to its rectilinear shape, no rotational movement is possible. A careful study, provided in [74] shows in particular that a displacement of the swimmer is possible depending on the frequency at which the actuated arm is deformed. At very low or very high frequency no net motion is possible after a stroke, while at a natural frequency of the system (which depends on the viscosity of the fluid, the masses and the spring constant)

a resonant effect takes place which provides an out of phase oscillation of the spring and, consequently, a net motion.

The present paper explores the situation where another spring is added to the system. The swimmer is therefore composed of four spheres linked by three arms, one of which being activated while the two remaining ones are springs. We particularly focus on the situation where the spring constants are different, leading to 2 natural frequencies of the system. We show that such systems can offer the interesting possibility of controlling the direction in which the swimmer moves with the frequency of the activated arm.

After recalling Montino and DeSimone's results on the three-sphere swimmer [74], we introduce a two-spring swimmer with a spring on each side of the actuated arm, and explore the consequences on its swimming motion and direction. We study its dynamics and displacement, depending on various system parameters.

2.2 *The 3-sphere Swimmer with a passive arm*

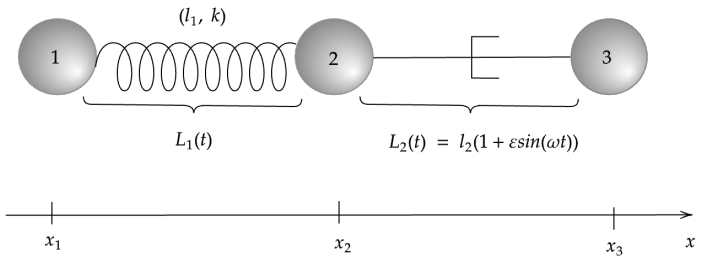

Figure 2.1. Three-sphere swimmer as proposed by Montino and DeSimone in [74]. Two spheres are connected by a spring with rest length l_1 and spring constant k. The third sphere is connected by an actuated arm. The distances between the spheres are given by $L_1(t)$ and $L_2(t)$.

Najafi and Golestanian created a swimmer consisting of three spheres, connected by two actuators [77]. By increasing and decreasing the length of the two actuators out of phase, the swimmer is able to perform a non-reciprocal motion providing a net displacement. Based on this, Montino and DeSimone proposed a three-sphere swimmer with a passive elastic arm [74] mimicking in this context, the mechanism of [83]. As shown in Figure 2.1, the first and second spheres are connected by a spring with spring constant k. The equilibrium length is denoted as l_1, the distance between the spheres is $L_1(t)$. The length of the actuated arm, which connects the second and third spheres, is given as $L_2(t)$. The radius of the spheres is a. For a periodic activation of $L_2(t)$ of the form

$$L_2(t) = l_2(1 + \varepsilon \sin(\omega t)), \tag{2.1}$$

the passive elastic arm experiences an out-of-phase oscillation, due to hydrodynamic interactions. The movement $L_1(t)$ can be calculated by considering elastic and hydrody-

namic forces. Indeed, assuming $\frac{a}{L_1} \sim \frac{a}{L_2} \ll 1$, the velocities v_i, $i = 1, 2, 3$ of the three spheres are related to the hydrodynamic forces in the following way

$$\begin{aligned} v_1 &= \frac{f_1}{6\pi\mu a} + \frac{f_2}{4\pi\mu L_1} + \frac{f_3}{4\pi\mu(L_1+L_2)}, \\ v_2 &= \frac{f_1}{4\pi\mu L_1} + \frac{f_2}{6\pi\mu a} + \frac{f_3}{4\pi\mu L_2}, \\ v_3 &= \frac{f_1}{4\pi\mu(L_1+L_2)} + \frac{f_2}{4\pi\mu L_2} + \frac{f_3}{6\pi\mu a}. \end{aligned}$$

Here, μ is the fluid viscosity and f_i describes the force, which is exerted on the fluid by the i-th sphere. The above set of equations can also be represented in the matrix form

$$V = RF \tag{2.2}$$

where $V = (v_1, v_2, v_3)^T$ is the vector of the velocities of the spheres and $F = (f_1, f_2, f_3)^T$ the vector of hydrodynamic forces acting on each sphere. The current structure of 3×3 mobility matrix R takes into account stokeslet interactions [17] by assuming that $a \ll L_i$, while self-interaction diagonal terms come from the hydrodynamic motion of a sphere in a fluid.

As it is the case in the low Reynolds number regime, inertial forces are neglected. Since there are no external forces considered, the force balance equation

$$f_1 + f_2 + f_3 = 0 \tag{2.3}$$

must be fulfilled. The elastic force $f_\mathrm{e} = k(L_1 - l_1)$ acting on the first sphere is equal and opposite to f_1 due to Newton's third law, leading to

$$f_1 = k(L_1 - l_1). \tag{2.4}$$

Furthermore, the velocities of the spheres and the lengths of the two arms are connected by

$$\dot{L}_1 = v_2 - v_1\,, \quad \dot{L}_2 = v_3 - v_2\,. \tag{2.5}$$

The time evolution of L_2 is controlled by the actuator as given in equation (2.1). The given system of equations (2.1- 2.5) can be solved to obtain $L_1(t)$ and $\dot{L}_1(t)$ and this calculation is done numerically in [74]. It can be observed that loops are formed in the configuration space (L_1, L_2). Since the displacement of a swimmer is proportional to the (algebraic) area enclosed by the curve in shape space, the three-sphere body is able to swim. Figure 2.2a shows the calculated curves in the shape space for different values of the actuating frequency ω. The other parameters are set to $l_1 = l_2 = 2 \cdot 10^{-4}\,\mathrm{m}$, $a = 0.1 \cdot 10^{-4}\,\mathrm{m}$, $\mu = 8.9 \cdot 10^{-4}\,\mathrm{Pa\,s}$, and $k = 10^{-7}\,\mathrm{N/m}$. It can be observed that the area enclosed by the blue curve (corresponding to an intermediate frequency) is larger than for the higher frequency (green curve) and for the lower frequency (red curve). This agrees with the qualitative study of [74], which states that the area enclosed by the curve

vanishes for $\Omega \to 0$ or $\Omega \to \infty$, where $\Omega = \omega\mu(l_1 + l_2)/k$ is a dimensionless frequency parameter.

From the resulting time evolution of $L_1(t)$ and $L_2(t)$, the position x_i of each sphere can be calculated from $\dot{x}_i = v_i$. The displacement of the swimmer $\Delta x(t) = \sum_i (x_i(t) - x_i(0))/3$ is shown in Figure 2.2b, with respect to the normalized time $t \cdot \omega/(2\pi)$. As it can be observed from the area in configuration space, the displacement of the swimmer after one period with intermediate frequency (blue) is larger than the one corresponding to a smaller (red) or higher frequency (green).

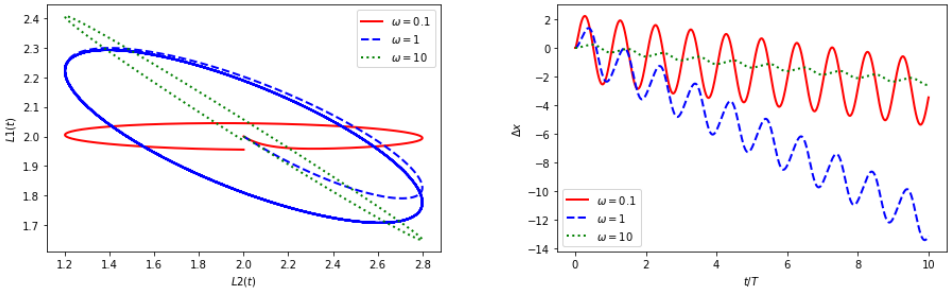

(a) **(b)**

Figure 2.2. Numerical results for Montino and DeSimone's three-sphere swimmer. (A) Curves in configuration space resulting from numerical solution of equations (2.1 - 2.5). The different colors correspond to different frequencies ω (in $\mathrm{rad\ s^{-1}}$) of the actuated arm. Note that the unit of length is 10^{-4} m. (B) Displacement Δx (in 10^{-4} m) of the three-sphere swimmer with respect to the normalized time $t/T = t \cdot \omega/(2\pi)$ for different actuating frequencies ω. [74]

It can be concluded that the three-sphere swimmer proposed by Montino and DeSimone is able to produce a net displacement depending on the dimensionless frequency Ω of the actuated arm. If Ω becomes too high or too low, the net displacement of the swimmer becomes smaller or eventually vanishes.

2.3 *The 4-sphere swimmer with two passive elastic arms*

Montino and DeSimone's swimmer [74] enabled us to circumvent the *Scallop Theorem* while only having one active degree of freedom in the system. However, this three-sphere swimmer can only swim in one direction. We now propose a new mechanism which, still with a single degree of freedom, is able to swim in both directions.

The swimmer is composed of 4 spheres where only the middle link serves as the active arm while the two others are passive springs as shown in Figure 2.3. In other words,

$$L_2 = l_2(1 + \varepsilon \sin(\omega t)), \tag{2.6}$$

and L_1, L_3 are the unknowns to be determined.

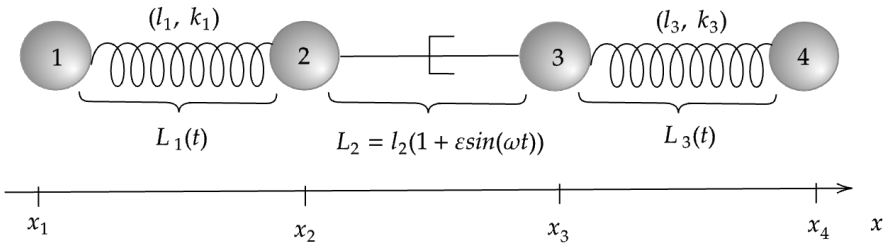

Figure 2.3. Four-sphere swimmer where the middle arm connecting spheres 2 and 3 is the activated part. Springs have rest lengths l_i and spring constants k_i. Distances between the spheres are given by $L_1(t)$, $L_2(t)$ and $L_3(t)$. In this case, the motion of the middle arm is prescribed as: $L_2 = l_2(1 + \varepsilon \sin(\omega t))$.

As in Section 2.2, we write down the equations for velocity v_i's of the four spheres similarly to [74]. This yields the following set of equations that govern the velocity of the spheres:

$$\begin{aligned}
v_1 &= \frac{f_1}{6\pi\mu a} + \frac{f_2}{4\pi\mu L_1} + \frac{f_3}{4\pi\mu(L_1+L_2)} + \frac{f_4}{4\pi\mu(L_1+L_2+L_3)},\\
v_2 &= \frac{f_1}{4\pi\mu L_1} + \frac{f_2}{6\pi\mu a} + \frac{f_3}{4\pi\mu L_2} + \frac{f_4}{4\pi\mu(L_2+L_3)},\\
v_3 &= \frac{f_1}{4\pi\mu(L_1+L_2)} + \frac{f_2}{4\pi\mu L_2} + \frac{f_3}{6\pi\mu a} + \frac{f_4}{4\pi\mu L_3},\\
v_4 &= \frac{f_1}{4\pi\mu(L_1+L_2+L_3)} + \frac{f_2}{4\pi\mu(L_2+L_3)} + \frac{f_3}{4\pi\mu L_3} + \frac{f_4}{6\pi\mu a},
\end{aligned}$$

that we again write in the abstract form

$$V = RF\,, \tag{2.8}$$

where $V = (v_1, v_2, v_3, v_4)^T$ is the vector of the velocities of the spheres and $F = (f_1, f_2, f_3, f_4)^T$ the vector of hydrodynamic forces acting on each sphere. Furthermore, the force-free condition becomes

$$f_1 + f_2 + f_3 + f_4 = 0. \tag{2.9}$$

and we can write the force balance law on spheres 1 and 4 as the balance between the viscous forces and the elastic forces of the arms:

$$f_1 = k_1\,(L_1 - l_1)\,, \qquad f_4 = -k_3\,(L_3 - l_3)\,. \tag{2.10}$$

and we observe that the rate of change of each of the links obeys

$$\dot{L}_i = v_{i+1} - v_i, \text{ for } i \in \{1,2,3\}\,. \tag{2.11}$$

The system (2.6 - 2.11) can be easily written as a differential-algebraic system of 11 equations with 11 unknowns. This system is then solved using standard numerical techniques.

2.3.1 *Computing net displacement over a period*

In the four-sphere swimmer described in our model, the net displacement of the swimmer after a periodic stroke can be computed as follows. Notice that the computation below does not involve the nature of the links (whether they are springs or rods). Calling X the position of the first sphere, V can be expressed linearly in terms of $\dot{X}$ and the rates of change of the arms' length $\dot{L}_i$ as

$$v_1 = \dot{X},\, v_2 = \dot{X} + \dot{L}_1,\, v_3 = \dot{X} + \dot{L}_1 + \dot{L}_2,\, v_4 = \dot{X} + \dot{L}_1 + \dot{L}_2 + \dot{L}_3\,,$$

that we rewrite in the matrix form as

$$V = M \begin{pmatrix} \dot{X} \\ \dot{L}_1 \\ \dot{L}_2 \\ \dot{L}_3 \end{pmatrix} \text{ with } M = \begin{pmatrix} 1 & 0 & 0 & 0 \\ 1 & 1 & 0 & 0 \\ 1 & 1 & 1 & 0 \\ 1 & 1 & 1 & 1 \end{pmatrix}.$$

Next, using $F = R^{-1}V$ and that the total force vanishes, provides us with a linear relationship between $\dot{X}$ and $\dot{L}_1, \dot{L}_2, \dot{L}_3$. Namely

$$\begin{pmatrix} 1 \\ 1 \\ 1 \\ 1 \end{pmatrix} \cdot R^{-1} M \begin{pmatrix} \dot{X} \\ \dot{L}_1 \\ \dot{L}_2 \\ \dot{L}_3 \end{pmatrix} = 0\,. \tag{2.12}$$

This is an equation that links $\dot{X}$ to $\dot{L}_1, \dot{L}_2, \dot{L}_3$ linearly, that we may rewrite under the form

$$\dot{X} = \xi(L) \cdot \dot{L}$$

where ξ is a 3-D vector field. Indeed, an expansion of $\xi(L)$ around the equilibrium solution $L_{eq} = (l_1, l_2, l_3)$ in the limit $a/l \ll 1$ with $l = \max(l_1, l_2, l_3)$ is obtained as follows. We first notice that, to first order

$$R^{-1} = 6\pi\mu a\,\mathrm{Id} - 9\pi\mu a \begin{pmatrix} 0 & \frac{a}{L_1} & \frac{a}{L_1+L_2} & \frac{a}{L_1+L_2+L_3} \\ \frac{a}{L_1} & 0 & \frac{a}{L_2} & \frac{a}{L_2+L_3} \\ \frac{a}{L_1+L_2} & \frac{a}{L_2} & 0 & \frac{a}{L_3} \\ \frac{a}{L_1+L_2+L_3} & \frac{a}{L_2+L_3} & \frac{a}{L_3} & 0 \end{pmatrix} + 6\pi\mu a\, O\left(\left(\frac{a}{l}\right)^2\right).$$

Simplifying by $6\pi\mu a$, we may thus rewrite (2.12) as

$$\alpha\dot{X} + \beta_1\dot{L}_1 + \beta_2\dot{L}_2 + \beta_3\dot{L}_3 = 0\,,$$

where

$$\begin{aligned}
\alpha &= 4 - \frac{3}{2}\left(\frac{2a}{L_1} + \frac{2a}{L_2} + \frac{2a}{L_3} + \frac{2a}{L_1+L_2} + \frac{2a}{L_2+L_3} + \frac{2a}{L_1+L_2+L_3}\right) + O\left(\left(\frac{a}{l}\right)^2\right),\\
\beta_1 &= 3 - \frac{3}{2}\left(\frac{a}{L_1} + \frac{2a}{L_2} + \frac{2a}{L_3} + \frac{a}{L_1+L_2} + \frac{2a}{L_2+L_3} + \frac{a}{L_1+L_2+L_3}\right) + O\left(\left(\frac{a}{l}\right)^2\right),\\
\beta_2 &= 2 - \frac{3}{2}\left(\frac{a}{L_2} + \frac{2a}{L_3} + \frac{a}{L_1+L_2} + \frac{a}{L_2+L_3} + \frac{a}{L_1+L_2+L_3}\right) + O\left(\left(\frac{a}{l}\right)^2\right),\\
\beta_3 &= 1 - \frac{3}{2}\left(\frac{a}{L_3} + \frac{a}{L_2+L_3} + \frac{a}{L_1+L_2+L_3}\right) + O\left(\left(\frac{a}{l}\right)^2\right),
\end{aligned}$$

from which we deduce that

$$\xi = -\frac{(\beta_1,\beta_2,\beta_3)^T}{\alpha} + O\left(\left(\frac{a}{l}\right)^2\right).$$

This leads to a formula for the coordinates of ξ, namely

$$\begin{aligned}
\xi_1 &= -\frac{3}{4} - \frac{3}{16}\left(\frac{a}{L_1} - \frac{a}{L_2} - \frac{a}{L_3} + \frac{a}{L_1+L_2} - \frac{a}{L_2+L_3} + \frac{a}{L_1+L_2+L_3}\right) + O\left(\left(\frac{a}{l}\right)^2\right),\\
\xi_2 &= -\frac{1}{2} - \frac{3}{8}\left(\frac{a}{L_1} - \frac{a}{L_3}\right) + O\left(\left(\frac{a}{l}\right)^2\right),\\
\xi_3 &= -\frac{1}{4} - \frac{3}{16}\left(\frac{a}{L_1} + \frac{a}{L_2} - \frac{a}{L_3} + \frac{a}{L_1+L_2} - \frac{a}{L_2+L_3} - \frac{a}{L_1+L_2+L_3}\right) + O\left(\left(\frac{a}{l}\right)^2\right),
\end{aligned}$$

Now, if we consider a closed stroke $L(t)$ in the shape space, the total displacement at the end of the stroke appears to be the circulation of ξ along the closed curve $L(t)$. In other words, using Stokes theorem

$$\Delta X = \oint_L \xi(L)\cdot dL = \int_\Sigma \mathrm{curl}(\xi)\cdot dS$$

where Σ is any surface that is bounded by the closed curve $L(t)$.

From the computation above, the leading term of curl(ξ) can be computed near $L = (l_1, l_2, l_3)$ and we obtain

$$\mathrm{curl}(\xi)(l_1,l_2,l_3) = \frac{3}{16}\begin{pmatrix} \frac{a}{l_2^2} + \frac{2a}{l_3^2} + \frac{a}{(l_1+l_2)^2} - \frac{a}{(l_2+l_3)^2} - \frac{a}{(l_1+l_2+l_3)^2} \\ -\frac{a}{l_1^2} - \frac{a}{l_3^2} - \frac{a}{(l_1+l_2)^2} - \frac{a}{(l_2+l_3)^2} + \frac{2a}{(l_1+l_2+l_3)^2} \\ \frac{2a}{l_1^2} + \frac{a}{l_2^2} - \frac{a}{(l_1+l_2)^2} + \frac{a}{(l_2+l_3)^2} - \frac{a}{(l_1+l_2+l_3)^2} \end{pmatrix} + O\left(\frac{a^2}{l^3}\right), \tag{2.13}$$

which enables us to compute an approximation of the displacement of the swimmer after a stroke around a given shape $L = (l_1, l_2, l_3)$. The validity of this expression to compute an approximation of the displacement after a stroke will be checked against the full integration of the system in the next Section.

2.3.2 *Numerical results: Swimming dynamics and displacement over time*

Numerical integration of the system (2.6 - 2.11) typically yields the 3D trajectories $(L_1(t),$ $L_2(t),$ $L_3(t))$ that are plotted in Figure 2.4. The flux of curl(ξ) through the areas enclosed by the limit cycles represents the displacement of the swimmer per unit cycle. All simulations are performed with reference parameters $l = l_1 = l_2 = l_3 = 2 \cdot 10^{-4}\,\mathrm{m}$, $a = 0.1 \cdot 10^{-4}\,\mathrm{m}$, $\mu = 8.9 \cdot 10^{-4}\,\mathrm{Pa\,s}$, $\varepsilon = 0.4$, $\omega = 1\,\mathrm{rad\,s^{-1}}$. As in Section 2.2, Figure 2.4(A) shows the behavior of the system when $k_1 = 0.1k_3 = 10^{-7}\,\mathrm{N\,m^{-1}}$, and for $\omega = 0.1$, 1, and 10. As expected, a periodic limit cycle is quickly obtained whose orientation changes with ω. As for the swimmer of the previous section, there exists an optimal frequency that provides the highest displacement per unit cycle, while for very low or high frequencies the area enclosed by the cycle tends to 0.

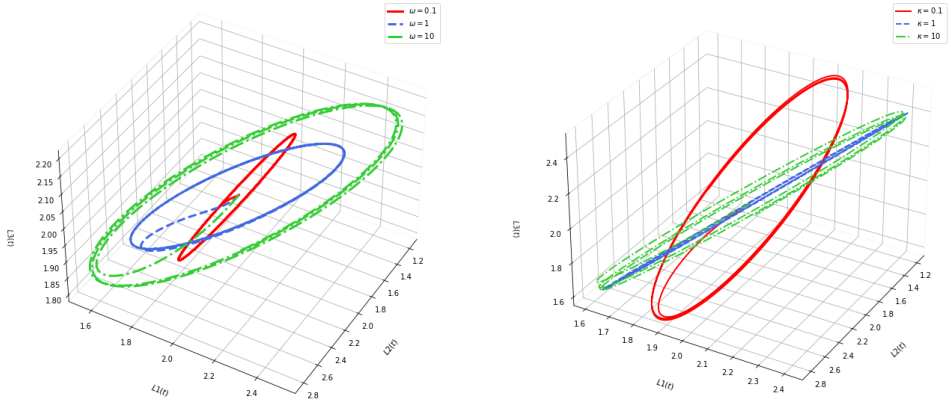

(a) **(b)**

Figure 2.4. Three dimensional trajectories of the four-sphere swimmer depicting limit cycles. (A) Effect of various frequencies ω (in $\mathrm{rad\,s^{-1}}$) for a fixed $\kappa = 10$. (B) Effect of stiffness ratio $\kappa = k_3/k_1$ for a fixed $\omega = 1\,\mathrm{rad\,s^{-1}}$.

In Figure 2.4(B), we fix the frequency $\omega = 1$ and vary the stiffness of the second link relative to the first link. Here $k_3 = 1 \cdot 10^{-7}\,\mathrm{N\,m^{-1}}$ while $k_1 = 0.1k_3, k_3$ and $10\,k_3$, characterized by the stiffness ratio $\kappa = k_3/k_1$. We observe that, although the areas enclosed by the trajectories remain similar, their orientation varies depending on κ. This can be expected since, when one spring is stiffer than the other one, phase lag will differ and one side of the swimmer will thus start moving before the other one. This influences the swimming direction of our model, which is then illustrated when computing the displacement. Lastly, we can notice that the area enclosed by the curve when $\kappa = 1$ is nonzero, although the swimmer does not have any net displacement, as shown later on in Figure 2.7, which seems unusual. This can be nevertheless explained. Indeed, when $\kappa = 1$, the swimmer is completely symmetric, falling in the case of the *Scallop Theorem*

once again. However, since there is still a phase lag between the springs and the active arm, the global length at which the swimmer starts each stroke can vary, explaining the nonzero surface bounded by the curve in the shape space.

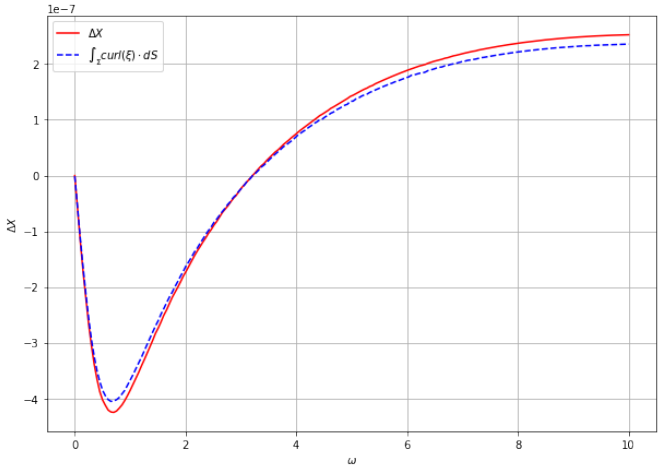

Figure 2.5. Average displacement per period (ΔX, in m) of the swimmer computed directly by integration (in red) and using the circulation of the first-order approximation (2.13) of curl(ξ) (in blue), plotted as a function of ω (in $rad\, s^{-1}$), for $\varepsilon = 0.3$.

We calculate the net displacement over a periodic stroke by integrating the average velocity of the spheres in the permanent regime, i.e. when the initial transient is terminated. Figure 2.5 shows both the approximation of the displacement computed using the formula $\Delta X = \oint_L \xi(L) \cdot dL = \int_\Sigma \text{curl}(\xi) \cdot dS$ with the first-order expansion of curl(ξ) given in (2.13), and the integration of $\dot{X}$ giving the exact displacement per period. Here, $a/\ell = 0.05$ and $\varepsilon = 0.3$, and we notice very a very small difference of about 5% between the approximation with the numerical integration of the system over a wide range of frequencies.

In Figure 2.6, we plot the swimmer's displacement as a function of time, in the permanent regime, when $\kappa = k_3/k_1 = 10$ and when $\kappa = 0.1$, for $\omega = \{0.1, 1, 10\}$ rad s^{-1}. The swimmer exhibits different behaviors depending on the frequency, namely, its efficiency varies and, more importantly the direction of the motion changes.

To understand the variation of the swimmer displacement with the frequency, we plot in Figure 2.7, the average (renormalized) displacement per period $\Delta X/l$, as a function of ω. Roughly speaking, the plot segregates two regimes that are separated by the $\kappa = 1$ curve. In this latter situation, as we have already mentioned, both springs are synchronized with the same amplitude due to the symmetry of the system. Thus, the swimmer undergoes a reciprocal shape change and no displacement can be observed. For $\kappa > 1$, $\Delta X/l$ has a positive maximum first, followed by a negative minimum, and conversely for $\kappa < 1$. The average displacement per period approaches to zero as $\omega \to 0$ and $\omega \to \infty$ [74]. The maxima/minima of the curves imply a characteristic resonant behavior where the displacement is maximum for a given frequency.

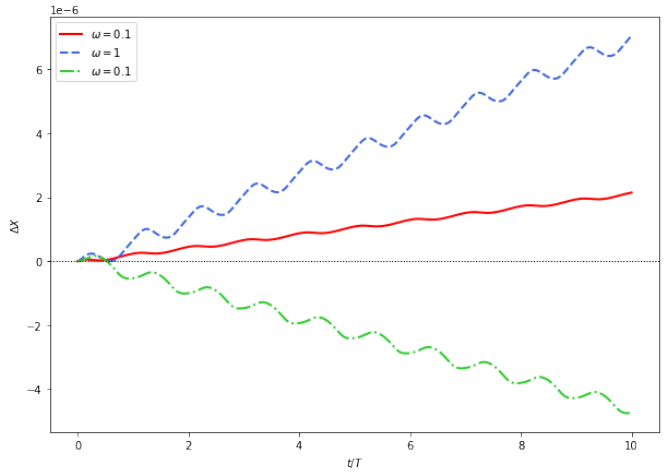

Figure 2.6. The swimmer's displacement ΔX (in m) plotted as a function of normalized time $t/T = t \cdot \omega/(2\pi)$ for $\kappa = 0.1$ and various ω.

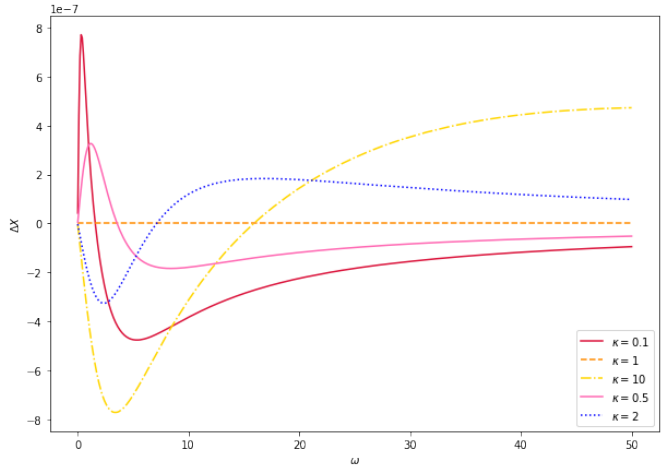

Figure 2.7. Average displacement per period (ΔX, in m) of the swimmer, plotted as a function of ω (in $rad\, s^{-1}$) for various κ.

Now, consider the case of $\kappa = 0.1$ in Figure 2.7. The displacement over one stroke ΔX is maximum at $\omega \approx 0.5\,\mathrm{rad\ s^{-1}}$ and minimum for $\omega \approx 5\,\mathrm{rad\ s^{-1}}$. Therefore, when the right spring is much stiffer than the left spring, $k_3 \gg k_1$, the swimmer moves to the right for small frequencies and moves to the left for moderate frequencies. As k_3 reduces and approaches k_1, both extrema of ΔX reduce in magnitude and shift to larger frequencies. For $k_1 = k_3$, there is no displacement. For $k_1 > k_3$ the scenario is opposite with the minima of larger magnitude appearing first followed by the maxima of smaller amplitude.

2.4 *Conclusion*

We have proposed and studied the dynamics of a four-sphere swimmer with two passive elastic arms, activated by a central link that elongates and retracts periodically with

amplitude ε and angular frequency ω. Thanks to interactions between elastic and hydrodynamic forces, a phase difference between the oscillations of the active arm and each spring is created, which value depends on the springs' stiffness. When those are different, it gives rise to a large range of frequencies at which the swimmer moves with high efficiency. This phase differences enables the model to undergo non-reciprocal shape changes, thus circumventing the Scallop Theorem's obstruction [87].

Moreover, since there are two springs with different stiffnesses on each side of the activated arm, depending on the driving frequency, the system undergoes a different behavior. Indeed, playing with the oscillation frequency of the active arm can change the system's swimming direction, contrarily to what was shown in earlier works [74]. This paves the way for controlling complex trajectories with simple artificial micro-swimmers composed of spheres as in [8], [9], [12].

J'arrive dans les bacs comme Jean-Sébastien
N***e la BAC ils ont saisi ma pof
Moi j'aime les bacs quand ils sont dans mes mains
À la fac j'vais d'venir prof

EL Pelo, EP Kinésithérappeur, "J'arrive dans les bacs"

3 *A limiting model for a low-Reynolds number swimmer with N passive elastic arms*

This chapter reproduces [11], written in collaboration with François Alouges and Aline Lefebvre-Lepot, published in 2023 in the journal *AIMS Press Mathematics in Engineering*.

3.1 *Introduction*

As stated by Purcell's *Scallop Theorem* [87], reciprocal shape changes in a swimmer never leads to a net displacement of the system in a low Reynolds number setting. Indeed, a microscopic scallop opening and closing its valve would be completely unable to swim, due to negligible inertial forces in this situation [31]. Several simple mechanisms have then been introduced (see e.g. [60]) to overcome this obstruction, most of them using two degrees of freedom in order to create closed curves with nonzero surface in the shape space of the swimmer.

One of the simplest mechanisms introduced in the literature is probably Najafi and Golestanian's three-sphere swimmer [77], which consists in three spheres linked by two extensible arms of negligible thickness, moving along a single direction. This model is much simpler than Purcell's original three-link swimmer [87], or Purcell's rotator [35], as there is no rotational motion involved. This swimmer has two degrees of freedom, activated periodically in time with a phase lag in order to produce the loop. Both Purcell's and Najafi and Golestanian's swimmers have been extensively studied in [4]–[7], [10], [33].

As an extension of this three-sphere swimmer, Montino and DeSimone then introduced a three-sphere swimmer with a passive elastic arm [74]. This adaptation has only one degree of freedom, which is the length of the non-elastic arm. Thanks to a resonant effect at natural frequency of the system (which depends on the viscosity of the fluid, the masses and the spring constant), an out-of-phase oscillation of the spring is created, which ultimately leads to a net motion of the swimmer. However, at very low or very high frequency, no net motion is possible after a stroke. Having this passive elastic arm also confines net motion to only one direction on the swimming axis, swimming direction is thus limited, and the swimmer can only move with its passive arm ahead. This was also denoted by Passov [83], when looking at Purcell's three-link swimmer with a passive elastic tail.

In this paper, Montino and DeSimone's swimmer is extended by adding a large number N of passive elastic arms to their one-dimensional swimmer, thus turning it into an $(N+2)$-sphere swimmer. This simple swimmer then leads to a limit model with an elastic tail resembling a one-dimensional flagella along which compressive waves propagate.

The paper is organized as follows. In sect. 3.2, we describe the N-spring swimmer, and its equations of motion, before looking at the limit model, when the number of springs tends to infinity, in sect. 3.2.3. We prove the convergence of the discrete model to the continuous one in sect. 3.3, using the fact that it is found to be a non-conventional mass lumping discretization of the limit model. Sect. 3.4 introduces two formulas in order to compute the net displacement of both swimmers, discrete and continuous. Finally, in sect. 3.5 we study numerically the movement and displacement of our swimmer depending on various system parameters, in order to find optimal swimming parameters to obtain the largest net displacement possible.

3.2 *Problem formulation and study: N-spring discrete model and its continuous limit*

The swimmer studied in this paper is an extension of the three-sphere swimmer with a single passive elastic arm [74], to a swimmer with $N+2$ spheres and N passive elastic arms, presented in figure 3.1. The first arm of this artificial swimmer is a rod of negligible thickness, surrounded by two spheres of radius a_1. This arm has a prescribed periodic movement around a length at rest L, of the form $L_0(t) = L(1+\tilde{\varepsilon}\cos(\omega t))$ where $\tilde{\varepsilon} \in [0,1)$ is a non-dimensional parameter. $\tilde{\varepsilon} < 1$ so that the active arm always has a positive length. We define ε as $\varepsilon = L\tilde{\varepsilon}$. The rest of the swimmer has a total length at rest Λ that does not depend on N. In order to keep a constant length and have an elastic force that does not depend on N, all the other spheres have a radius $a = \tilde{a}/N$, the springs have each a rest length $h = \Lambda/N \gg a$, and an elastic constant $k = \tilde{k}N$, with $\tilde{k}$ and $\tilde{a}$ prescribed and independent of N.

If the swimmer is able to control the length of the front rod with the prescribed periodic function $L_0(t)$, the length of the N remaining springs are governed by the balance of viscous and elastic forces. At any time t, the length $L_j(t)$ of the j-th arm, $j \geq 1$ is written as $L_j(t) = \frac{\ell_j(t)}{N} + h$. Let us then denote by μ the fluid viscosity, f_j^F and f_j^R the hydrodynamic and elastic forces on the j-th sphere. We also call x_j the coordinate of its center, so that $V_j = \dot{x}_j$ is the velocity of the j-th sphere. The geometry of the system entails $\dot{L}_j = V_{j+2} - V_{j+1}$ for all $j = 0, \ldots, N$.

In order to effectively swim, our N-spring swimmer undergoes periodic harmonic but non-reversible deformations, just like the original swimmers from Najafi and Golestanian [77], and Montino and DeSimone [74]. However, due to the geometry, we expect a wave to propagate along the tail. This is the behaviour of this wave that we aim at describing in the remainder of the paper.

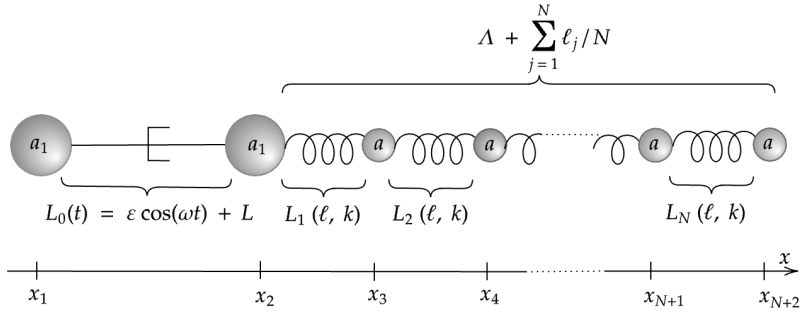

Figure 3.1. Low Reynolds number swimmer with N elastic arms.

3.2.1 *First approximations*

In a first approximation, we consider the case where the hydrodynamic force on the j-th sphere only depends on the speed of that same sphere, and neglect interactions between spheres. This leads to the following set of equations on (fluid) forces and velocities:

$$\begin{cases} f_j^F = -6\pi\mu a V_j \text{ for } j \geq 3, \\ f_j^F = -6\pi\mu a_1 V_j \text{ for } j = 1, 2. \end{cases} \tag{3.1}$$

The elastic forces on each sphere can be written as:

$$\begin{cases} f_2^R &= k(L_1 - h) = k\dfrac{\ell_1}{N} \\ f_j^R &= k\big((L_{j-1} - h) - (L_{j-2} - h)\big), \\ &= k\dfrac{\ell_{j-1} - \ell_{j-2}}{N} \quad \text{for } 3 \leq j \leq N+1 \\ f_{N+2}^R &= -k(L_N - h) = -k\dfrac{\ell_N}{N}. \end{cases} \tag{3.2}$$

At low Reynolds number, inertial forces are negligible. This, together with the fact that the artificial swimmer is self-propelled, gives:

$$\begin{cases} f_1^F + \cdots + f_{N+2}^F = 0, \\ f_j^R + f_j^F = 0 \text{ for } j \geq 3. \end{cases} \tag{3.3}$$

Using (3.1), (3.2) and (3.3), we obtain the expression of fluid forces on each sphere with respect to the length of the adjacent arms. In particular, for the first two spheres:

$$\begin{cases} f_1^F - f_2^F = 6\pi\mu a_1(V_2 - V_1) = 6\pi\mu a_1 \dot{L}_0, \\ f_1^F + f_2^F = f_3^R + \cdots + f_{N+2}^R = -k\ell_1/N, \end{cases} \tag{3.4}$$

which finally leads to:

$$\begin{cases} f_1^F = \frac{1}{2}(+6\pi\mu a_1 \dot{L}_0 - \tilde{k}\ell_1), \\ f_2^F = \frac{1}{2}(-6\pi\mu a_1 \dot{L}_0 - \tilde{k}\ell_1). \end{cases} \tag{3.5}$$

3.2.2 *Movement of the spheres*

In order to write the equations governing the system, we use equations (3.1-3.5) to find ODEs on the elongation $l_j(t)$ of the j-th arm, for $j \geq 1$. We first consider the case $j \geq 2$. Writing $\dot{L}_j = V_{j+2} - V_{j+1} = \frac{1}{6\pi\mu a}(f_{j+2}^R - f_{j+1}^R)$, one deduces

$$\dot{\ell}_j = \Lambda^2 K \frac{\ell_{j-1} - 2\ell_j + \ell_{j+1}}{h^2}, \; 2 \leq j \leq N, \tag{3.6}$$

where we have added a fictitious variable

$$\ell_{N+1} = 0\,, \tag{3.7}$$

and with $K = \dfrac{\tilde{k}}{6\pi\mu\tilde{a}}$.

To determine the equation for the first elastic arm, we use the fact that $\dot{L}_1 = V_3 - V_2 = -\dfrac{1}{6\pi\mu a} f_3^F + \dfrac{1}{6\pi\mu a_1} f_2^F$ to obtain, using equations (3.2) and (3.5):

$$h\dot{\ell}_1 = \Lambda^2 K \frac{\ell_2 - \ell_1}{h} - \frac{\Lambda K \tilde{a}}{2a_1}\ell_1 - \frac{\Lambda}{2}\dot{L}_0. \tag{3.8}$$

We can easily verify that the ODE problem (3.6,3.7,3.8) is well-posed using Cauchy-Lipschitz theorem, and provides a unique solution $(\ell_j(t))_{1\leq j\leq N+1}$ for any initial configuration.

Seeking for periodic (complex) solutions to equation (3.6) leads to

$$\ell_j(t) = (\alpha_d \gamma_+^{j-1} + \beta_d \gamma_-^{j-1}) e^{i\omega t}, \tag{3.9}$$

where $\alpha_d, \beta_d \in \mathbb{C}$ and

$$\gamma_\pm = \frac{i/(K_\omega N^2) + 2 \pm \sqrt{\Delta}}{2} \tag{3.10}$$

and $\Delta = \dfrac{-1}{K_\omega^2 N^4} + \dfrac{4i}{K_\omega N^2}$, where $K_\omega = \dfrac{K}{\omega} = \dfrac{\tilde{k}}{6\pi\mu\tilde{a}\omega}$ is an adimensional number. Notice that $|\gamma_+| > 1$ while $|\gamma_-| < 1$. The constants α_d and β_d may be determined through the boundary conditions. Namely assuming, from the linearity of the problem, $\ell_1 = b_d e^{i\omega t}$, with $b_d \in \mathbb{C}$ and recalling $l_{N+1} = 0$ enables us to write

$$\begin{cases} \ell_1(t) = b_d e^{i\omega t} = e^{i\omega t}(\alpha_d + \beta_d), \\ \ell_{N+1}(t) = e^{i\omega t}(\alpha_d \gamma_+^N + \beta_d \gamma_-^N) = 0\,, \end{cases} \tag{3.11}$$

to finally obtain

$$\alpha_d = \frac{-\gamma_-^N b_d}{(\gamma_+^N - \gamma_-^N)}, \quad \beta_d = \frac{\gamma_+^N b_d}{(\gamma_+^N - \gamma_-^N)}. \tag{3.12}$$

Then, we use (3.8) to determine b_d:

$$b_d = -\frac{\varepsilon i/2}{i/N + NK_\omega(1 - z_d) + K_\omega \dfrac{\tilde{a}}{2a_1}}, \tag{3.13}$$

where $z_d = \dfrac{\gamma_+^N \gamma_- - \gamma_-^N \gamma_+}{\gamma_+^N - \gamma_-^N}$.

3.2.3 *Limit model with an infinite number of springs*

As we increase the number of springs in our swimmer, a limit model arises, with an elastic-like tail, as shown in figure 3.2. This elastic tail compresses and dilates itself in the same way that the springs do, following the active arm, in order to create a global displacement of our swimmer.

Equations (3.6) and (3.8) can be viewed as a finite element discretization of a PDE, which describes the continuous version of our swimmer. Limit expressions for this PDE model are formally derived throughout this section while the convergence of the N-spring model to the continuous model will be proven in Sect. 3.3.

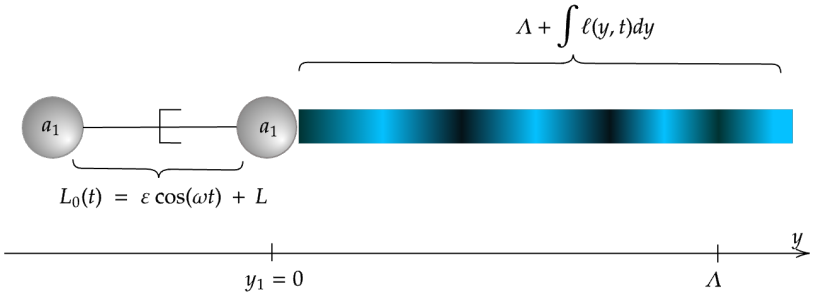

Figure 3.2. Continuous model of the low-Reynolds-number elastic swimmer. Color variations in the tail indicate compression and expansion of the swimmer.

First, as $h \to 0$ ($N \to \infty$), $\dfrac{\ell_{j-1} - 2\ell_j + \ell_{j+1}}{h^2}$ formally converges to a second order derivative. More precisely, we introduce a new space variable $y_j = (j-1)h$ for $1 \leq j \leq N+1$. The points y_j are equally spaced and thus different from the previous x_j. Since $y_1 = 0$, the y variable can be seen as a local space coordinate attached to the second sphere, and we assume $\ell(y_j) = \ell_j$ for a smooth enough function ℓ. Passing to the formal limit in (3.6) leads to a heat equation:

$$\partial_t \ell(y,t) = K\Lambda^2 \partial_{yy}\ell(y,t), \quad \forall (y,t) \in [0,\Lambda] \times \mathbb{R}_+^\star. \tag{3.14}$$

Concerning the boundary conditions, we first notice that $\ell_{N+1} = 0$ leads to $\ell(\Lambda, t) = 0$ for all $t > 0$. As $h \to 0$, the equation (3.8) on ℓ_1 formally becomes a Fourier-type boundary condition:

$$\Lambda^2 K \partial_y \ell(0,t) - \Lambda K \frac{\tilde{a}}{2a_1}\ell(0,t) = \frac{\Lambda}{2}\dot{L}_0(t), \quad \forall t > 0.$$

Therefore, we finally obtain the following continuous problem:
Find $\ell \in \mathcal{C}^2([0,\Lambda] \times \mathbb{R}_+^*)$ such that $\forall (y,t) \in (0,\Lambda) \times \mathbb{R}_+^\star$,

$$\begin{cases} \partial_t \ell(y,t) - \Lambda^2 K \partial_{yy}\ell(y,t) = 0, \\ \Lambda^2 K \partial_y \ell(0,t) - \Lambda K \dfrac{\tilde{a}}{2a_1}\ell(0,t) = \dfrac{\Lambda}{2}\dot{L}_0(t), \\ \ell(\Lambda,t) = 0. \end{cases} \tag{3.15}$$

3.2.4 *Well-posedness of the problem*

Equation (3.15) belongs to the class of problem for which the classical theory of parabolic equations applies. Namely, calling

$$\mathcal{V} = \left\{ u \in H^1((0,\Lambda)) | u(\Lambda) = 0 \right\},$$

which is a Hilbert space with the scalar product $(u,v)_{\mathcal{V}} = \int_0^\Lambda \partial_y u \, \partial_y v \, dy$, the variational formulation reads:

Let $T > 0$, find $\ell(y,t) \in L_t^\infty(0,T; L_y^2((0,\Lambda))) \cap L_t^2(0,T;\mathcal{V})$ such that for all $t \in (0,T)$ and for all $v \in \mathcal{V}$

$$\begin{aligned} \frac{d}{dt}\int_0^\Lambda \ell v \, dy + \Lambda^2 K \int_0^\Lambda \partial_y \ell \, \partial_y v \, dy \\ + \frac{\Lambda K \tilde{a}}{2a_1}\ell(0,t)v(0) = -\frac{\Lambda}{2}\dot{L}_0(t)v(0) \end{aligned} \tag{3.16}$$

with $\ell(y,0) = \ell_0(y) \in L^2((0,\Lambda))$ a given initial data.

Defining the bilinear form κ in $\mathcal{V} \times \mathcal{V}$ as:

$$\kappa : (u,v) \mapsto \Lambda^2 K \int_0^\Lambda \partial_y u(y) \partial_y v(y) \, dy + \frac{\Lambda K \tilde{a}}{2a_1} u(0)v(0), \tag{3.17}$$

which is symmetric and coercive on $\mathcal{V}$, well-posedness of the problem (3.16) follows from standard results on parabolic equations (see e.g. [88]). Moreover, it is well known that the solution $\ell(\cdot, t)$ is of class $\mathcal{C}^\infty([0, \Lambda])$ for any time $t > 0$.

3.2.5 *Analytical periodic solutions*

Let us now solve the system (3.15) using the following ansatz $\ell(y, t) = \underline{\ell}(y)e^{i\omega t}$. From (3.14) we deduce the following equation:

$$i\underline{\ell} = \Lambda^2 K_\omega \partial_{yy}\underline{\ell}\,. \tag{3.18}$$

The characteristic polynomial associated to (3.18) has two roots, $r := \dfrac{1+i}{\Lambda\sqrt{2K_\omega}}$ and $-r$, which leads to the following solutions:

$$\underline{\ell}(y) = \alpha e^{ry} + \beta e^{-ry}, \tag{3.19}$$

with $\alpha,\ \beta \in \mathbb{C}$.

We then determine α and β using boundary conditions:

$$\begin{cases} -(\alpha+\beta)\dfrac{\tilde{a}}{2a_1} + \Lambda r(\alpha-\beta) = \dfrac{i\varepsilon}{2K_\omega}, \\ \alpha e^{r\Lambda} + \beta e^{-r\Lambda} = 0, \end{cases}$$

i.e.,

$$\begin{cases} \alpha = \dfrac{i\varepsilon}{2K_\omega\big(\dfrac{\tilde{a}}{2a_1}(e^{2r\Lambda}-1) + \Lambda r(e^{2r\Lambda}+1)\big)}, \\ \beta = -e^{2r\Lambda}\alpha. \end{cases} \tag{3.20}$$

We notice that $r\Lambda = \dfrac{1+i}{\sqrt{2K_\omega}}$ only depends on K_ω.

3.3 *Convergence of the discrete model towards the continuous one*

We first notice that the discrete problem (3.6) is a kind of *non conventional* mass-lumped version of a finite element discretization of the continuous one (3.15). In order to clarify this statement, we introduce the finite element setting. Let $\mathcal{V}_h \subset \mathcal{V}$ the space of continuous, piecewise linear functions g on the one-dimensional partition $T_h = \{y_1, \cdots, y_{N+1}\}$ of $(0, \Lambda)$, and that verify the Dirichlet boundary condition $g(\Lambda) = 0$. Let $\{\Phi_j\}_{j=1,\,N}$ be the standard basis for $\mathcal{V}_h$ consisting of the hat functions defined by $\Phi_j(y_k) = \delta_{j,k}$ for $1 \le j, k \le N$.

Let $\ell_h \in \mathcal{V}_h$ be the continuous, piecewise linear function such that for $1 \le j \le N+1$, $t > 0$, $\ell_h(y_j, t) = \ell_j(t)$. Using the basic semi-discrete Galerkine method would lead to the discretization of (3.21) in the matrix form:

$$\frac{d(M_h L_h)}{dt} + K_h L_h = \tilde{f}(t), \tag{3.21}$$

with $L_h(t) = (\ell_1(t), \cdots, \ell_N(t))^T$. Similarly, $\tilde{f} = (-\frac{\Lambda}{2}\dot{L}_0, 0, \cdots, 0)$, $(M_h)_{i,j} = \int_0^\Lambda \Phi_i(y)\Phi_j(y)dy$ and $(K_h)_{i,j} = \kappa(\Phi_i, \Phi_j)$, where κ is defined in equation (3.17).

Computing explicitly the coefficients of the matrices K_h and M_h gives

$$(K_h)_{ij} = \begin{cases} -\Lambda^2 K/h & \text{for } |i-j| = 1, \\ 2\Lambda^2 K/h & \text{for } i = j \geq 2\,, \\ \Lambda^2 K/h + \Lambda K\tilde{a}/(2a_1) & \text{for } i = j = 1\,, \end{cases}$$

and

$$(M_h)_{ij} = \begin{cases} h/6 & \text{for } |i-j| = 1, \\ 2h/3 & \text{for } i = j \geq 2\,, \\ h/3 & \text{for } i = j = 1\,. \end{cases}$$

The key observation is that Eqs. (3.6) and (3.8) are nothing but a mass-lumped discretization of (3.15) where the mass matrix M_h has been replaced by the diagonal version

$$\widetilde{M}_h = \begin{pmatrix} h & & 0 \\ & \ddots & \\ 0 & & h \end{pmatrix}.$$

Hence, ℓ_h actually solves

$$\frac{d(\widetilde{M}_h L_h)}{dt} + K_h L_h = \tilde{f}(t)\,, \tag{3.22}$$

together with the initial condition

$$\ell_h(0) = \ell_{0,h} \in \mathcal{V}_h\,. \tag{3.23}$$

The classical mass-lumped method, on the other hand, would have consisted in replacing the tridiagonal mass matrix M_h by a diagonal matrix $\bar{M}_h$ using an integration formula on the vertices of the partition. Namely, using the trapezoidal formula $\int_0^\Lambda g \sim \big(\frac{1}{2}g(y_1) + \sum_{j=2}^{N} g(y_j) + \frac{1}{2}g(y_{N+1})\big)h = \big(\frac{1}{2}g(y_1) + \sum_{j=2}^{N} g(y_j)\big)h$, for a function g satisfying $g(\Lambda) = 0$ leads to the mass-lumped matrix

$$\bar{M}_h = \begin{pmatrix} h/2 & & & 0 \\ & h & & \\ & & \ddots & \\ 0 & & & h \end{pmatrix} \tag{3.24}$$

which differs from $\widetilde{M}_h$.

We shall then study the ODE (3.22), (3.23) using the method presented in [100] which provides us with a convergence result for the mass-lumped method with $\bar{M}_h$.

We introduce the two following inner products on $\mathcal{V}_h$ associated with $\bar{M}_h$ and $\widetilde{M}_h$ respectively. Namely, for $(u_h, v_h) \in \mathcal{V}_h$

$$\langle u_h, v_h \rangle_h = \frac{h}{2} u_h(y_1) v_h(y_1) + h \sum_{j=2}^{N} u_h(y_j) v_h(y_j)$$

and

$$(u_h, v_h)_h = h \sum_{j=1}^{N} u_h(y_j) v_h(y_j) \, .$$

We also call $\| \cdot \|_h$ the norm associated to $(\cdot, \cdot)_h$, while the L^2 norm and inner products are denoted by $\| \cdot \|$ and $(\cdot, \cdot)$ respectively. Gerschgörin Theorem applied to M_h shows the equivalence of the norms $\| \cdot \|$ and $\| \cdot \|_h$ on $\mathcal{V}_h$ *uniformly* in h, and, more precisely, we have the estimate, valid for all $v_h \in \mathcal{V}_h$

$$\frac{1}{6} (v_h, v_h)_h \leq (v_h, v_h) \leq (v_h, v_h)_h \, ,$$

from which we also deduce

$$h v_h(y_1)^2 \leq \|v_h\|_h^2 \leq 6 \|v_h\|^2 \, . \tag{3.25}$$

Finally, we introduce, for $u_h, v_h \in \mathcal{V}_h$, $\delta_h(u_h, v_h) = (u_h, v_h)_h - (u_h, v_h)$ the quadrature error.

Lemma 3.3.1 (First estimates).

Let $u_h, v_h \in \mathcal{V}_h$. We have, for h sufficiently small:

$$|\delta_h(u_h, v_h)| \leq Ch \|\partial_y u_h\| \|\partial_y v_h\|, \tag{3.26}$$

$$|\delta_h(u_h, v_h)| \leq C\sqrt{h} \|\partial_y u_h\| \|v_h\| \tag{3.27}$$

for a constant C that does not depend on u_h, v_h or h.

Proof. In all what follows, C denotes a constant that may vary from line to line, being always independent of h. Let $u_h, v_h \in \mathcal{V}_h$. We write $|\delta_h(u_h, v_h)| \leq |(u_h, v_h)_h - \langle u_h, v_h \rangle_h| + |\langle u_h, v_h \rangle_h - (u_h, v_h)|$. Thomée [100] provides us with an estimate of the error between $\langle u_h, v_h \rangle_h$ and (u_h, v_h), namely,

$$|\langle u_h, v_h \rangle_h - (u_h, v_h)| \leq Ch^2 \|\partial_y u_h\| \|\partial_y v_h\|$$

and

$$|\langle u_h, v_h \rangle_h - (u_h, v_h)| \leq Ch \|\partial_y u_h\| \|v_h\|$$

for some constant $C > 0$ that does not depend on u_h, v_h or h. The latter estimate is obtained by an inverse inequality.

It remains to estimate the term $\tilde{\delta}_h(u_h, v_h) = (u_h, v_h)_h - \langle u_h, v_h \rangle_h$.

We notice that:

$$|\tilde{\delta}_h(u_h, v_h)| = \frac{h}{2}|u_h(y_1)v_h(y_1)| \tag{3.28}$$

$$= \frac{h}{2}\left|\int_0^\Lambda \partial_y u_h(y)\,dy\right|\left|\int_0^\Lambda \partial_y v_h(y)\,dy\right|$$

$$\leq \frac{h\Lambda}{2}\|\partial_y u_h\|\|\partial_y v_h\|\,. \tag{3.29}$$

Similarly, (3.28) together with (3.25) gives:

$$|\tilde{\delta}_h(u_h, v_h)| \leq C\sqrt{h}\|\partial_y u_h\|\|v_h\|. \tag{3.30}$$

This yields (3.26) and (3.27). □

THEOREM 3.3.1 · *Convergence in L^2 norm*

If ℓ and ℓ_h are solution to (3.16) and (3.22), (3.23) respectively, and $\ell_0 \in H^2((0,\Lambda))$, we have, for all $t \geq 0$,

$$\|\ell_h(t) - \ell(t)\| \quad \leq C\|\ell_{0,h} - \ell_0\| + Ch^2(\|\partial_{yy}\ell_0\| + \|\partial_{yy}\ell(t)\|)\,Ch\left(\int_0^t \|\partial_{yt}\ell\|^2 ds\right)^{1/2}.$$

Proof. Let R_h be the Ritz projector from $\mathcal{V}$ on $\mathcal{V}_h$, associated with $\kappa(\cdot,\cdot)$. Namely, for $g \in \mathcal{V}$, $R_h g$ is defined by

$$\kappa(R_h g, v_h) = \kappa(g, v_h)$$

for all $v_h \in \mathcal{V}_h$. We write $\ell_h - \ell = (\ell_h - R_h\ell) + (R_h\ell - \ell) = \theta_h + \rho$ (Notice that $\theta_h \in \mathcal{V}_h$). Standard estimations show that $\rho(t)$ satisfies $\|R_h\ell - \ell\| \leq Ch^2\|\partial_{yy}\ell\|$. In order to estimate θ_h, we write, for all $\chi_h \in \mathcal{V}$

$$\begin{aligned}
(\partial_t\theta_h, \chi_h)_h + \kappa(\theta_h, \chi_h) &= (\partial_t\ell_h, \chi_h)_h + \kappa(\ell_h, \chi_h) - (\partial_t R_h\ell, \chi_h)_h - \kappa(R_h\ell, \chi_h)\\
&= (f, \chi_h) - (\partial_t R_h\ell, \chi_h)_h - \kappa(\ell, \chi_h)\\
&= (\partial_t\ell, \chi_h) - (\partial_t R_h\ell, \chi_h)_h\\
&= -(\partial_t\rho, \chi_h) - \delta_h(\partial_t R_h\ell, \chi_h).
\end{aligned} \tag{3.31}$$

Setting $\chi_h = \theta_h$, we obtain

$$\frac{1}{2}\frac{d}{dt}\|\theta_h\|_h^2 + \kappa(\theta_h, \theta_h) = -\left(\partial_t\rho, \theta_h\right) - \delta_h\left(\partial_t R_h\ell, \theta_h\right).$$

Here, we have at once, using Cauchy-Schwarz and Poincaré inequalities:

$$\begin{aligned} |(\partial_t \rho, \theta_h)| &\leq \|\partial_t(\ell - R_h\ell)\| \, \|\theta_h\| \\ &\leq Ch \, \|\partial_{yt}\ell\| \, \|\theta_h\| \\ &\leq Ch \, \|\partial_{yt}\ell\| \, \|\partial_y\theta_h\|. \end{aligned}$$

Using the first equation of lemma 3.3.1, and the fact that $\|\partial_y R_h u\| \leq C\|\partial_y u\|$, we also obtain

$$\begin{aligned} |\delta_h \left(\partial_t R_h\ell, \theta_h\right)| &\leq Ch \, \|\partial_{yt} R_h\ell\| \, \|\partial_y\theta_h\| \\ &\leq Ch \, \|\partial_{yt}\ell\| \, \|\partial_y\theta_h\| \, , \end{aligned}$$

from which we deduce that

$$\begin{aligned} \frac{1}{2}\frac{d}{dt}\|\theta_h\|_h^2 + \kappa(\theta_h, \theta_h) &\leq Ch \, \|\partial_{yt}\ell\| \, \|\partial_y\theta_h\| \\ &\leq \kappa(\theta_h, \theta_h) + Ch^2 \, \|\partial_{yt}\ell\|^2 \, , \end{aligned}$$

using the coercivity of $\kappa(\cdot, \cdot)$ on $\mathcal{V}$. We therefore infer

$$\|\theta_h(t)\|_h^2 \leq \|\theta_h(0)\|_h^2 + Ch^2 \int_0^t \|\partial_{yt}\ell\|^2 \, ds \, .$$

We now recall that $\|\cdot\|_h$ and $\|\cdot\|$ are equivalent norms on $\mathcal{V}_h$, uniformly in h, and hence

$$\|\theta_h(t)\| \leq C\|\theta_h(0)\| + Ch \left(\int_0^t \|\partial_{yt}\ell\|^2 \, ds \right)^{1/2} .$$

Here $\|\theta_h(0)\| = \|\ell_{0,h} - R_h\ell_0\|$ and

$$\begin{aligned} \|\ell_{0,h} - R_h\ell_0\| &\leq \|\ell_{0,h} - \ell_0\| + \|\ell_0 - R_h\ell_0\| \\ &\leq \|\ell_{0,h} - \ell_0\| + Ch^2\|\partial_{yy}\ell_0\|, \end{aligned}$$

whence $\theta_h(t)$ is bounded as desired. □

THEOREM 3.3.2 · *Convergence in $\mathcal{H}^1$ norm*

If ℓ and ℓ_h are solution to (3.16) and (3.22), (3.23) respectively we have, for $t \geq 0$,

$$\begin{aligned} \|\partial_y(\ell_h - \ell)(t)\| \leq \; & Ch(\|\partial_{yy}\ell_0\| + \|\partial_{yy}\ell(t)\|) + C\|\partial_y(\ell_{0,h} - \ell_0)\| \\ & + C\sqrt{h} \left(\int_0^t \|\partial_{yt}\ell\|^2 ds \right)^{1/2} . \end{aligned}$$

Proof. We now set $\chi_h = \partial_t\theta_h$ in equation (3.31) for θ_h to obtain:

$$\|\partial_t\theta_h\|_h^2 + \frac{1}{2}\frac{d}{dt}\kappa(\theta_h, \theta_h) = -(\partial_t\rho, \partial_t\theta_h) - \delta_h(R_h\partial_t\ell, \partial_t\theta_h).$$

Here, as in the proof of theorem 3.3.1,

$$|(\partial_t\rho, \partial_t\theta_h)| \leq \|\partial_t(\ell - R_h\ell)\|\|\partial_t\theta_h\| \leq C\sqrt{h}\|\partial_{yt}\ell\|\|\partial_t\theta_h\|.$$

Further, by the second line of lemma 3.3.1,

$$\begin{aligned} |\delta_h(\partial_t R_h\ell, \partial_t\theta_h)| &\leq C\sqrt{h}\|\partial_{yt}R_h\ell\|\|\partial_t\theta_h\| \\ &\leq C\sqrt{h}\|\partial_{yt}\ell\|\|\partial_t\theta_h\|. \end{aligned}$$

Using again the equivalence between the norms $\|\cdot\|_h$ and $\|\cdot\|$ on $\mathcal{V}_h$, we conclude:

$$\begin{aligned} \|\partial_t\theta_h\|_h^2 + \frac{1}{2}\frac{d}{dt}\kappa(\theta_h, \theta_h) &\leq C\sqrt{h}\|\partial_{yt}\ell\|\|\partial_t\theta_h\|_h \\ &\leq \|\partial_t\theta_h\|_h^2 + Ch\|\partial_{yt}\ell\|^2, \end{aligned}$$

so that, after integration, and using the coercivity of $\kappa(\cdot,\cdot)$ on $\mathcal{V}$

$$\begin{aligned} \|\partial_y\theta_h(t)\| &\leq C\|\partial_y\theta_h(0)\| + C\sqrt{h}\left(\int_0^t \|\partial_{yt}\ell\|^2 ds\right)^{1/2} \\ &\leq \|\partial_y(\ell_{0,h} - \ell_0)\| + Ch\|\partial_{yy}\ell_0\| + C\sqrt{h}\left(\int_0^t \|\partial_{yt}\ell\|^2 ds\right)^{1/2}. \end{aligned}$$

This, together with the standard estimate for $\partial_y\rho(t)$ completes the proof. □

We proved the convergence of the discrete N-spring swimmer to the continuous model we formally derived in the previous section. Note that we obtain only a first-order (resp. half order) convergence in L^2 norm (resp. H^1 norm) while the standard estimations for the mass-lumping method leads to a second-order (resp. first order) convergence . This is due to the Fourier-type boundary condition at 0 which differs from the classical Dirichlet boundary condition used in [100].

3.4 *Mathematical expression of the displacement*

3.4.1 *Net displacement of the N-spring swimmer*

We seek the swimmer's displacement by looking at the displacement of the first of the largest sphere, meaning we only compute $V_1 = \dot{x}_1$, and integrate over a period $(0, 2\pi/\omega)$.

Taking into account the hydrodynamic interactions due to the i^{th}-sphere with $i \in \{2, \cdots, N+2\}$ on the first sphere, we have

$$V_1 = \frac{1}{6\pi\mu a_1} f_1^F + \frac{1}{4\pi\mu L_0} f_2^F + \frac{1}{4\pi\mu}\sum_{i=3}^{N+2} \frac{f_i^F}{L_0 + L_1 + \cdots + L_{i-2}}$$

Using expressions (3.2) and (3.5), we obtain

$$V_1 \;= \frac{1}{2}\dot{L}_0 - \frac{\tilde{a}}{2a_1}K\ell_1 - \frac{3a_1\dot{L}_0}{4L_0} - \frac{3K\tilde{a}\ell_1}{4L_0} + \frac{3\tilde{a}K}{2}\sum_{j=1}^{N}\frac{\ell_j-\ell_{j+1}}{\sum_{i=0}^{j}L_i}\,, \tag{3.32}$$

where we recall that, by convention, $\ell_{N+1}=0$.

Finally, by integrating over one period, and noticing that both ℓ_2 and $\dot{L}_1/L_1$ have a vanishing time-average, we obtain, for any value of $h=\Lambda/N$, the displacement of the corresponding N-spring swimmer:

$$\Delta_h x_1 = \int_0^{2\pi/\omega}\Big[-\frac{3K\tilde{a}\ell_1}{4L_0} + \frac{3\tilde{a}K}{2}\sum_{j=1}^{N}\frac{\ell_j-\ell_{j+1}}{\sum_{i=0}^{j}L_i}\Big]\,dt \tag{3.33}$$

3.4.2 *Net displacement of the limit model*

We may find an expression for the displacement of the limit model as h tends to 0, by passing to the limit in the preceding expression.

Indeed, for h and y given, we define $j_h(y)$ the unique integer such that $j_h(y)h \le y \le (j_h(y)+1)h$. Then, defining χ_h the function

$$\chi_h(y,t) = \frac{1}{L_0(t)+\cdots+L_{j_h(y)+1}(t)},$$

we may write

$$\int_0^{2\pi/\omega}\sum_{j=0}^{N-1}\frac{\ell_h(jh,t)-\ell_h((j+1)h,t)}{\sum_{i=0}^{j+1}L_i}\,dt = -\int_0^{2\pi/\omega}\int_0^{\Lambda}\partial_y\ell_h(y,t)\chi_h(y,t)\,dy\,dt\,,$$

where ℓ_h is the piecewise linear function defined in the previous section.

Finally, the displacement $\Delta_h x_1$ of the N-spring swimmer during one time period can be rewritten as

$$\Delta_h x_1 = \int_0^{2\pi/\omega}\Big[-\frac{3K\tilde{a}\ell_h(0,t)}{4L_0(t)} - \frac{3\tilde{a}K}{2}\int_0^{\Lambda}\partial_y\ell_h(y,t)\chi_h(y,t)\,dy\Big]\,dt\,.$$

Now, using the fact that $j_h(y)h \to y$ when $h \to 0$, together with the L^2 and H^1 convergence of ℓ_h to ℓ, we obtain that, for any y and t,

$$\chi_h(y,t) = \frac{1}{L_0(t) + (j_h(y)+1)h + \dfrac{h}{\Lambda}\displaystyle\sum_{i=0}^{j} \ell_h(ih,t)}$$
$$\xrightarrow[h\to 0]{} \frac{1}{L_0(t) + y + \displaystyle\int_0^y \frac{\ell(t)}{\Lambda}} =: \chi(y,t)$$

Moreover $0 \leq \chi_h(y,t) \leq \max_t \frac{1}{L_0(t)} = \frac{1}{L(1-\tilde{\varepsilon})}$, shows that χ_h is uniformly bounded. Therefore, using dominated convergence theorem, we deduce that χ_h converges to χ in $L^2(0, 2\pi/\omega; (0,\Lambda))$ as h tends to 0.

Using the convergence theorems proven in the preceding section, we may pass to the limit $h \to 0$ in $\Delta_h x_1$, and obtain the following expression for the displacement during one period for the limit model

$$\Delta x_1 = \int_0^{2\pi/\omega}\int_0^{\Lambda} -\frac{3K\tilde{a}}{2}\partial_y \ell(y,t)\left(L_0(t) + y + \int_0^y \frac{\ell}{\Lambda}\right)^{-1} dy\,dt - \int_0^{2\pi/\omega} \frac{3K\tilde{a}\ell(0,t)}{4L_0} dt\,. \tag{3.34}$$

3.5 *Numerical experiments*

In this section, we numerically study the discrete model's convergence towards the continuous one. Then, we investigate the influence of the two parameters ω and $\tilde{\varepsilon}$ on the system and on its displacement, while the rest of the swimmer is determined by the values in table 3.1. All simulations are achieved using MATLAB. We consider here that the default length L of the active arm is small compared to the rest of the swimmer. The first sphere thus acts like the head of a sperm cell, and the active arm like a link between the head and the flagella, which gives a signal so that the rest of the system oscillates.

Table 3.1. Values of the parameters used in the numerical simulations, matching those of [74]. We have taken for μ the dynamic viscosity of water at $25°C$.

$\tilde{a}$	$1 \cdot 10^{-5}\, m$
a_1	$1 \cdot 10^{-5}\, m$
Λ	$4 \cdot 10^{-4}\, m$
L	$3 \cdot 10^{-5}\, m$
$\tilde{k}$	$1 \cdot 10^{-8}\, Nm^{-1}$
μ	$8.9 \cdot 10^{-4}\, Pa\,s$

3.5.1 *Convergence of the discrete models to the continuous one*

We investigate numerically the convergence estimations obtained in section 3.3. We recall that the continuous solution ℓ solves the heat equation PDE with the Fourier-type boundary conditions (3.15). We consider, in this section, periodic forcing for which explicit solutions are given by (3.19, 3.20).

Convergence of the N-spring discrete model · We recall that the discrete solution ℓ_h is the P^1 discrete function based on the $(\ell_i)_i$ solution to the N-spring ODE system (3.6,3.7,3.8). This discrete system corresponds to a semi-discretization in space of the continuous model, based on a non conventional mass-lumping method. The solution $(\ell_i)_i$ of the discrete problem in the periodic setting is given in equations (3.9,3.10,3.12,3.13).

The space step h (or equivalently the number of springs N) being given, the discrete error is defined as the error between ℓ_h and the P^1 interpolation of ℓ. We plot in figure 3.3, the L^2 (resp. H^1) error denoted by e_{h,L^2} (resp. e_{h,H^1}).

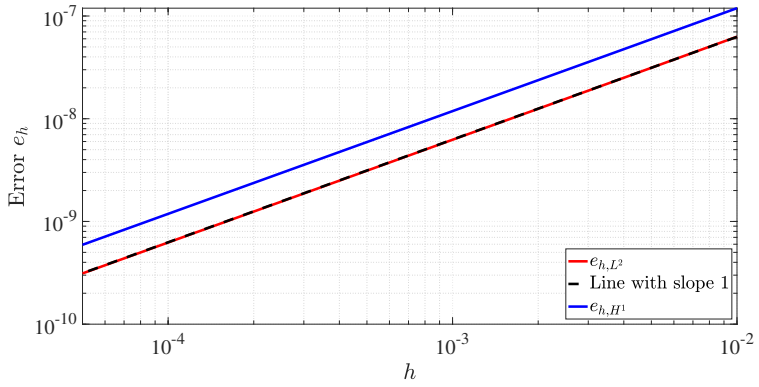

Figure 3.3. L^2 and H^1 errors between the N-spring discrete model and the continuous one as a function of the number of springs in log scale, in the $(2\pi/\omega)$-periodic case, for $\tilde{\varepsilon} = 0.7$ and $\omega = 1\, rad \cdot s^{-1}$.

We observe that the L^2 error converges with order one, as expected from theorem 3.3.1. Concerning the H^1 error, we observe a superconvergence phenomenon: as the L^2 error, it converges at order 1, while theorem 3.3.2 predicts a convergence at order $1/2$. This can be explained by the regularity of the considered periodic solution.

Influence of mass-lumping · As mentioned earlier, the N-spring model turns out to be a discretization in space of the continuous problem (3.15), based on an unconventional mass-lumping method. The convergence proof that we proposed in section 3.3 is based on the results of Thomée [100]. He shows that, for a standard mass-lumping discretization, the usual order of convergence for finite elements is obtained: convergence of order 2 for the L^2 error and 1 for the H^1 error.

We investigate here the influence of the space discretization, by comparing the N-spring model (3.22), solved numerically this time, to the classical mass-lumping

method (3.24) and the standard Galerkin finite element method (3.21). Again we consider the periodic framework for which the exact solution is available. The time discretization of the three ODE systems is achieved using a Crank-Nicolson scheme for which the time step is chosen to be small enough so that the error due to the time discretization is negligible.

The corresponding L^2 (resp. H^1) error is given on figure 3.4 (resp. figure 3.5). We can see that, as expected, the L^2 error converges at order 1 for the N-spring model, while it converges at order 2 for both the classical mass-lumping method and the standard Galerking discretization. Again, due to the regularity of the solutions, a super-convergence phenomenon of the H^1 error is observed for all three methods: as the L^2 error, it converges at order 1 for the N-spring model and order 2 for the other two discretizations.

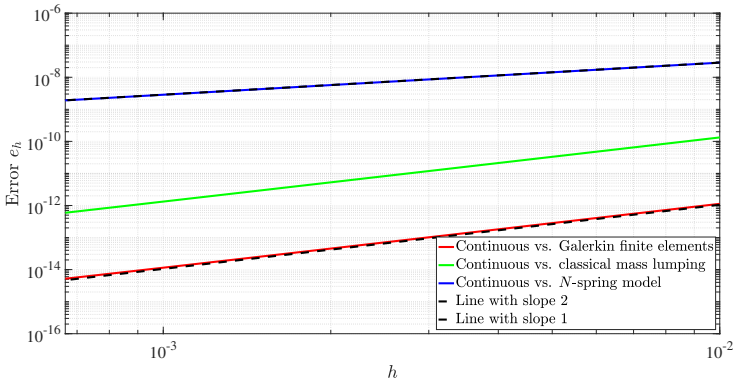

Figure 3.4. L^2 error between the continuous model and our mass-lumping method, as a function of the number of springs, in log scale.

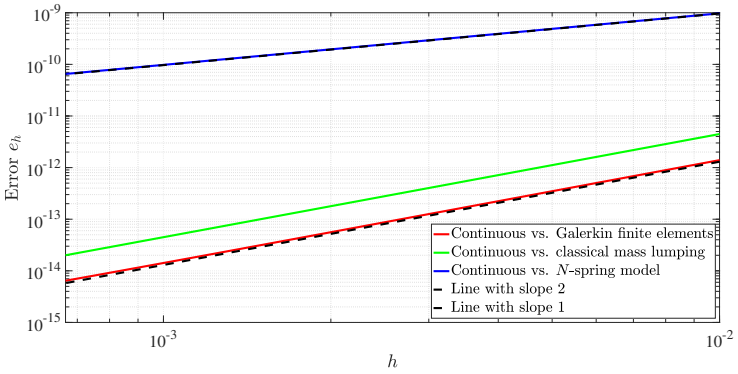

Figure 3.5. H^1 error between the continuous model and our mass-lumping method, as a function of the number of springs, in log scale.

3.5.2 *Swimming strokes*

In this section, we investigate the swimming ability of the N-spring swimmer. The stroke being periodic, we use the explicit solutions given in section 3.2.2. The computations are achieved for $N = 2,000$ springs.

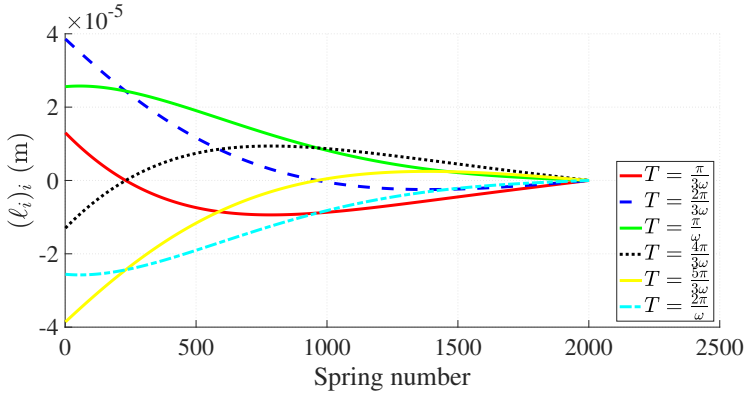

Figure 3.6. Movement of the whole $2,000$-springs swimmer during a full stroke, at different time stamps T, for $\omega = 1\, rad \cdot s^{-1}$ and $\tilde{\varepsilon} = 0.7$.

Deformation of the swimmer · Figure 3.6 shows a full stroke of the swimmer, in which we notice that a wave is propagating along its tail. Remember that this wave is a contraction wave along the horizontal tail. This tail appears to be oscillating fairly efficiently for the side close to the head, while the amplitude of the contraction decays considerably on the second half of the tail.

The movement shown corresponds to the stretch of ℓ_j, and not to the actual deformation which would be ℓ_j/N, for all $1 \leq j \leq N$. We thus remark that this deformation is relatively small compared to the size of the artificial swimmer, which matches the approximation of small deformations that we made in the first place.

Displacement · In this section, we study the influence of the parameters $\tilde{\varepsilon}$ and K_ω on the swimmer's displacement (3.33), in order to maximize its absolute value.

In figure 3.7, we plot the displacement of the swimmer as a function of time, for different values of $\tilde{\varepsilon}$. The displacement is computed through numerical integration of equation (3.33). The graph shows that the swimmer globally swims backwards, and we recognize the back and forth motion which is characteristic of low Reynolds number artificial swimmers. A larger amplitude $\tilde{\varepsilon}$ of the forcing leads to a larger displacement and we observe (see figure 3.8), that Δx_1 is proportional to $\tilde{\varepsilon}^2$, which is what is expected in theory (similar behaviors are observed, e.g., in [15], [16], [35] and explained as the surface of loops in the space of shapes [5]).

As we want to maximize Δx_1 while having $\tilde{\varepsilon} < 1$, we choose a fixed value $\tilde{\varepsilon} = 0.7$ which, although arbitrary, allows for an easier comparison to Montino and DeSimone's results [74], as they made a similar parameter choice.

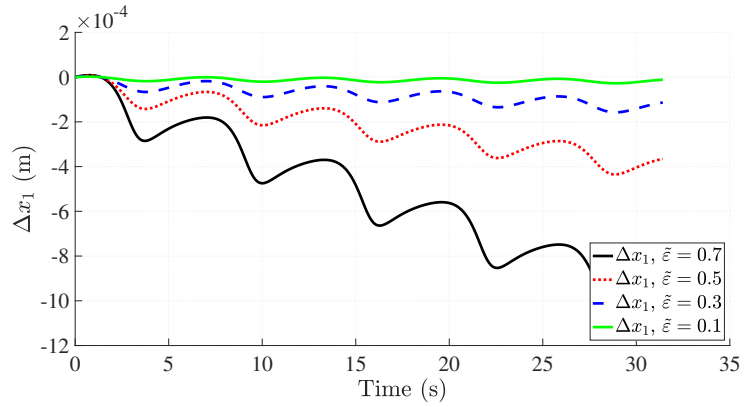

Figure 3.7. Displacement of the $2,000$-spring swimmer against time t, for different values of $\tilde{\varepsilon}$.

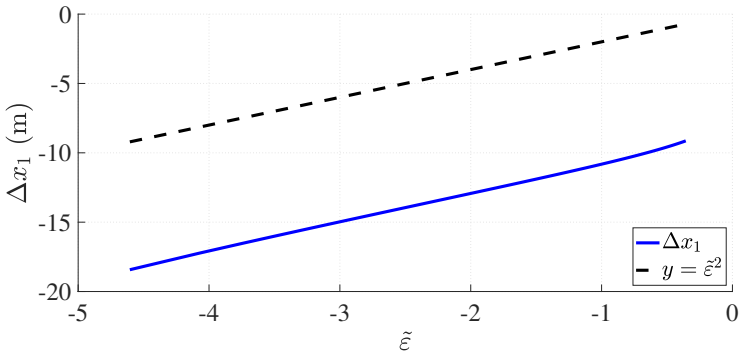

Figure 3.8. Displacement of the $2,000$-spring swimmer depending on ε for an arm oscillating frequency $\omega = 1\, rad/s$ compared to $y = \tilde{\varepsilon}^2$, in log-scale.

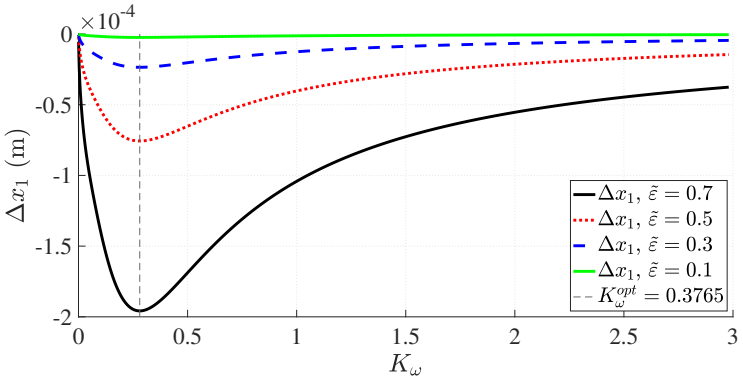

Figure 3.9. Displacement of the $2,000$-spring swimmer depending on K_ω, for different values of $\tilde{\varepsilon}$.

Figure 3.9 shows Δx_1 depending on K_ω, for different values of $\tilde{\varepsilon}$. At any fixed K_ω, we observe once again that larger $\tilde{\varepsilon}$ leads to larger Δx_1. We first observe that, if $K_\omega \to \infty$, the net displacement of the swimmer vanishes. According to the expression of K_ω, this is the case for example when $\omega \to 0$: the oscillation disappears, immobilizing

the artificial swimmer. This can also happen when $\tilde{k} \to \infty$: the springs become so rigid that the tail of the swimmer can no longer deform. In that case, the swimmer has only one degree of freedom left to deform and faces Purcell's Scallop theorem's obstruction. Similarly, letting $K_\omega \to 0$ immobilizes the swimmer. An optimal value K_ω^{opt} for the non-dimensional parameter is reached between these two limiting cases, in order to maximize the displacement on one time period. According to the figure, $K_\omega^{\text{opt}} \simeq 0.3765$. A complete mathematical expression of K_ω^{opt} does not seem available, due to the largely nonlinear nature of the problem contrarily to the final expression obtained in [74]. A pair of optimal values for ω and k to obtain this K_ω^{opt} are $\omega = 1\, rads^{-1}$ and $\tilde{k} \simeq 6.207 \cdot 10^{-8} Nm^{-1}$. Moreover, the expression of K_ω guarantees that ω must vary proportionally to $\tilde{k}$ for the pair $(\tilde{k}, \omega)$ to remain at the optimum. Indeed, the softer the spring, the slower the first arm needs to oscillate in order to generate a large movement.

Looking at the other parameters separately, we can also clearly see from equation (3.33), that the displacement depends linearly on $\tilde{a}$, which is predictable. However, this parameter has a direct consequence on the size of the artificial swimmer and must stay in a reasonable range (in our case no more than $1e^{-5}\, m$) so that the swimmer stays at microscopic scale.

Finally, we notice that the value of Λ and the ratio $a_1/\tilde{a}$ has little to no influence on the previous analysis. We therefore keep for those parameters values that seem coherent with the scale we are working at, and that match with numerical experiments provided in [74].

3.6 *Conclusion*

We analyzed the dynamics of two low-Reynolds-number swimmers. The first one, which is an extension of [74], is made of N passive springs, and the second one is the corresponding limit model with an elastic tail. Both are activated by an active arm that elongates and retracts periodically with amplitude ε and angular frequency ω.

Noting that the N-spring swimmer is a non-conventional mass lumping discretization of the limit model, we proved its convergence, when N tends to infinity, to the continuous model, by extending the results of Thomée [100] to the case of a Fourier-type boundary condition. For both swimmers, a phase difference between the oscillations of the active arm and the tail is created by the interaction between elastic and hydrodynamic forces. Then, both models undergo non-reciprocal shape changes and thus circumvent Scallop Theorem's obstruction [87]. Numerical simulations indeed show a wave propagating along the swimmers' tails. Similarly to what was shown in [74], our models are able to swim but there is no control over the swimming direction.

Then, we focused on computing the net displacement over a time period of the swimmer in both cases, in view of its optimization. We obtain explicit formulae for this displacement as a function of the local elongation during the stroke. We numerically recover the classical back and forth swimming and the second-order scaling of the displacement as a function of the maximum elongation of the forcing active arm. Moreover, we highlight a dimensionless parameter K_ω, driving the movement of the

swimmer when its geometry (Λ, a, a_1) is given. Some optimal values for this parameter can be estimated by numerical experiments.

Lastly, we noticed that, similarly to the behavior of Machin's swimming rod [73], the deformations of both our swimmers is rapidly attenuating along their passive parts, which suggests that some form of activation is needed in order to mimic the type of behavior observed in nature.

Tiny currents swirl,
Microswimmers drift and dive,
Life in silent waves.

ChatGPT

4 *The N-link model for slender rods in a viscous fluid: well-posedness and convergence to classical elastohydrodynamics equations*

This chapter reproduces a paper in preparation, written in collaboration with François Alouges, Aline Lefebvre-Lepot and Clément Moreau.

4.1 *Introduction*

Flexible fibers are ubiquitous in nature, particularly at microscale, playing key roles as flagella and cilia for microbiological locomotion [59] and structural components of cell membranes, polymer chains [25], and micro-robotics [21].

The dynamics of a slender filament in a fluid is governed by the intricate coupling between mechanical properties of the deformable filament, and hydrodynamic interactions between the filament and the fluid. In addition, internal or external effects such as gravity, magnetic field or internal activity can yield a broad range of behaviors like undulating, twisting or knotting.

Casting this fluid-structure interaction problem as a set of equations requires various modeling assumptions [36], [72], going from a full 3D description of both filament and fluid to simplifications pertaining to the filament slenderness and the specificities of low-Reynolds number hydrodynamics. In the slender limit, for planar motion, and neglecting effects of internal shear, elastic restoring torque is linearly related to local curvature and bending stiffness according to Euler-Bernoulli beam theory [13], [101].

For the treatment of hydrodynamics, Resistive Force Theory (RFT) [46], first developed in the 1950s and which approximates the local drag as a linear anisotropic operator related to the local velocity, remains to this day a prominently popular choice as a simple approximation with satisfying accuracy [111]. Non-local models, often termed as slender body theory (SBT), and regularized Stokeslet methods typically provide higher accuracy in cases where it is warranted [78], [101].

Combining these fundamental modeling assumptions, we thus focus on a 1D, planar, inextensible Euler-Bernoulli rod in a viscous fluid modeled through RFT. The equations for the dynamics of the position and shape of the filament form a fourth-order nonlinear

partial differential equation (PDE) system, which is considered as standard in the filament elastohydrodynamics literature [13], [49], [59].

The nonlinear terms arising from the inextensibility constraint make the filament elastohydrodynamics equations notoriously tricky to solve numerically with reasonable levels of accuracy and computational efficiency [41]. To avoid the computational burden of solving PDEs, a range of approximate models for the elastic filament have been developed, sharing the idea of reducing system dimension by replacing the continuous elastic body with a collection of rigid parts connected by elastic junctions. Commonplace examples include the N-beads formulation, for which the filament is seen as a chain of spheres, and the N-link, for which it is seen as a chain of slender, straight rods. It is worth noting that these models not only constitute approximations of a flexible fiber, but also exactly describe the structure of some flexible micro-robots built as an assembly of magnetic parts [3], [75], [84].

The N-link model relies on analytic integration of the hydrodynamic force density carried on individual segments. Then, the dynamics are reduced to those of a first-order differential algebraic system, considerably reducing the computational cost for numerical simulation and allowing further refinements on dealing with hydrodynamics [103] and obstacles [38], [93].

Whether it is on the PDE formulation or its discrete N-link approximation, mathematical analysis of elastohydrodynamics is relatively scarce, with the first well-posedness (existence and uniqueness of the solution for a given initial data) result in the continuous case having been stated only recently by Mori & Ohm [76]. Relying on the Banach fixed point theorem, the authors establish global existence of solutions in L^2 for small initial data and local existence of solutions for arbitrary initial data. On the other hand, justification of existence and uniqueness of the solutions of the N-link system is currently lacking. Furthermore, despite the reasonable physical grounds for approximating a flexible fiber by a collection of small rigid segments and the observable and quantifiable numerical convergence of the N-link system's solution towards that of the continuous model [75], no formal proof of convergence between both models as N approaches infinity is available to the best of our knowledge.

In this paper, we address both these questions and rigorously establish the well-posedness of the N-link equations (Theorem 4.2.1), and the convergence (up to extraction of a subsequence) of this solution in suitable functional spaces towards the solution of the continous elastohydrodynamics equations (Theorem 4.2.2).

Both proofs follow classical blueprints. Theorem 4.2.2 for *free* boundary conditions is an application of the Cauchy-Lipschitz theorem, which requires verifying that the hydrodynamic resistance matrix is invertible. An extension to other standard boundary condition is then derived using bounds obtained from a key energy dissipation formula (Lemma 4.3.1). For Theorem 4.2.2, in order to connect the finite- and infinite-dimensional variables of both systems, we define piecewise-affine and piecewise-continous interpolates of the N-link system variables (position, orientation, force and moments) and derive uniform bounds in N for each of them. In most cases, these bounds are a direct consequence of the energy dissipation estimate. Interestingly, the

discrete tangent vector $e_\parallel$, which encapsulates the inextensibility condition, requires strong convergence in $L^2((0,T);L^4(0,L))$, where $T>0$ is any fixed time and L stands for the length of the filament, which we obtain as an application of the Aubin-Lions-Simon lemma [14].

The paper is structured as follows. In Section 4.2, we describe the continuous model, its coarsed-grained N-link companion and state both Theorems mentioned above. Section 4.3 is dedicated to establishing the energy dissipation formula. Relying on this, the proofs of Theorems 4.2.1 and 4.2.2 are conducted respectively in Sections 4.4 and 4.5. Finally, we discuss the results and list a few open problems in Section 4.6.

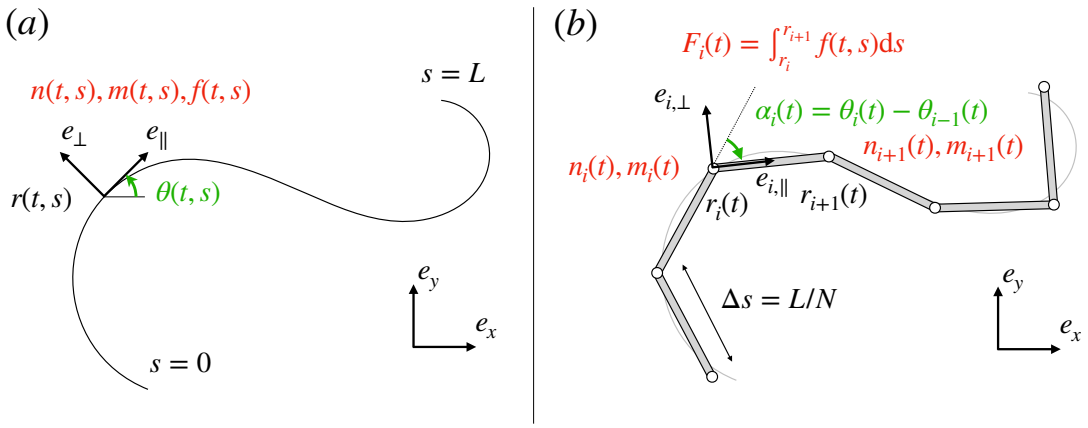

Figure 4.1. Diagram and notations for (a) the continuous elastohydrodynamic flagellum model and (b) the N-link model.

4.2 *Problem formulation and main results*

4.2.1 *Continuous model*

We consider a passive inextensible elastic filament of length $L>0$ undergoing planar deformations in a fluid at a low Reynolds number, parametrized by

$$r:\begin{cases}\mathbb{R}_+\times[0,L]\to\mathbb{R}^2\\ (t,s)\mapsto r(t,s)\end{cases}$$

where s is the filament arclength and t the time, as shown in Figure 4.1(a). Two types of forces are experienced by the filament: contact forces $n(t,s)$ inside the filament, and external forces, characterized by a force density $f(t,s)$, along with contact moments $m(t,s)$. The filament is then classically defined by the following system of equations [13]

$$\begin{cases} n_s+f=0,\\ m_s+r_s\times n=0,\\ m=E\theta_s e_z=Er_{ss}\times r_s,\\ |r_s|^2=1,\end{cases}$$

where $\theta(t,s)$ is defined as the angle between the x axis and the tangent vector to the filament $e_\parallel$, with $e_\parallel = r_s(t,s) := \dfrac{\partial r}{\partial s}(t,s)$, and contact moments are linked to the angle via a bending stiffness $E > 0$. The first two equations are the force and torque balance on the system, and external moments are neglected. The filament is supposed to be inextensible, unshearable and hyperelastic. The bending moment is thus linearly related to the local curvature, hence the third equation, while the fourth one models the inextensibility.

Using Resistive Force Theory, the density of external forces can be expressed as:

$$f(t,s) = -c_\perp (e_\perp \cdot \dot{r}) e_\perp - c_\parallel (e_\parallel \cdot \dot{r}) e_\parallel = \mathbf{C}(\theta(t,s))\dot{r}, \tag{4.1}$$

with $e_\parallel = (\cos(\theta), \sin(\theta))^\intercal$, $e_\perp = (-\sin(\theta), \cos(\theta))^\intercal$ and where $c_\parallel > 0$ and $c_\perp > 0$ such that $c_\parallel \neq c_\perp$ are the parallel and perpendicular drag coefficients, respectively, $\dot{r}(t,s) := \dfrac{\partial r}{\partial t}(t,s)$. Finally,

$$\mathbf{C}(\theta) = -\left[c_\perp \begin{pmatrix} -\sin\theta \\ \cos\theta \end{pmatrix} \Big(-\sin\theta\,,\, \cos\theta \Big) + c_\parallel \begin{pmatrix} \cos\theta \\ \sin\theta \end{pmatrix} \Big(\cos\theta\,,\, \sin\theta \Big) \right] \tag{4.2}$$

is a negative definite 2×2 matrix, depending regularly on the variable θ.

To end the description of the model, it remains to choose the boundary conditions at $s = 0$ and $s = L$ for any time $t > 0$. While the filament remains free in $s = L$ (i.e. $n(t,L) = 0$ and $m(t,L) = 0$), we investigate various configurations for the other end $s = 0$:

- ◇ Either the filament is *free*, i.e. $n(t,0) = 0$ and $m(t,0) = 0$;
- ◇ Or the filament is *pinned*, meaning $m(t,0) = 0$ and $\dot{r}(t,0) = 0$. In this case, the extremity is fixed but the filament is free to rotate around it;
- ◇ Or it can also be *clamped*, i.e. $\dot{r}(t,0) = 0$ and $\dot{\theta}(t,0) = 0$. The extremity has a fixed position and orientation.

The following system of equations is presented for a filament *free* at both ends but can then be adapted accordingly, by changing the third and fourth lines of equations. The continuous model thus finally reads

$$\begin{cases} n_s + \mathbf{C}(\theta)\dot{r} = 0, \\ m_s + r_s \times n = 0, \\ n(0) = n(L) = 0, \\ m(0) = m(L) = 0, \\ m = E\theta_s e_z = E r_{ss} \times r_s, \\ |r_s|^2 = 1. \end{cases} \tag{4.3}$$

4.2.2 *N-link model*

We now introduce the discrete filament model, the N-link swimmer [2], [75], shown in Figure 4.1(b). The swimmer, embedded in the fluid, is composed of N discrete segments of size $\Delta s = L/N$, and can be interpreted as a coarse-grained version of Figure 4.1(a). The extremities of the i-th segment, for $1 \leq i \leq N$, are at positions $r_i(t)$ and $r_{i+1}(t)$. The unit vector parallel to the i-th segment is then defined by $e_{i,\parallel}(t) = \dfrac{r_{i+1}(t) - r_i(t)}{\Delta s} = (\cos\theta_i(t)\,,\,\sin\theta_i(t))^\intercal$, calling θ_i the angle between e_x and $e_{i,\parallel}$. At each point $r_i(t)$, we define a contact moment $m_i(t)$ and a contact force (on the $(i-1)$-th link) $n_i(t)$. The relation between the angles and the elastic torque, and the inextensibility condition, then read

$$\begin{cases} m_{i+1}(t) = \kappa(\theta_{i+1}(t) - \theta_i(t))e_z, & 1 \leq i \leq N-1, \\ \dfrac{|r_{i+1}(t) - r_i(t)|}{\Delta s} = 1, & 1 \leq i \leq N, \end{cases}$$

where the elastic constant is defined as $\kappa = E/\Delta s$ in order to be consistent with the previous continuous model. Here, although in $e_{i,\parallel}$, the θ_is are defined modulo 2π, in the equation on m_{i+1}, the choice of a representative for θ_i modulo 2π is essential.

We call $f_{\text{ext},i}(t)$ the external fluid force exerted on the $i-$th segment. In order to compute it using the Resistive Force Theory (see (4.1)), we parametrize the swimmer using its arclength coordinate as

$$r^h(t,s) = r_i(t) + (s - (i-1)\Delta s)\frac{r_{i+1}(t) - r_i(t)}{\Delta s}, \tag{4.4}$$

for $s \in L_i = [(i-1)\Delta s, i\Delta s]$ and $1 \leq i \leq N$, which is the linear interpolate between $r_i(t)$ and $r_{i+1}(t)$ on the i-th segment. Then, $f_{\text{ext},i}$ is given by

$$\begin{aligned} f_{\text{ext},i}(t) &= \int_{L_i} \mathbf{C}(\theta_i)\ \dot{r}^h(t,s)\ \mathrm{d}s \\ &= \Delta s\ \mathbf{C}(\theta_i)\ \dot{r}_{i+\frac{1}{2}}(t)\,, \end{aligned}$$

where we used the notation $r_{i+1/2} = \dfrac{r_i + r_{i+1}}{2}$, and the force balance on the i-th segment reads

$$\Delta s\, \mathbf{C}(\theta_i)\, \dot{r}_{i+\frac{1}{2}}(t) + n_{i+1}(t) - n_i(t) = 0. \tag{4.5}$$

Similarly, the external fluid torque can be computed as (omitting the dependence in time for brevity)

$$\begin{aligned} m_{\mathrm{ext},i} &= \int_{L_i} r^h \times \mathbf{C}(\theta_i)\,\dot{r}^h \,\mathrm{d}s \\ &= \int_{L_i} (r^h - r_{i+1/2}) \times \mathbf{C}(\theta_i)\,(\dot{r}^h - \dot{r}_{i+1/2}) \,\mathrm{d}s + \Delta s\, r_{i+1/2} \times \mathbf{C}(\theta_i)\,\dot{r}_{i+1/2} \\ &= \int_{L_i} (r_{i+1} - r_i) \times \mathbf{C}(\theta_i)\,(\dot{r}_{i+1} - \dot{r}_i) \left(\frac{1}{2} + \frac{s-(i-1)\Delta s}{\Delta s}\right) \mathrm{d}s + \Delta s\, r_{i+1/2} \times \mathbf{C}(\theta_i)\,\dot{r}_{i+1/2} \\ &= -\frac{\Delta s^3}{12} c_\perp \dot{\theta}_i e_z + \Delta s\, r_{i+1/2} \times \mathbf{C}(\theta_i)\,\dot{r}_{i+1/2} \end{aligned}$$

and the torque balance equation on the $i-$th segment then reads

$$-\frac{\Delta s^3}{12} c_\perp \dot{\theta}_i e_z + \Delta s\, r_{i+1/2} \times \mathbf{C}(\theta_i)\,\dot{r}_{i+1/2} + m_{i+1} - m_i + r_{i+1} \times n_{i+1} - r_i \times n_i = 0\,.$$

Using the force balance equation (4.5), together with the definition of $e_{i,\parallel}$, this simplifies to

$$m_{i+1} - m_i + \Delta s\, e_{i,\parallel} \times \frac{n_{i+1}+n_i}{2} - \frac{\Delta s^3}{12} c_\perp \dot{\theta}_i e_z = 0\,.$$

To complete the system, there remains to choose the boundary conditions for the N-link swimmer at any time $t > 0$. We always consider the swimmer free at one end, more specifically, $m_{N+1}(t) = 0$ and $n_{N+1}(t) = 0$. As for the continuous filament, we investigate three types of boundary conditions for the N-link swimmer

- ◇ Either the swimmer is *free*, i.e. $n_1(t) = 0$ and $m_1(t) = 0$;
- ◇ Or the N-link swimmer is *pinned*, meaning $m_1(t) = 0$ and $\dot{r}_1(t) = 0$;
- ◇ Or it can also be *clamped*, i.e. $\dot{r}_1(t) = 0$ and $\dot{\theta}_1(t) = 0$.

Finally, collecting the preceding equations, the complete system for the $N-$link swimmer reads as, for *free* boundary conditions at both ends

$$\begin{cases} n_{i+1} - n_i + \Delta s\, \mathbf{C}(\theta_i)\,\dot{r}_{i+1/2} = 0, & 1 \le i \le N, \\ m_{i+1} - m_i + \Delta s\, e_{i,\parallel} \times \dfrac{n_{i+1}+n_i}{2} - \dfrac{\Delta s^3}{12} c_\perp \dot{\theta}_i e_z = 0, & 1 \le i \le N, \\ n_1 = n_{N+1} = 0, & \\ m_1 = m_{N+1} = 0, & \\ m_{i+1} = \dfrac{E}{\Delta s}(\theta_{i+1} - \theta_i) e_z, & 1 \le i \le N-1, \\ \dfrac{|r_{i+1} - r_i|}{\Delta s} = 1, & 1 \le i \le N. \end{cases} \tag{4.6}$$

The system of equations (4.6) can easily be written for *pinned* or *clamped* boundary conditions, by replacing the third and fourth lines of equations.

Using the definitions of $(\theta_i)_i$ and $(e_{i,\parallel})_i$, one can also rewrite the N-link system in matrix form, which will be useful in Section 4.4. Indeed, for $2 \leq i \leq N+1$, let us notice that r_i can be explicitly written in terms of r_1 and $(\theta_j)_j$ as

$$r_i = r_1 + \Delta s \sum_{k=1}^{i-1} \begin{pmatrix} \cos\theta_k \\ \sin\theta_k \end{pmatrix} =: R_i((\theta_j)_j, r_1). \tag{4.7}$$

The functions R_i depend analytically on their parameters which entails in particular $\dot{r}_i = \dot{r}_1 + \sum_{k=1}^{i-1} \frac{\partial R_i}{\partial \theta_k}\dot{\theta}_k$, or, in other words, that $\dot{r}_i$ depends linearly on $\dot{r}_1$ and $(\dot{\theta}_j)_j$, with coefficients that are still analytic in r_1 and $(\theta_j)_j$.

The system (4.6) with *free* boundary conditions can then be rewritten as

$$\begin{cases} n_{i+1} - n_i + \Delta s \mathbf{C}(\theta_i)\,\dot{r}_{i+1/2} = 0, & 1 \leq i \leq N, \\ (m_{i+1} - m_i)\cdot e_z + \Delta s e_{i,\parallel} \times \dfrac{n_{i+1}+n_i}{2} \cdot e_z - \dfrac{\Delta s^3}{12} c_\perp \dot{\theta}_i = 0, & 1 \leq i \leq N, \\ n_1 = 0, & \\ m_1 \cdot e_z = 0, & \\ m_{i+1}\cdot e_z = \dfrac{E}{\Delta s}(\theta_{i+1} - \theta_i), & 1 \leq i \leq N-1, \end{cases} \tag{4.8}$$

where the inextensibility condition is enforced by (4.7), and n_1 and $m_1 \cdot e_z$ can be replaced with any other chosen boundary condition. Supposing that r_i, $i > 1$ are given by (4.7), they can be removed from the unknowns in (4.6). Similarly, since $n_{N+1} = m_{N+1} \cdot e_z = 0$, they are also removed from the unknowns, and the remaining unknowns in system (4.8) are thus $r_1 \in C^1(\mathbb{R}_+)^2$, $(\theta_i)_i \in C^1(\mathbb{R}_+)^N$, $(n_i)_i \in C^1(\mathbb{R}_+)^{2N+2}$ and $(m_i \cdot e_z)_i \in C^1(\mathbb{R}_+)^{N+1}$. This final form of the system of equations characterizing the N-link clearly looks like a discrete version of the continuous system (4.3), although it does not directly arise from a discretisation of (4.3).

To finish this section, let us rewrite system (4.8) in matrix form. This is done here for *free* boundary conditions, but can easily be adapted to the other two presented in this paper. We first introduce the vector collecting the unknowns $\mathbf{X} = (\theta_1, \ldots, \theta_N, r_1^x, r_1^y)^\intercal$ where $(r_1^x, r_1^y)^\intercal = r_1$ projected along e_x and e_y. The middle points' coordinates therefore satisfy $\dot{r}_{i+1/2} = (G\dot{\mathbf{X}})_i$ where for any $X = (X_i)_i \in \mathbb{R}^{N+2}$ and $1 \leq i \leq N$, the matrix G is of size $(2N, N+2)$ and defined as

$$(GX)_i = \begin{pmatrix} X_{N+1} \\ X_{N+2} \end{pmatrix} + \Delta s \sum_{k=1}^{i-1} \begin{pmatrix} -\sin\theta_k \\ \cos\theta_k \end{pmatrix} X_k + \frac{\Delta s}{2} \begin{pmatrix} -\sin\theta_i \\ \cos\theta_i \end{pmatrix} X_i \in \mathbb{R}^2. \tag{4.9}$$

Setting $\mathbf{N} = (n_1^x, n_1^y, \ldots, n_N^x, n_N^y)^\intercal$, $\mathbf{M} = (m_1 \cdot e_z, \ldots, m_N \cdot e_z)^\intercal$, and recalling that $\dot{\mathbf{X}} = (\dot{\theta}_1, \ldots, \dot{\theta}_N, \dot{r}_1^x, \dot{r}_1^y)^\intercal$, the system (4.8) can be rewritten as the following differential-

algebraic system of linear equations, using the fact that for any $u \in \mathbb{R}^2$ and $1 \leq i \leq N$, $e_{i,\parallel} \times u \cdot e_z = e_{i,\perp} \cdot u$.

$$\begin{pmatrix} A_{11} & A_{12} & 0_{2N,N} \\ A_{21} & A_{22} & A_{23} \\ 0_{N,2N} & 0_{N,N+2} & I_N \end{pmatrix} \begin{pmatrix} \mathbf{N} \\ \dot{\mathbf{X}} \\ \mathbf{M} \end{pmatrix} = \begin{pmatrix} F_1 \\ F_2 \\ F_3 \end{pmatrix}, \tag{4.10}$$

where

$$A_{11} = \begin{pmatrix} -I_2 & I_2 & \cdots & \cdots & 0_2 \\ 0_2 & -I_2 & I_2 & \cdots & 0_2 \\ \vdots & \ddots & \ddots & \ddots & \vdots \\ \vdots & \ddots & \ddots & \ddots & \vdots \\ 0_2 & \cdots & \cdots & 0_2 & -I_2 \end{pmatrix}, \; A_{12} = \Delta s \, \mathbb{C} G \,,$$

$$A_{21} = \frac{\Delta s}{2} \begin{pmatrix} e_{1,\perp}^\intercal & e_{1,\perp}^\intercal & 0_2 & \cdots & 0_2 \\ 0_2 & e_{2,\perp}^\intercal & e_{2,\perp}^\intercal & \cdots & 0_2 \\ \vdots & \ddots & \ddots & \ddots & \vdots \\ 0_2 & \cdots & \cdots & e_{n,\perp}^\intercal & 0_2 \\ I_2 & 0_2 & \cdots & \cdots & 0_2 \end{pmatrix}, \; A_{22} = -\frac{\Delta s^3}{12} c_\perp \begin{pmatrix} 1 & & & & \\ & \ddots & & & \\ & & 1 & & \\ & & & 0 & \\ & & & & 0 \end{pmatrix},$$

$$A_{23} = \begin{pmatrix} -1 & 1 & 0 & \cdots & 0 \\ 0 & -1 & 1 & \cdots & 0 \\ \vdots & \ddots & \ddots & \ddots & \vdots \\ 0 & \cdots & \cdots & -1 & 0 \\ 0 & \cdots & \cdots & \cdots & 0 \end{pmatrix},$$

and

$$F_1 = 0_{2N}, \; F_2 = 0_{N+2}, \; F_3 = \frac{E}{\Delta s}(0, \theta_2 - \theta_1, \cdots, \theta_N - \theta_{N-1})^\intercal \,.$$

4.2.3 *Statement of the main results*

Obviously, the discrete system (4.8) resembles the continuous one (4.3). The goal of the paper is to show that the dynamics of the discrete system converges as Δs tends to 0 (or equivalently N tends to $+\infty$) to the one of the continuous one. In order to formalize the result, let us first introduce the interpolates in space associated to all relevant quantities in the N-link swimmer, in order to formally state its convergence towards the continuous filament. The first interpolates are built using continuous and piecewise linear functions ϕ_i, defined in $H^1(0,L) = \{u \in L^2(0,L) \,|\, u_s \in L^2(0,L)\}$ by $\phi_i(j\Delta s) = \delta_{i-1,j}$ for $i = 1, \cdots, N+1$ and $j = 0, \cdots, N$. We thus place ourselves in $\mathcal{V}_h = \text{Span}((\phi_i)_{1 \leq i \leq N+1}) = \{v_h \in \mathcal{C}^0(0,L) \,|\, v_h \text{ affine on } [(i-1)\Delta s, i\Delta s] \text{ for } 1 \leq i \leq N\}$,

with $h = \Delta s$. We then introduce the following linear interpolates, for $T > 0$ and $(t, s) \in Q_T = [0, T] \times [0, L]$

$$r^h(t,s) = \sum_{i=1}^{N+1} r_i(t)\phi_i(s), \tag{4.11}$$

$$m^h(t,s) = \sum_{i=1}^{N+1} m_i(t)\phi_i(s), \tag{4.12}$$

$$n^h(t,s) = \sum_{i=1}^{N+1} n_i(t)\phi_i(s), \tag{4.13}$$

$$\theta^h(t,s) = \sum_{i=1}^{N} \theta_i(t)\phi_{i+1}(s) + \theta_1(t)\phi_1(s). \tag{4.14}$$

Notice that (4.11) is nothing but a rewriting of (4.4). Notice also that $r_s^h(t,s) = \dfrac{r_{i+1}(t) - r_i(t)}{\Delta s}$ for $s \in [(i-1)\Delta s, i\Delta s]$, from which we deduce that $|r_s^h(t,s)|^2 = 1$ by construction. Lastly, we also define the piecewise constant interpolates

$$\bar{\theta}^h(t,s) = \sum_{i=1}^{N} \theta_i(t)\mathbb{1}_{L_i}(s), \tag{4.15}$$

$$\bar{m}^h(t,s) = \sum_{i=1}^{N} m_i(t)\mathbb{1}_{L_i}(s). \tag{4.16}$$

From these definitions, we recover in particular $\bar{m}^h = E\theta_s^h e_z$. The two following theorems constitute the main results of this paper, guaranteeing both the well-posedness of the N-link equations, as well as its convergence towards the system of equations characterizing a continuous filament.

THEOREM 4.2.1 · *Well-posedness for the N-link swimmer*

The discrete system (4.8), given a set of initial conditions $r_1^0 \in \mathbb{R}^2$, $(\theta_i^0)_{1\le i\le N} \in \mathbb{R}^N$ admits a unique solution $r_1 \in C^1(\mathbb{R}_+)^2$, $(\theta_i)_{1\le i\le N} \in C^1(\mathbb{R}_+)^N$.

Let $r_1 \in C^1(\mathbb{R}_+)^2, (\theta_i)_{1\le i\le N} \in C^1(\mathbb{R}_+)^N, (m_i)_{1\le i\le N+1} \in C^1(\mathbb{R}_+)^{2N+2}, (n_i)_{1\le i\le N+1} \in C^1(\mathbb{R}_+)^{2N+2}$ be a solution to system (4.8), with initial conditions $r_1^0 \in \mathbb{R}^2$, $(\theta_i^0)_{1\le i\le N} \in \mathbb{R}^N$. This solution exists thanks to Theorem 4.2.1, and r_1, $(\theta_i)_{1\le i\le N}$, $(m_i)_{1\le i\le N+1}$ and $(n_i)_{1\le i\le N+1}$ can be interpolated using definitions (4.11 – 4.16) and equation (4.7). Its interpolates are then denoted as $(r^h, m^h, n^h, \bar{m}^h)$.

THEOREM 4.2.2 · *Convergence*

If $(\theta_s^h(0,\cdot))_h$ is bounded uniformly h in $L^2(0,L)$, then the interpolates $(r^h, m^h, n^h, \bar{m}^h)_h$ is bounded in $H^1(Q_T) \times L^2((0,T); H^1(0,L))^2 \times$

$L^2((0,T);BV(0,L))$. Moreover, when $h \to 0$, we have that, up to extraction of a subsequence,

$$\begin{aligned} &r^h \rightharpoonup r \text{ weakly in } H^1(Q_T),\\ &m^h \rightharpoonup m \text{ weakly in } L^2((0,T);H^1(0,L)),\\ &n^h \rightharpoonup n \text{ weakly in } L^2((0,T);H^1(0,L)),\\ &\bar{m}^h \rightharpoonup m \text{ weakly in } L^2(Q_T), \end{aligned}$$

where $(r,\, m,\, n)$ are solutions to the equations of an elastic filament (4.3).

Remark 4.2.1. Theorem 4.2.2 gives a solution to (4.3) without any initial condition. Therefore, it does not guarantee the existence of a solution to the continuous system given a set of initial conditions.

Remark 4.2.2. The result given by Theorem 4.2.2 is only up to extraction of subsequences for each sequence of interpolates, as the uniqueness of the solutions to System (4.3) is not guaranteed.

Remark 4.2.3. The hypothesis from Theorem 4.2.2 on $(\theta_s^h(0,\cdot))_h$ means that its limit $\theta_s(0,\cdot)$ in $L^2(0,L)$ is at least bounded in $L^2(0,L)$. At the level of the interpolates, if $(\theta_s^h(0,\cdot))_h$ is uniformly bounded in h in $L^2(0,L)$, then $(\theta_s^h)_h$ is also uniformly bounded in h in $L^2(Q_T)$.

4.3 *Energy dissipation*

The following result materializes energy dissipation in the N-link system of equations (4.8). This result is the key to proving both theorems, as well as a warranty that the N-link swimmer is consistent from the point of view of physics, as it provides some natural bounds on relevant quantities in the system, first introduced in Section 4.4, when proving Lemma 4.4.1.

Lemma 4.3.1 (Energy dissipation law).

Any solution $(r_i)_{1\le i\le N+1} \in C^1(\mathbb{R}_+)^{2N+2}$, $(\theta_i)_{1\le i\le N} \in C^1(\mathbb{R}_+)^N$, $(m_i)_{1\le i\le N+1} \in C^1(\mathbb{R}_+)^{2N+2}$,$(n_i)_{1\le i\le N+1} \in C^1(\mathbb{R}_+)^{2N+2}$ to the discrete system (4.8), also satisfy the following energy dissipation equation

$$\frac{1}{2}\frac{\mathrm{d}}{\mathrm{d}t}\left[E\sum_{i=1}^{N-1}\Delta s\left(\frac{\theta_{i+1}-\theta_i}{\Delta s}\right)^2\right]+\sum_{i=1}^{N}\frac{\Delta s^3}{12}c_\perp\dot{\theta}_i^2-\sum_{i=1}^{N}\Delta s\,\mathbf{C}(\theta_i)\,\dot{r}_{i+\frac{1}{2}}\cdot\dot{r}_{i+\frac{1}{2}}=0\,. \quad (4.17)$$

Proof. Multiplying the force balance equation (4.5) by the velocity $\dot{r}_{i+\frac{1}{2}}$, and summing over $i = 1, \cdots, N$ leads to

$$\begin{aligned}\Delta s \sum_{i=1}^{N} \mathbf{C}(\theta_i)\, \dot{r}_{i+\frac{1}{2}} \cdot \dot{r}_{i+\frac{1}{2}} &= -\sum_{i=1}^{N} \dot{r}_{i+\frac{1}{2}} \cdot (n_{i+1} - n_i)\, \mathrm{d}s \\ &= \sum_{i=1}^{N} (\dot{r}_{i+1} - \dot{r}_i) \cdot \frac{n_{i+1} + n_i}{2},\end{aligned}$$

using a summation by parts and the boundary conditions $n_1 = n_{N+1} = 0$ (notice that this remains true if we use the boundary condition $\dot{r}_1 = 0$ instead of $n_1 = 0$). But, since $r_{i+1} - r_i = \Delta s\, e_{i,\parallel}$, we have $\dot{r}_{i+1} - \dot{r}_i = \Delta s\, \dot{\theta}_i e_{i,\perp}$, from which we deduce

$$\begin{aligned}\Delta s \sum_{i=1}^{N} \mathbf{C}(\theta_i)\, \dot{r}_{i+\frac{1}{2}} \cdot \dot{r}_{i+\frac{1}{2}} &= \Delta s \sum_{i=1}^{N} \dot{\theta}_i e_{i,\perp} \cdot \frac{n_{i+1} + n_i}{2} \\ &= \Delta s \sum_{i} \dot{\theta}_i e_z \cdot e_{i,\parallel} \times \frac{n_{i+1} + n_i}{2} \\ &= \sum_{i=1}^{N} \dot{\theta}_i e_z \cdot \left[m_i - m_{i+1} + \frac{\Delta s^3}{12} c_\perp \dot{\theta}_i e_z \right] \\ &= \sum_{i=1}^{N} \frac{\Delta s^3}{12} c_\perp \dot{\theta}_i^2 + \sum_{i=1}^{N} \dot{\theta}_i e_z \cdot (m_i - m_{i+1}) \\ &= \sum_{i=1}^{N} \frac{\Delta s^3}{12} c_\perp \dot{\theta}_i^2 + \sum_{i=2}^{N} (\dot{\theta}_i - \dot{\theta}_{i-1}) e_z \cdot m_i\,,\end{aligned}$$

thanks to the moment balance equation (4.8), and the boundary conditions $m_1 = m_{N+1} = 0$ (notice that this also remains true if we use the boundary condition $\dot{\theta}_1 = 0$ instead of $m_1 = 0$). Now, observing that we have $m_i \cdot e_z = \frac{E}{\Delta s}(\theta_i - \theta_{i-1})$ for $i = 2, \cdots, N$, we deduce

$$\frac{E}{\Delta s} \sum_{i=1}^{N-1} (\dot{\theta}_i - \dot{\theta}_{i-1})(\theta_i - \theta_{i-1}) + \sum_{i=1}^{N} \frac{\Delta s^3}{12} c_\perp \dot{\theta}_i^2 - \Delta s \sum_{i=1}^{N} \mathbf{C}(\theta_i)\, \dot{r}_{i+\frac{1}{2}} \cdot \dot{r}_{i+\frac{1}{2}} = 0$$

which directly leads to equation (4.17). □

Remark 4.3.1. Recalling from (4.9) that $\dot{r}_{i+\frac{1}{2}}$ depends linearly on $\dot{\mathbf{X}} = \left(\dot{\theta}_1, \ldots, \dot{\theta}_N, \dot{r}_1^x, \dot{r}_1^y\right)^\intercal$, the energy estimate can also be rewritten in matrix form, using the definition of G from equation (4.9)

$$\frac{1}{2}\frac{\mathrm{d}}{\mathrm{d}t}\left[E \sum_{i=1}^{N-1} \Delta s \left(\frac{\theta_{i+1} - \theta_i}{\Delta s} \right)^2 \right] + \dot{\mathbf{X}}^\intercal M((\theta_i)_i, r_1)\dot{\mathbf{X}} = 0, \tag{4.18}$$

where $M := M_1 + M_2$ with

$$M_1 = \frac{\Delta s^3}{12} c_\perp \begin{pmatrix} 1 & & & & \\ & \ddots & & & \\ & & 1 & & \\ & & & 0 & \\ & & & & 0 \end{pmatrix}, \; M_2 = -\Delta s G^\intercal \mathbb{C} G, \tag{4.19}$$

and $\mathbb{C}$ is the block diagonal matrix defined by $\mathbb{C} = \mathrm{diag}(\mathbf{C}(\theta_1), \ldots, \mathbf{C}(\theta_N))$.

4.4 *Proof of Theorem 4.2.1 (Well-posedness for the N-link swimmer)*

We first present a proof of local in time well posedness of the system of equations (4.8) for an N-link swimmer with *free* boundary conditions at both ends, before globalizing the results in time. The other boundary conditions are then discussed.

Local in time existence and uniqueness for *free* boundary conditions. Let $N \in \mathbb{N}^*$, and let us prove that, for a set of initial conditions $(\theta_1^0, \ldots, \theta_N^0, r_1^{x,0}, r_1^{y,0}) \in \mathbb{R}^{N+2}$, System (4.8) admits a unique solution $(\theta_1, \ldots, \theta_N, r_1^x, r_1^y)$ in $C^1([0,T])^{N+2}$ for $T > 0$ sufficiently small. Setting $n_{N+1} = 0$ and $m_{N+1} \cdot e_z = 0$ for all time, we recall the matrix formulation of the N-link system from equation (4.10)

$$\begin{pmatrix} A_{11} & A_{12} & 0_{2N,N} \\ A_{21} & A_{22} & A_{23} \\ 0_{N,2N} & 0_{N,N+2} & I_N \end{pmatrix} \begin{pmatrix} \mathbf{N} \\ \dot{\mathbf{X}} \\ \mathbf{M} \end{pmatrix} = \begin{pmatrix} F_1 \\ F_2 \\ F_3 \end{pmatrix}.$$

In order to proceed, and show existence and uniqueness of solutions locally in time, we notice that the time derivatives only appear in $\dot{\mathbf{X}}$. Since (4.10) is an algebro-differential system, in order to be able to use Cauchy-Lipschitz Theorem, we rewrite the system in a fully differential way

$$B(\mathbf{X})\dot{\mathbf{X}} = \tilde{F}(\mathbf{X}) \tag{4.20}$$

where B is invertible and Lipschitz continous in $\mathbf{X} = (\theta_1, \cdots, \theta_N, r_1^x, r_1^y)^\intercal$, and $\tilde{F}$ is also Lipschitz continuous in $\mathbf{X}$. Then, Cauchy-Lipschitz theorem applied on equation (4.20) enables us to conclude. The proof follows two steps:

Step 1. We first notice that the matrix $\begin{pmatrix} A_{11} & 0_{2N,N} \\ 0_{N,2N} & I_N \end{pmatrix}$ is block diagonal and clearly invertible. Therefore,

$$B = A_{22} - (A_{21}\, A_{23}) \begin{pmatrix} A_{11} & 0_{2N,N} \\ 0_{N,2N} & I_N \end{pmatrix}^{-1} \begin{pmatrix} A_{12} \\ 0_{N,N+2} \end{pmatrix} = A_{22} - A_{21} A_{11}^{-1} A_{12}$$

and

$$\tilde{F} = F_2 - A_{23}F_3 - A_{21}A_{11}^{-1}F_1 = -A_{23}F_3$$

are well defined and are indeed Lipschitz continuous in $\mathbf{X}$.

Step 2. The matrix B is invertible if and only if $A = (A_{ij})_{1\leq i,j\leq 3}$ is invertible. But A is a square matrix of size $(4N+2)\times(4N+2)$, and it is enough to prove that the matrix is one-to-one.

Hence, we consider $X \in \mathbb{R}^{2N}$, $Y \in \mathbb{R}^{N+2}$ and $Z \in \mathbb{R}^N$ such that

$$\begin{pmatrix} A_{11} & A_{12} & 0_{2N,N} \\ A_{21} & A_{22} & A_{23} \\ 0_{N,2N} & 0_{N,N+2} & I_N \end{pmatrix} \begin{pmatrix} X \\ Y \\ Z \end{pmatrix} = 0_{4N+2}\,, \tag{4.21}$$

and prove that, necessarily, $X = 0_{2N}$, $Y = 0_{N+2}$ and $Z = 0_N$. First of all, the last line directly gives $Z = 0_N$. Then, using the first and second lines, we have

$$\begin{cases} A_{11}X + A_{12}Y &= 0_{2N}\,, \\ A_{21}X + A_{22}Y &= 0_{N+2}\,. \end{cases} \tag{4.22}$$

Since A_{11} is invertible, this can also be rewritten as $(A_{22} - A_{21}A_{11}^{-1}A_{12})Y = 0$. Writing the coefficients as $X = (X_i)_i \in \mathbb{R}^{2N}$ and $Y = (Y_i)_i \in \mathbb{R}^{N+2}$, we first notice that the $(N+1)$th and $(N+2)$th lines of $A_{21}X + A_{22}Y = 0_{N+2}$ read $X_1 = 0_2$. Then, since $(A_{22} - A_{21}A_{11}^{-1}A_{12})Y = 0_{N+2}$, we have

$$\begin{aligned} 0 &= Y^{\mathsf{T}}(A_{22} - A_{21}A_{11}^{-1}A_{12})Y \\ &= Y^{\mathsf{T}}(A_{21}X + A_{22}Y) \\ &= \sum_{i=1}^{N} \Delta s\, Y_i \begin{pmatrix} -\sin\theta_i \\ \cos\theta_i \end{pmatrix} \cdot \frac{X_{i+1}+X_i}{2} + \frac{\Delta s}{2}\, Y_N \begin{pmatrix} -\sin\theta_N \\ \cos\theta_N \end{pmatrix} \cdot X_N - \sum_{i=1}^{N} \frac{\Delta s^3}{12} c_\perp Y_i^2\,. \end{aligned}$$

Hence, using the properties of the vector product, G as introduced in equation (4.9), and once again that $X_1 = (0,0)^{\mathsf{T}}$, one has, by summation by parts,

$$\begin{aligned} 0 &= \frac{\Delta s}{2} \sum_{i=2}^{N} X_i \cdot \left(Y_{i-1} \begin{pmatrix} -\sin\theta_{i-1} \\ \cos\theta_{i-1} \end{pmatrix} + Y_i \begin{pmatrix} -\sin\theta_i \\ \cos\theta_i \end{pmatrix} \right) - \sum_{i=1}^{N} \frac{\Delta s^3}{12} c_\perp Y_i^2 \\ &= \sum_{i=2}^{N} X_i \cdot ((GY)_i - (GY)_{i-1}) - \sum_{i=1}^{N} \frac{\Delta s^3}{12} c_\perp Y_i^2 \\ &= -\sum_{i=1}^{N} (X_{i+1} - X_i) \cdot (GY)_i - \sum_{i=1}^{N} \frac{\Delta s^3}{12} c_\perp Y_i^2. \end{aligned}$$

Using $A_{11}X + A_{12}Y = 0$, we also have that for $1 \leq i \leq N$, $X_{i+1} - X_i = -\Delta s(\mathbb{C}GY)_i$ and we recover equation (4.18)

$$0 = \sum_{i=1}^{N} \Delta s(\mathbb{C}GY)_i \cdot (GY)_i - \sum_{i=1}^{N} \frac{\Delta s^3}{12} c_\perp Y_i^2.$$

By construction, $-\Delta s G^\intercal \mathbb{C} G$ is symmetric definite positive, since $\mathbb{C}$ is block diagonal with negative definite blocks. The preceding equation thus leads to $Y_i = 0$ and $(GY)_i = 0$ for all $i \in \{1, \cdots, N\}$. But, from (4.9), we deduce that

$$0 = (GY)_1 = \begin{pmatrix} Y_{N+1} \\ Y_{N+2} \end{pmatrix} + \frac{\Delta s}{2} \begin{pmatrix} -\sin\theta_1 \\ \cos\theta_1 \end{pmatrix} X_1 = \begin{pmatrix} Y_{N+1} \\ Y_{N+2} \end{pmatrix},$$

which finishes to proves that $Y = 0_{N+2}$. Finally, using $A_{11}X + A_{12}Y = 0_{2N}$ in (4.22), we deduce that $X = 0_{2N}$, A is injective and, eventually, that B is invertible.

In conclusion, the Cauchy-Lipschitz theorem can be applied to equation (4.20) and the system (4.8) with a set of initial conditions admits a unique C^1 solution $(\theta_1, \ldots, \theta_N, r_1)$ locally in time.

Global existence and uniqueness. The solution $(\theta_1, \ldots, \theta_N, r_1)$ to system (4.8) can be extended to $\mathbb{R}_+$ as long as they stay bounded at any time $t > 0$. The boundedness in time of $(\theta_1, \ldots, \theta_N, r_1)$ is ensured by the following lemma.

Lemma 4.4.1 (Bounds on $(r_i)_i$ and $(\theta_i)_i$).

Let $N \in \mathbb{N}^*$. For any $T > 0$, as long as all $(r_i)_{1\leq i\leq N+1}$ and $(\theta_i)_{1\leq i\leq N}$ exist on $[0, T[$, they stay bounded in $[0, T]$ in the following sense:

$$|r_i(t) - r_i(0)| \leq C_1 T^{1/2}, \tag{4.23}$$
$$|\theta_i(t) - \theta_i(0)| \leq C_2 T^{1/2}, \tag{4.24}$$

for all $1 \leq i \leq N$, for all $t \in [0, T]$, and where $C_1, C_2 > 0$ are constants that do not depend on T.

Proof. Let us take $T > 0$ and assume that the solution $(r_i)_{1\leq i\leq N+1}$ and $(\theta_i)_{1\leq i\leq N}$ exist on $[0, T[$. First of all, integrating equation (4.17) over time $t \in [0, T]$, we obtain

$$\frac{1}{2}\left[E \sum_{i=1}^{N-1} \Delta s \left(\frac{\theta_{i+1}(T) - \theta_i(T)}{\Delta s}\right)^2\right] + \int_0^T \sum_{i=1}^{N} \frac{\Delta s^3}{12} c_\perp \dot\theta_i^2(t)\,\mathrm{d}t - \int_0^T \sum_{i=1}^{N} \Delta s\, \mathbf{C}(\theta_i)\, \dot r_{i+\frac12}(t) \cdot \dot r_{i+\frac12}(t)\,\mathrm{d}t = C, \tag{4.25}$$

where the integrals on the left-hand side are all positive, and $C = \frac{1}{2}\left[E \sum_{i=1}^{N-1} \Delta s \left(\frac{\theta_{i+1}(0) - \theta_i(0)}{\Delta s}\right)^2\right] > 0$ is a constant. We thus deduce that

$$\int_0^T \sum_{i=1}^{N} \frac{\Delta s^3}{12} c_\perp \dot\theta_i^2\,\mathrm{d}t \leq C. \tag{4.26}$$

Similarly, using the fact that $\mathbf{C}(\theta_i)$ is always negative and can be bounded from below for all i independently of N, leads to the following estimate

$$\int_0^T \sum_{i=1}^N \Delta s \, |\dot{r}_{i+1/2}|^2 \leq \tilde{C}, \tag{4.27}$$

where $\tilde{C} = C/\min(c_\parallel, c_\perp)$. Moreover, using the inextensibility condition as in (4.7), one can write $\dot{r}_{i+1} - \dot{r}_i = \Delta s \, \dot{\theta}_i e_{i,\perp}$. Hence,

$$\int_0^T \sum_{i=1}^N \Delta s \, |\dot{r}_{i+1} - \dot{r}_i|^2 = \int_0^T \sum_{i=1}^N \Delta s \, |\Delta s \, \dot{\theta}_i e_{i,\perp}|^2 = \int_0^T \sum_{i=1}^N \Delta s^3 \dot{\theta}_i^2 \leq \frac{12}{c_\perp} C. \tag{4.28}$$

Combining equations (4.27) and (4.28) on the $\dot{r}_i$s finally leads to

$$\int_0^T \sum_i \Delta s |\dot{r}_i(s)|^2 \, \mathrm{d}s \leq 4\tilde{C} + \frac{12}{c_\perp} C. \tag{4.29}$$

Finally, let us look at $r_i(t)$ for $1 \leq i \leq N+1$ and $t \in [0,T]$. We have that, using Cauchy-Schwarz inequalities, as well as equation (4.29) along with $\int_0^T |\dot{r}_i(s)|^2 \, \mathrm{d}s \leq \int_0^T \sum_j |\dot{r}_j(s)|^2 \, \mathrm{d}s$:

$$\begin{aligned} |r_i(t) - r_i(0)| = \left| \int_0^T \dot{r}_i(s) \, \mathrm{d}s \right| &\leq \int_0^T |\dot{r}_i(s)| \, \mathrm{d}s \\ &\leq T^{1/2} \left(\int_0^T |\dot{r}_i(s)|^2 \, \mathrm{d}s \right) \frac{1}{2} \leq T^{1/2} \frac{1}{\Delta s^{\frac{1}{2}}} \left(4\tilde{C} + \frac{12}{c_\perp} C \right)^{\frac{1}{2}}, \end{aligned}$$

which gives (4.23).

Let us now focus on the $(\theta_i)_i$. Similarly, let $t \in [0,T]$, we have that, using triangular inequality

$$|\theta_i(t) - \theta_i(0)| = \left| \int_0^t \dot{\theta}_i(s) \, \mathrm{d}s \right| \leq \int_0^T \left| \dot{\theta}_i(s) \right| \, \mathrm{d}s. \tag{4.30}$$

Using equation (4.26), the fact that $\frac{\Delta s}{12} c_\perp$ is fixed and $\int_0^T \left|\dot{\theta}_i(s)\right|^2 \mathrm{d}s \leq \int_0^T \sum_j |\dot{\theta}_j(s)|^2 \mathrm{d}s$, along with Cauchy-Schwarz inequality, we obtain for all $t \in [0, T]$

$$|\theta_i(t) - \theta_i(0)| \leq T^{1/2} \left(\int_0^T \left|\dot{\theta}_i(s)\right|^2 \mathrm{d}s \right)^{\frac{1}{2}} \leq T^{1/2} \left(\frac{12}{\Delta s^3 c_\perp} C \right)^{\frac{1}{2}}. \tag{4.31}$$

This gives (4.24) and concludes the proof. □

Lemma 4.4.1 thus guarantees that the solution $(\theta_1, \ldots, \theta_N, r_1)$ to system (4.8) can not blow up in finite time. The system (4.8) with initial conditions $(\theta_1^0, \ldots, \theta_N^0, r_1^0) \in \mathbb{R}^{N+2}$ therefore admits a unique solution for all time $(\theta_1, \ldots, \theta_N, r_1)$ in $C^1((\mathbb{R}_+)^{N+2})$, which concludes the proof of Theorem 4.2.1 in the case of *free* boundary conditions.

Remark 4.4.1. So, far, no assumptions have been made on the values the angles θ_i can take, meaning that the N-link could auto-intersect itself, just as a the continuous filament can.

Existence and uniqueness for *pinned* or *clamped* boundary conditions. When the N-link swimmer is *pinned* or *clamped*, for $t > 0$, $\dot{r}_1(t) = 0$, meaning that r_1 is no longer an unknown in the system. The proof of theorem 4.2.1 can thus be adapted by removing a set of two unknowns (i.e. $r_1^x(t)$ and $r_1^y(t)$) and by looking at the new matrix A of size $4N \times 4N$. The proof can then be carried on as above.

4.5 *Proof of theorem 4.2.2 (Convergence)*

We first recall the next two results, whose detailed proofs can directly be found in the associated references, and which will be used to prove Theorem 4.2.2.

Lemma 4.5.1 (Aubin-Lions-Simon [14], [23]).

Let $H_1 \subset H_2$ be two Banach spaces, and $T > 0$. Take a sequence $(u_n)_n$ bounded in $L^2((0,T); H_1)$ such that $(\dot{u}_n)_n$ is bounded in $L^2((0,T); H_2)$. Then, for any Banach space H such that $H_1 \subset H \subset H_2$, with H_1 compactly embedded in H and H continuously embedded in H_2, $(u_n)_n$ is relatively compact in $L^2((0,T); H)$.

Lemma 4.5.2 (Embedding in one dimension of functions with bounded variations – BV [39]).

Let $BV(0, L)$ be defined as the space of functions of bounded variation, equipped with the norm $\|u\|_{BV} = |u(0)| + TV(u)$, for $u \in BV(0, L)$, where $TV(u)$ is the total variation of u. Then, for all $1 \leq p < \infty$, $BV(0, L)$ is compactly embedded in $L^p(0, L)$.

In this section, we now fix a $T > 0$. The proof is decomposed into three propositions. We introduce the first proposition, which aim is to bound the interpolates in space and time r^h, $\bar{\theta}^h$, n^h and m^h defined in equations (4.11-4.16) independently of $h = \Delta s$ in the relevant function spaces. Then, we would like to ensure, using the next two propositions, the convergence of each of these interpolates as h goes to zero, towards a set of functions that is a solution to a weak form of system (4.3).

PROPOSITION 4.5.1 · *Bounds on interpolates*

If $(\theta_s^h(0,\cdot))_h$ is bounded uniformly h in $L^2(0,L)$, the interpolates defined in equations (4.11-4.16) satisfy the following bounds, uniformly in $h = \Delta s$

1. $(r^h)_h$ is bounded in $H^1(Q_T)$;
2. $(\dot{r}_s^h)_h$ is bounded in $L^2((0,T);H^{-1}(0,L))$;
3. $(r_s^h)_h$ is bounded in $L^2((0,T);BV(0,L))$;
4. $(n^h)_h$ is bounded in $L^2((0,T);H^1(0,L))$;
5. $(m^h)_h$ is bounded in $L^2((0,T);H^1(0,L))$;
6. $(\Delta s\,\dot{\bar{\theta}}^h)_h$ is bounded in $L^2(Q_T)$;
7. $(\theta_s^h)_h$ is bounded in $L^2(Q_T)$.

Proof. **1. Bounding $(r^h)_h$ in $H^1(Q_T)$.** We are looking for bounds of the $L^2(Q_T)$ norms of $(r^h)_h$, $(\dot{r}^h)_h$ and $(r_s^h)_h$. Since r^h is the piecewise linear interpolate of the $(r_i)_{1\le i\le N+1}$, $r_s^h(t,s) = \displaystyle\sum_{i=1}^{N} \frac{r_{i+1}(t)-r_i(t)}{\Delta s}\mathbb{1}_{L_i}$. The inextensibility conditions immediately gives over each segment L_i the equality $|r_s^h| = |\frac{r_{i+1}-r_i}{\Delta s}| = 1$, which ensures $(r_s^h)_h$ is bounded in $L^2(Q_T)$ norm. In the proof of Lemma 4.4.1, using the energy estimate (4.17), we previously obtained some bounds on the discrete quantities $\dot{r}_i$ in equation (4.29) and $\dot{\theta}_i$ in equation (4.26), independently of N. Using those bounds, we obtain the following result on $\|\dot{r}^h\|_2$

$$\begin{aligned}
\|\dot{r}^h\|^2_{L^2(Q_T)} &= \int_0^T \sum_{i=1}^{N} \int_{L_i} \left|\dot{r}_i + s\frac{\dot{r}_{i+1}-\dot{r}_i}{\Delta s}\right|^2 \mathrm{d}s\ \mathrm{d}t \\
&\le 2\int_0^T \sum_{i=1}^{N} \int_{L_i} |\dot{r}_i|^2\,\mathrm{d}s\ \mathrm{d}t + 2\int_0^T \sum_{i=1}^{N} \int_{L_i} s^2\frac{(\dot{r}_{i+1}-\dot{r}_i)^2}{\Delta s^2}\,\mathrm{d}s\ \mathrm{d}t \\
&\le 2\int_0^T \sum_{i=1}^{N} \Delta s\ |\dot{r}_i|^2\,\mathrm{d}s\ \mathrm{d}t + \frac{2}{3}\int_0^T \sum_{i=1}^{N} \Delta s^3\dot{\theta}_i^2\,\mathrm{d}s\ \mathrm{d}t\,, \qquad (4.32)
\end{aligned}$$

which is bounded uniformly in $h = \Delta s$ from (4.26) and (4.29).

Lastly, we write r^h as $r^h = \bar{r} + \delta r$, where $\bar{r}(t) = \dfrac{1}{L}\displaystyle\int_0^L r^h(t,s)\,\mathrm{d}s$ and $\delta r = r^h - \bar{r}$ variations around $\bar{r}$ and thus naturally of zero average. We will find some bounds on $(r^h)_h$ by bounding separately both terms. Indeed, as we only have a bound for the

derivatives of $(r^h)_h$ in time and space, and no boundary condition, finding a bound for $(r^h)_h$ is not immediate. Using Poincaré-Wirtinger inequality, along with the bound on $(r^h_s)_h$ from equation (4.32)

$$\|\delta r\|_2 = \|r^h - \bar{r}\|_2 \leq C\|r^h_s\|_2,$$

which is bounded uniformly in Δs, and where $C > 0$ is a constant.

Moreover, differentiating in time gives $\dot{r}^h = \dot{\bar{r}} + \dot{\delta r}$. As $\dot{\bar{r}}$ (average speed) and $\dot{\delta r}$ (small speed variation) are orthogonal to each other, $\|\dot{r}^h\|_2^2 = \|\dot{\bar{r}}\|_2^2 + \|\dot{\delta r}\|_2^2$. We already know that $\dot{r}$ is bounded in L^2, and both right-hand-side terms are positive, they are also bounded. As $\dot{\bar{r}}$ is the mean speed, it does not depend on $s \in [0, L]$, so one has $\int_0^L |\dot{\bar{r}}|^2 \,\mathrm{d}s = L|\dot{\bar{r}}|^2$. This last quantity is bounded at any time $t > 0$ by some $\bar{C} > 0$. For some $T > 0$ and $t \leq T$

$$|\bar{r}(t) - \bar{r}(0)| \leq \int_0^\intercal |\dot{\bar{r}}| \leq T^{1/2} \left(\int_0^\intercal |\dot{\bar{r}}|^2 \right)^{1/2} \leq \sqrt{\bar{C}} T.$$

Finally, since $\bar{r}(0) < \infty$, $\bar{r}$ is bounded in $[0, T]$ and so $(r^h)_h$ is bounded in $L^2(Q_T)$.

2. Bounding $(\dot{r}^h_s)_h$ in $L^2((0,T); H^{-1}(0,L))$. Since $(\dot{r}^h)_h$ is bounded in $L^2(Q_T)$, according to **1.**, $(\dot{r}^h_s)_h$ is also bounded in $L^2((0,T); H^{-1}(0,L))$, as for all $u \in L^2(0,L)$, $\|u_s\|_{H^{-1}(0,L)} \leq \|u\|_{L^2(0,L)}$.

3. Bounding $(r^h_s)_h$ in $L^2((0,T); BV(0,L))$. Let us compute $\|r^h_s(t,\,\cdot)\|_{BV}$, recalling that $e_{i,\parallel}(t) = \frac{r_{i+1}(t) - r_i(t)}{\Delta s}$, we obtain

$$\|r^h_s(t,\,\cdot)\|_{BV} = |r^h_s(t,0)| + TV(r^h_s(t,\,\cdot)) = |e_{1,\parallel}(t)| + \sum_{i=1}^{N-1} |e_{i+1,\parallel}(t) - e_{i,\parallel}(t)|. \tag{4.33}$$

Then, since $e_{i,\parallel} = (\cos(\theta_i), \sin(\theta_i))^\intercal$, we have that, also using Cauchy-Schwarz inequality

$$\|r^h_s(t,\,\cdot)\|_{BV} \leq 1 + \sum_{i=1}^{N-1} |\theta_{i+1}(t) - \theta_i(t)| \leq 1 + \sqrt{N-1} \left(\sum_{i=1}^{N-1} |\theta_{i+1}(t) - \theta_i(t)|^2 \right)^{1/2}. \tag{4.34}$$

Finally, from the energy estimate (4.25), we get that $\sum_{i=1}^{N-1} \Delta s \, \frac{|\theta_{i+1}(t) - \theta_i(t)|^2}{\Delta s^2}$ decreases over time and we deduce

$$\|r^h_s(t,\,\cdot)\|_{BV} \leq 1 + \sqrt{L} C, \tag{4.35}$$

where $C = \sum_{i=1}^{N-1} \Delta s \, \frac{|\theta_{i+1}(0) - \theta_i(0)|^2}{\Delta s^2}$, which is uniformly bounded in Δs by hypothesis. Integrating its square over time in $[0, T]$ concludes the proof.

4. Bounding $(n^h)_h$ in $L^2((0,T);H^1(0,L))$. First, we notice that

$$\begin{aligned}\|n_s^h(t,\cdot)\|_2^2 &= \sum_{i=1}^{N}\Delta s\left|\frac{n_{i+1}(t)-n_i(t)}{\Delta s}\right|^2\\ &= \sum_{i=1}^{N}\Delta s\left|\mathbf{C}(\theta_i)\dot{r}_{i+1/2}(t)\right|^2\end{aligned}$$

using the force balance in (4.8).

Summing over i, and integrating over $[0,T]$, we get

$$\|n_s^h\|^2_{L^2(Q_T)} = = \int_0^T\sum_{i=1}^{N}\Delta s\left|\mathbf{C}(\theta_i)\dot{r}_{i+1/2}(t)\right|^2\mathrm{d}t. \tag{4.36}$$

Using equations (4.2) and (4.27) gives that $(n_s^h)_h$ is bounded in $L^2(Q_T)$ uniformly in $h=\Delta s$. Finally, using the boundary condition $n^h(t,L)=0$, we deduce that $(n^h)_h$ is also bounded in $L^2((0,T);H^1(0,L))$.

5. Bounding $(m^h)_h$ in $L^2((0,T);H^1(0,L))$. As for n^h before, since, for all $t>0$, $m^h(t,L)=0$, it is sufficient to prove that $(m_s^h)_h$ is bounded in $L^2(Q_T)$. Let us write

$$\|m_s^h(t,\cdot)\|_2^2 = \sum_{i=1}^{N}\Delta s\left|\frac{m_{i+1}(t)-m_i(t)}{\Delta s}\right|^2. \tag{4.37}$$

Then, using the moment balance from the system of equations (4.8), we also have that

$$\left|\frac{m_{i+1}(t)-m_i(t)}{\Delta s}\right| \le \left|\frac{n_{i+1}(t)+n_i(t)}{2}\right| + \frac{\Delta s^2}{12}c_\perp|\dot{\theta}_i(t)|. \tag{4.38}$$

Combining equations (4.37) and (4.38) leads to

$$\|m_s^h(t,\cdot)\|_2^2 \le 2\sum_{i=1}^{N}\Delta s\left|\frac{n_{i+1}(t)+n_i(t)}{2}\right|^2 + 2\sum_{i=1}^{N}\Delta s\frac{\Delta s^4}{144}c_\perp^2|\dot{\theta}_i(t)|^2. \tag{4.39}$$

Moreover, one can notice that

$$\begin{aligned}\|n^h(t,\cdot)\|_2^2 &= \sum_{i=1}^{N}\int_{-\Delta s/2}^{\Delta s/2}\left|\frac{n_i(t)+n_{i+1}(t)}{2}+\frac{2s}{\Delta s}\frac{n_{i+1}(t)-n_i(t)}{2}\right|^2\mathrm{d}s\\ &\ge \sum_{i=1}^{N}\Delta s\left|\frac{n_i(t)+n_{i+1}(t)}{2}\right|^2.\end{aligned} \tag{4.40}$$

Using equation (4.40) into equation (4.39) and integrating over time then gives

$$\int_0^T \sum_{i=1}^N \Delta s \left| \frac{m_{i+1}(t) - m_i(t)}{\Delta s} \right|^2 \mathrm{d}t \leq 2 \int_0^T \|n^h(t,\,\cdot)\|_2^2 \,\mathrm{d}t + \int_0^T \frac{2\Delta s^2}{144} c_\perp^2 \sum_{i=1}^N \Delta s^3 |\dot{\theta}_i|^2 \,\mathrm{d}t, \quad (4.41)$$

which is bounded uniformly in Δs, since, from **4.**, $(n^h)_h$ is bounded in $L^2((0,T);H^1(0,L))$ and $\left(\int_0^T \sum_{i=1}^N \Delta s^3 |\dot{\theta}_i|^2 \,\mathrm{d}t \right)_h$ is bounded uniformly in $h = \Delta s$, according to equation (4.26).

6. Bounding $(\Delta s\, \dot{\bar{\theta}}^h)_h$ in $L^2(Q_T)$. Using the energy estimate from Lemma 4.3.1, integrating it over time and following the same reasoning as in the proof of Lemma 4.4.1, we obtain

$$\int_0^T \sum_{i=1}^N \int_{L_i} (\Delta s\, \dot{\bar{\theta}}^h(s))^2 \,\mathrm{d}s \;\mathrm{d}t = \int_0^T \sum_{i=1}^N \Delta s^3\, \dot{\theta}_i^2 \;\mathrm{d}t, \quad (4.42)$$

which is bounded uniformly in Δs. Finally, $(\Delta s\, \dot{\bar{\theta}}^h)_h$ is bounded in $L^2(Q_T)$.

7. Bounding $(\theta_s^h)_h$ in $L^2(Q_T)$.

First, let us write $\theta_s^h(s,t) = \sum_{i=1}^{N-1} \frac{\theta_{i+1}-\theta_i}{\Delta s} \mathbb{1}_{L_{i+1}}$. Using the integrated energy estimate (4.25), we get

$$\begin{aligned}
\|\theta_s^h\|_2^2 &= \int_0^T \sum_{i=1}^{N-1} \int_{L_{i+1}} \left| \frac{\theta_{i+1}(t) - \theta_i(t)}{\Delta s} \right|^2 \mathrm{d}s \;\mathrm{d}t \\
&= \int_0^T \sum_{i=1}^{N-1} \Delta s \left| \frac{\theta_{i+1}(t) - \theta_i(t)}{\Delta s} \right|^2 \mathrm{d}t \\
&\leq T \sum_{i=1}^{N-1} \Delta s \left| \frac{\theta_{i+1}(0) - \theta_i(0)}{\Delta s} \right|^2 \mathrm{d}t.
\end{aligned}$$

By hypothesis, $\left(\sum_{i=1}^{N-1} \frac{\theta_{i+1}(0)-\theta_i(0)}{h} \right)_h$ is uniformly bounded in $h = \Delta s$ in $L^2(Q_T)$, and then so is $(\theta_s^h)_h$. □

Using the bounds from Proposition 4.5.1 on the interpolates r^h, n^h, m^h and $\bar{\theta}^h$, the following proposition guarantees that, up to extraction of subsequences, all the aforementionned quantities converge towards a limit, each in their relevant spaces, as specified below.

PROPOSITION 4.5.2 · *Extraction of convergent subsequences*

Up to the extraction of a subsequence, and if $(\theta_s^h(0,\cdot))_h$ is bounded uniformly h in $L^2(0,L)$, the interpolates defined in equations (4.11-4.16) all converge, when $h = \Delta s \to 0$, in the following sense:

1. $(r^h)_h$ converges to r weakly in $H^1(Q_T)$ and strongly in $L^2(Q_T)$;
2. $(r_s^h)_h$ strongly to r_s in $L^2(0,T;L^p(0,L))$ for all $1 \leq p < \infty$;
3. $(n^h)_h$ weakly converges to n in $L^2((0,T);H^1(0,L))$;
4. $(m^h)_h$ weakly converges to m in $L^2((0,T);H^1(0,L))$;
5. $(\bar{m}^h)_h$ weakly converges to m in $L^2(0,T;L^p(0,L))$ for all $1 \leq p < \infty$;
6. $(\Delta s^2\,\dot{\bar{\theta}}^h)_h$ strongly converges to 0 in $L^2(Q_T)$;
7. $(\theta_s^h e_z)_h$ weakly converges to α in $L^2(Q_T)$.

Proof. **1. Convergence of $(r^h)_h$ in $H^1(Q_T)$ and in $L^2(Q_T)$.** From **1.** in Proposition 4.5.1, $(r^h)_h$ is bounded in $H^1(Q_T)$. Classically, there exists a subsequence of $(r^h)_h$ that converges to a limit r, weakly in $H^1(Q_T)$ and strongly in $L^2(Q_T)$, thanks to Rellich Theorem.

2. Convergence of $(r_s^h)_h$ in $L^2((0,T);L^p(0,L))$ for all $1 \leq p < \infty$. We know from Proposition 4.5.1, that $(\dot{r}_s^h)_h$ is bounded in $L^2((0,T);H^{-1}(0,L))$ and $(r_s^h)_h$ is bounded in $L^2((0,T);BV(0,L))$. Thanks to Lemmas 4.5.1 and 4.5.2, for any $1 \leq p < \infty$, we can deduce that $(r_s^h)_h$ is relatively compact in $L^2((0,T);L^p(0,L))$.

3. Convergence of $(n^h)_h$ in $L^2((0,T);H^1(0,L))$. From **4.** in Proposition 4.5.1, $(n^h)_h$ is bounded in $L^2((0,T);H^1(0,L))$ so, up to the extraction of a subsequence, it weakly converges towards a limit n in $L^2((0,T);H^1(0,L))$.

4. Convergence of $(m^h)_h$ in $L^2((0,T);H^1(0,L))$. It follows similarly from **5.** in Proposition 4.5.1.

5. Convergence of $(\bar{m}^h)_h$ in $L^2(Q_T)$. Let us prove that $(\bar{m}^h)_h$ weakly converges towards m in $L^2(Q_T)$, by computing the norm of the difference between $\bar{m}^h$ and m^h, as follows

$$\begin{aligned}\int_0^T \|\bar{m}^h(t) - m^h(t)\|_2^2 \,\mathrm{d}t &= \int_0^T \sum_{i=1}^N \int_0^{\Delta s} (m_i(t)(1 - s/\Delta s) + m_{i+1}(t)s/\Delta s - m_i(t))^2 \,\mathrm{d}s\,\mathrm{d}t \\ &= \int_0^T \sum_{i=1}^N \int_0^{\Delta s} 1/E^2 (m_i(t) - m_{i+1}(t))^2 (s/\Delta s)^2 \,\mathrm{d}s\,\mathrm{d}t \\ &\leq \frac{\Delta s}{3} \|m^h\|^2_{L^2((0,T);H^1(0,L))}.\end{aligned} \tag{4.43}$$

Since $\lim_{h=\Delta s \to 0} \Delta s \|m^h\|^2_{L^2((0,T);H^1(0,L))} = 0$ from **5.** in Proposition 4.5.1, this concludes the proof for $(\bar{m}^h)_h$.

6. Convergence of $(\Delta s^2\,\dot{\bar{\theta}}^h)_h$ in $L^2(Q_T)$. It follows from **6.** in Proposition 4.5.1.

7. Convergence of $(\theta_s^h e_z)_h$ in $L^2(Q_T)$. It follows from **7.** in Proposition 4.5.1.

Eventually, it is important to notice that the extractions of subsequences may be done in a row so we can assume that the abovementioned convergences are obtained for all sequences with the same indices $(h_n)_{n\in\mathbb{N}}$ with $h_n \to 0$ as $n \to +\infty$. □

In order to prove Theorem 4.2.2, it now remains to establish that the limits obtained in Proposition 4.5.2 are solutions of the continuous system (4.3). We will do so by first introducing a weak form of the system of equations (4.8), and passing to the limit as h (actually h_n) tends to 0. Let $\varphi \in C_c^\infty(0,L)$, and $\psi \in C_c^\infty(0,T)$, we notice that can rewrite the $N-$link equations (4.8) as

$$
\begin{cases}
\displaystyle\int_0^T\int_0^L \Big(\mathbf{C}(\bar{\theta}^h)\dot{r}^h(t,s) + n_s^h(t,s)\Big)\,\varphi(s)\psi(t)\,\mathrm{d}s\,\mathrm{d}t = 0, & \text{(4.44a)}\\[2ex]
\displaystyle\int_0^T\int_0^L \left(\left(-\frac{\Delta s^2}{12}c_\perp\dot{\bar{\theta}}^h(t,s)e_z + m_s^h(t,s)\right)\varphi(s) + \Big(r_s^h(t,s)\times n^h(t,s)\bar{\varphi}^h(s)\Big)\right)\psi(t)\,\mathrm{d}s\,\mathrm{d}t = 0, & \text{(4.44b)}\\[2ex]
\displaystyle\int_0^T\int_0^L \bar{m}^h(t,s)\varphi(s)\psi(t)\,\mathrm{d}s\,\mathrm{d}t = \int_0^T\int_0^L E\theta_s^h(t,s)e_z\varphi(s)\psi(t)\,\mathrm{d}s\,\mathrm{d}t, & \text{(4.44c)}\\[2ex]
\Big|r_s^h(t,s)\Big| = 1, \text{ for a.e. } (t,s)\in Q_T, & \text{(4.44d)}\\[2ex]
n^h(t,0) = 0, \text{ for a.e. } t\in[0,T], & \text{(4.44e)}\\[2ex]
m^h(t,0) = \bar{m}^h(t,0) = 0, \text{ for a.e. } t\in[0,T], & \text{(4.44f)}
\end{cases}
$$

where $\bar{\varphi}^h$ is defined by, for $s \in [0,L]$

$$
\bar{\varphi}^h(s) = \sum_{i=1}^N \frac{1}{\Delta s}\left(\int_{L_i}\varphi(u)\,\mathrm{d}u\right)\mathbb{1}_{L_i}(s). \tag{4.45}
$$

The next proposition then shows that the solutions of the system of equations (4.44) converge towards the solutions of a weak form of equations (4.3) when Δs goes to zero.

PROPOSITION 4.5.3 · *Equations verified by the limits of the interpolates*

Assume $(\theta_s^h(0,\cdot))_h$ is bounded uniformly h in $L^2(0,L)$. Then, the limits $(r,\, n,\, m) \in H^1(Q_T) \times L^2((0,T);H^1(0,L))^2$, introduced in Proposition 4.5.2, of the interpolates defined in equations (4.11-4.16) satisfy the following system of equations, for $\varphi \in C_c^\infty(0,L)$ and $\psi \in C_c^\infty(0,T)$

$$
\begin{cases}
\displaystyle\int_0^T\int_0^L \left(\mathbf{C}(\theta)\dot{r}(t,s) + n_s(t,s)\right)\varphi(s)\psi(t)\,\mathrm{d}s\,\mathrm{d}t = 0, & \text{(4.46a)}\\[2ex]
\displaystyle\int_0^T\int_0^L \left(m_s(t,s) + r_s(t,s)\times n(t,s)\right)\varphi(s)\psi(t)\,\mathrm{d}s\,\mathrm{d}t = 0, & \text{(4.46b)}\\[2ex]
\displaystyle\int_0^T\int_0^L m(t,s)\varphi(s)\psi(t)\,\mathrm{d}s\,\mathrm{d}t = \int_0^T\int_0^L Er_{ss}(t,s)\times r_s(t,s)\varphi(s)\psi(t)\,\mathrm{d}s\,\mathrm{d}t, & \text{(4.46c)}\\[2ex]
|r_s(t,s)| = 1, \text{ for a.e. } (t,s)\in Q_T, & \text{(4.46d)}\\[2ex]
n(t,0) = 0, \text{ for a.e. } t\in[0,T], & \text{(4.46e)}\\[2ex]
m(t,0) = 0, \text{ for a.e. } t\in[0,T]. & \text{(4.46f)}
\end{cases}
$$

Proof. **Force balance.** First of all, notice that

$$\mathbf{C}(\bar{\theta}^h) = -\left(c_\parallel r_s^h\left(r_s^h\right)^\intercal + c_\perp\left(I - r_s^h\left(r_s^h\right)^\intercal\right)\right).$$

and since $(r_s^h)_h$ strongly converges to r_s in $L^2(0,T;L^4(0,L))$, according to Proposition 4.5.2, we deduce that $\mathbf{C}(\bar{\theta}^h)$ strongly converges in $L^2(Q_T)$ to

$$\mathbf{C}(\theta) = -\left(c_\parallel r_s\left(r_s\right)^\intercal + c_\perp\left(I - r_s\left(r_s\right)^\intercal\right)\right).$$

Moreover, Proposition 4.5.2 also states that $(\dot{r}^h)_h$ weakly converges towards $\dot{r}$ in $L^2(Q_T)$, and $(n_s^h)_h$ weakly converges towards n_s in $L^2(Q_T)$. This is sufficient to pass to the limit in equation (4.44a) and obtain (4.46a).

Moment balance. From **6.** in Proposition 4.5.2, we have that $\Delta s^2\dot{\bar{\theta}}^h$ strongly converges towards zero when $\Delta s \to 0$, in $L^2(Q_T)$. Then, from **4.** in Proposition 4.5.2, m_s^h also

weakly converges to m_s in $L^2(Q_T)$. Let us then express the rightmost term in (4.44b) with $\bar{\varphi}^h$ in terms of φ as

$$\int_0^T\int_0^L (r_s^h(s)\times n^h(s))\bar{\varphi}^h(s)\,\mathrm{d}s\,\psi(t)\,\mathrm{d}t = \sum_{i=1}^N \int_0^T\int_{L_i} (r_s^h(s)\times n^h(s))\varphi(s)\,\mathrm{d}s\,\psi(t)\,\mathrm{d}t + \sum_{i=1}^N \int_0^T\int_{L_i} (r_s^h(s)\times n^h(s))(\bar{\varphi}^h(s)-\varphi(s))\,\mathrm{d}s\,\psi(t)\,\mathrm{d}t\,. \tag{4.47}$$

We now want to go to the limit in both terms on the right-hand side. Looking at the first one, we know from **2.** and **3.** in Proposition 4.5.2 that r_s^h strongly converges towards r_s in $L^2(Q_T)$ and n^h weakly converges towards n in $L^2(Q_T)$. This leads to

$$\lim_{h=\Delta s\to 0}\int_0^T\int_0^L (r_s^h(s)\times n^h(s))\varphi(s)\,\mathrm{d}s\,\psi(t)\,\mathrm{d}t = \int_0^T\int_0^L (r_s(s)\times n(s))\varphi(s)\psi(t)\,\mathrm{d}s\,\mathrm{d}t. \tag{4.48}$$

For the second term, using (4.45) and Poincaré-Wirtinger inequality on each segment L_i, we have, on the whole filament and for some constant $C>0$ independent of Δs,

$$\|\varphi-\bar{\varphi}^h\|_{L^2(0,L)} \le C\Delta s\|\varphi_s\|_{L^2(0,L)}. \tag{4.49}$$

Combining (4.47) and (4.49), with (4.44d), it comes, for a constant $\tilde{C}>0$

$$\sum_{i=1}^N \int_0^T\int_{L_i} (r_s^h(s)\times n^h(s))(\bar{\varphi}^h(s)-\varphi(s))\psi(t)\,\mathrm{d}s\,\mathrm{d}t \le \tilde{C}\Delta s\|n^h\|_{L^2(Q_T)}\|\varphi_s\|_{L^2(0,L)}\|\psi\|_{L^2(0,T)}.$$

Since, from **4.** in Proposition 4.5.1, n^h is bounded independently of Δs in $L^2(Q_T)$, the right-hand side converges to zero when $\Delta s\to 0$. In conclusion, the limits $(r,\,n,\,m)\in H^1(Q_T)\times L^2((0,T);H^1(0,L))^2$ satisfy (4.46b).

Inextensibility constraint. The limit $r_s\in L^2((0,T);L^4(0,L))$ of r_s^h automatically verifies the inextensibility constraint (4.46d), according to **2.** in Proposition 4.5.2.

Boundary conditions. We notice that both $(n^h)_h$ and $(m^h)_h$ are in $L^2((0,T);H_0^1(0,L))$ which is closed with respect to the weak $L^2((0,T);H^1(0,L))$ convergence. Therefore the weak limits n and m satisfy the boundary conditions (4.46e) and (4.46f).

Relation between m and θ. First, we have from Proposition 4.5.2 that $(\bar{m}^h)_h$ weakly converges towards m, and that $(\theta_s^h)_h$ weakly converges towards α, both in $L^2(Q_T)$. Then,

we would like to identify α to the curvature in the continuous system recalling that, in System (4.3), m is also characterized by $m = Er_{ss} \times r_s$. To do so, we define

$$\hat{r}^h(t,s) = r^h(t,0) + \int_0^s (\cos\theta^h(t,u),\, \sin\theta^h(t,u))^\intercal \,\mathrm{d}u, \tag{4.50}$$

such that $\hat{r}^h_s = (\cos\theta^h, \sin\theta^h)^\intercal$. As θ^h is continuous and piecewise linear, this last expression is differentiable in s and we have

$$\hat{r}^h_{ss} = \theta^h_s(-\sin\theta^h,\, \cos\theta^h)^\intercal, \tag{4.51}$$

and

$$\bar{m}^h = E\theta^h_s e_z = E\hat{r}^h_{ss} \times \hat{r}^h_s. \tag{4.52}$$

Using Proposition 4.2.2, we know that $(\theta^h_s)_h$ weakly converges towards an $\alpha \in L^2(Q_T)$. We now want to identify α with a product of derivatives of r in s, provided they are well-defined. Looking at the left hand-side of equation (4.52), we have, similarly to the computation from equation (4.43)

$$\begin{aligned}
\|\bar{\theta}^h - \theta^h\|^2_{L^2(Q_T)} &= \int_0^T \sum_{i=2}^N \int_0^{\Delta s} (\theta_i - \theta_{i-1})^2 \left(1 - \frac{s}{\Delta s}\right)^2 \mathrm{d}s\,\mathrm{d}t \\
&= \int_0^T \sum_{i=2}^N \frac{\Delta s^3}{3E^2} m^2_{i+1}\,\mathrm{d}t \\
&\leq \frac{\Delta s^2}{3E^2} \|\bar{m}^h\|^2_{L^2(Q_T)}.
\end{aligned}$$

From Proposition 4.5.1, $(\bar{m}_h)_h$ is uniformly bounded in $L^2(Q_T)$, hence $\|\bar{\theta}^h - \theta^h\|_{L^2(Q_T)}$ goes to zero when $h \to 0$. Then, this also means that

$$\lim_{h\to 0} \|\hat{r}^h_s - r^h_s\|_{L^2(Q_T)} = \lim_{h\to 0} \|(\cos\theta^h, \sin\theta^h)^\intercal - (\cos\bar{\theta}^h, \sin\bar{\theta}^h)^\intercal\|_{L^2(Q_T)} = 0. \tag{4.53}$$

Since, from Proposition 4.5.2, $(r^h_s)_h$ strongly converges towards r_s in $L^2(Q_T)$, we also have that $(\hat{r}^h_s)_h$ strongly converges towards r_s in $L^2(Q_T)$. Using Proposition 4.5.1, $(\theta^h_s)_s$ is uniformly bounded in $h = \Delta s$ in $L^2(Q_T)$, from which we get that $(\hat{r}^h_{ss})_h$ is uniformly bounded in h in $L^2(Q_T)$ as well, so it weakly converges towards a limit (up to extraction of a subsequence). Remembering that $\hat{r}^h_s \in L^2((0,T); H^1(0,L))$ converges towards r_s in $L^2(Q_T)$, by uniqueness of the limit, r_s is differentiable in s and $\hat{r}^h_{ss}$ weakly converges towards r_{ss} in $L^2(Q_T)$. Finally, combining the weak convergence of $\hat{r}^h_{ss}$ and the strong convergence or $\hat{r}^h_s$ in $L^2(Q_T)$, we get

$$\lim_{h\to 0} \int_0^T \int_0^L \hat{r}^h_{ss}(t,s) \times \hat{r}^h_s(t,s)\varphi(s)\psi(t)\,\mathrm{d}s\,\mathrm{d}t = \int_0^T \int_0^L r_{ss}(t,s) \times r_s(t,s)\varphi(s)\psi(t)\,\mathrm{d}s\,\mathrm{d}t. \tag{4.54}$$

In conclusion, r_{ss} is well defined and m, r satisfy equation (4.46f). □

Notice that Propositions 4.5.1, 4.5.2 and 4.5.3 use no assumptions on boundary conditions in $s = 0$. They are all thus valid for either a *free*, *pinned* or *clamped* filament. This concludes the proof of Theorem 4.2.2.

4.6 *Discussion*

In this paper, we have addressed mathematical validity of the N-link formulation for the elastohydrodynamics of a filament in a viscous flow. Theorems 4.2.1 and 4.2.2 provide a rigorous proof of convergence (up to extraction) of the N-link model (4.8) towards the classical filament elastohydrodynamics formulation (4.3), which is a first step towards showing that the N-link swimmer is a well-founded discretization of a continuous elastohydrodynamic filament.

The proofs of both theorems rely on energy dissipation formula (4.17). The fact that this formula holds and precisely leads to convergence underlines, in particular, the superiority of the N-link model over other possible discretized versions of equation (4.3), such as a finite difference scheme on the filament arclength. As an important consequence, when numerically implementing the filament dynamics, Theorem 4.2.2 fully justifies the use of an N-link filament as an equivalent system.

Several extensions to the framework of the present study can be envisioned. We discuss the most prominent of them in the following and provide insights on the difficulties they would likely raise, leaving fuller analysis to future works.

Hydrodynamics. It is worth recalling that the elastohydrodynamics equation (4.3) as well as the N-link model (4.8) are built on coarse approximations of hydrodynamic interactions, namely local resistive force theory. Inclusion of nonlocal effects in the elastohydrodynamics equation is of course challenging from the functional analysis point of view, as it requires to deal with integral terms in the equation.

On the other hand, the N-link model can handle the inclusion nonlocal terms within the hydrodynamic matrix [103], and establishing invertibility of the resistance matrix to extend the results of Theorem 4.2.1 may still be tractable.

Non-Newtonian fluids also constitute and important avenue of research for future extensions of this study, with many biological fluids exhibiting viscoelastic behaviors or complex rheologies [93]. Well-posedness for continuous elastohydrodynamics featuring an additional coupling modeling linear viscoelasticity was tackled by Ohm in [79], whilst rigorous treatment of corresponding coarse-grained versions remains an open problem.

Active filament. Modeling internal activity within the curvature dynamics of the filament is a crucial step to fully describe the dynamics of biological filaments such as microswimmer flagella and cilia, rather than that of a passive elastic fiber for the present study. Activity is typically represented as an internal torque forcing, say τ, which would appear in the moment equation (fifth line of System (4.3)). By perturbative arguments, it is very likely that well-posedness and convergence are preserved in the case of "small

enough" τ, following the proofs of Theorems 4.2.1 and 4.2.2 and including suitable assumptions on the norm and regularity of τ. The general case for arbitrary τ is trickier, and probably does not admit more than local existence in time, as noted by Mori & Ohm for continous elastohydrodynamics [76].

Three-dimensional motion. As we can observe in many filaments, flagella in sperm cells or bacteria [22], [109], it is essential to then extend our well-posedness and convergence results to an analogous model in 3D. A possible extension could be envisioned by formally studying either a bead-and-segment model introduced by Fuchter and Bloomfield-Gadêlha [40], or the direct 3D equivalent of the N-link model, as presented by Walker, Ishimoto and Gaffney in [103]. For the latter, both the continuous equations and their discretization seem very similar to those of the N-link, except for the angles between segments which is now characterized by a three-dimensional twist vector. This then modifies the constitutive equation for the contact torque. However, the final matrix-vector system has a similar structure to that of the N-link, so similar mathematical methods may be of use.

Multiple filaments. In nature, for example when looking at swimming bacteria, multiple filaments are often present in the studied setting. As pointed out by Du Roure *et al.* [36] and Young [110], in this case, hydrodynamical interactions between filaments need to be taken into account, thus adding another layer of complexity to the problem. In particular, these interactions are deemed to have an important impact on swimming speed and filament motion in general.

In conclusion, we have shown the validity of the N-link model as a mathematically rigorous coarse-grained version of an elastic filament. This original approach bridging two physically relevant models could inspire future contributions to a more complete mathematical theory of microswimming and fluid-structure interaction at microscopic scale.

Se mia nonna avesse le ruote, sarebbe una carriola.

Italian expression

5 *Mathematical models for flagellar activation mechanisms*

In this chapter, Sections 5.1 through 5.7 reproduce a submitted paper [1], written in collaboration with François Alouges, Irene Anello, Antonio DeSimone and Aline Lefebvre-Lepot. The last section, 5.8.2, presents some additional unpublished results on a comparision between the usual assumptions used in our models and some equaitons arising from the system's chemistry.

5.1 *Introduction*

Cilia and flagella are active appendages-like organelles employed by numerous eukaryotic cells to swim inside viscous fluid [102]. They exploit hydrodynamic friction to induce cellular self-propulsion, and show a characteristic periodic motion in their dynamics [42], [43], which enables them to swim as efficiently as possible at a low Reynolds number [87].

However, as first noticed by Taylor [98] and Grey and Hancock [46], initiating a movement at the beginning of an elastic rod, in a setting similar to flagellar swimming, is not sufficient to propagate a wave along the appendage and match the type of periodic motion that is observed in practice. Machin [73] then observed that some form of internal activity is necessary to sustain the oscillations. The first numerical simulations with

active components were then conducted by Brokaw [26]–[28], by matching parameters values in order to reproduce a flagellum's beating pattern [85].

We now know that all cilia and flagella have a common internal structure, their cytoskeleton called the axoneme, which is composed of pairs of A and B filaments, called microtubules. An axoneme is composed of nine microtubule pairs arranged in a cylinder and, in some cases, a central tubule pair. All filaments have a periodic structure and are polar with the same polarity, their minus end being attached to the basal corpuscle, a complex structure linking the filament to the swimmer's body. Interconnection proteins then link tubules together; nexin forms elastic links between two adjacent microtubule doublets, while radial spokes go from tubules A towards the center.

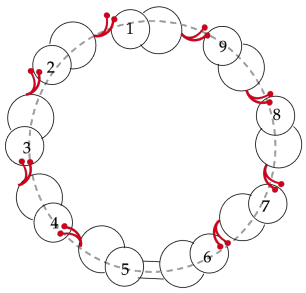

Figure 5.1. Simplified axoneme with 9 microtubule doublets and no central pair [108]. Note the presence of a bridge between rows 5 and 6.

This is indeed an active structure due to the work done by molecular motors, which are protein macro-molecules that move along periodic and polar filaments. In the axoneme, molecular motors are called dyneins and are situated between neighbouring microtubule pairs. They are attached to one of the microtubule pair and walk along the opposite pair creating local sliding between neighbouring microtubules, similarly to what can be observed in muscles with the sliding filament model [94]. This structure directly creates bending along the filament [96].

This complex three dimensional structure has first been modeled in [29] as a pair of filaments that bends on a plane; throughout this paper we will call this model the one-row model. This kind of projection of the axoneme, well represented in [89], implies a great simplification on the study of the hydrodynamics of the system, while still detecting the typical oscillatory behaviour of cilia and flagella. This was made possible by coupling the dynamics of active filaments together with the stochastic equations that regulates the molecular activity of the dyneins. Our focus is going to be on this last part, suggesting a new filament structure and adding motors rows using the stochastic model presented in [54]–[58], [62] and [86], where motors are attached to one of the two filaments of the projection, and walk on the other one. This model has no additional components regulating sliding, and nevertheless prove that dyneins can synchronize and thus auto-regulate themselves to create a form of alternating sliding on both sides of the axoneme. This matches, in particular, with the curvature regulation hypothesis called steady dynein loading [19], [52], [107] in which axonemal curvature is created

without any inhibition mechanism transmitted along the system. Note that this question is controversial as many other curvature regulation models, using additional mechanical signaling to provide some form of inhibition have been proposed in the literature [50], [65]–[71].

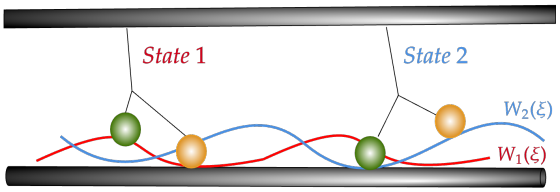

Figure 5.2. Two states of a motor walking along a microtubule in a periodicity cell.

Let us focus on one dynein: its motion can be described with a stochastic two-state model. The idea is that the motor can be found only either in state 1, where one head is bound to the filament and the other is not, or in state 2, where the opposite configuration holds (see Fig. 5.2). Each state $i = 1, 2$ is defined by its potential energy $W_i(\xi)$ at position $\xi \in [0, \ell]$ on the filament, as shown in Figure 5.2. The necessary energy for the motor to change its state is provided by a hydrolysis transformation involving Adenosinetriphosphate (ATP).

We introduce two transition rates, $\omega_1(\xi)$ and $\omega_2(\xi)$, that measure the probability per unit of time for one motor to go from state 1 to state 2 and vice versa. The transition rates depend on W_i as well as on the chemical quantities. One way to model this last dependence is to define the local deviation from the chemical equilibrium of the system as a non negative quantity, Ω, which is proportional to the ATP concentration. A full treatment of this is present in [55]. When Ω is zero, the system does not have energy to consume, it is in chemical equilibrium and the molecular motors remain still.

The filaments have periodic structures, and it is common to assume that both potentials W_1 and W_2, and transition rates ω_1 and ω_2 are periodic functions with the same period ℓ. In practice, we use explicit expressions for them.

Microtubules are therefore linked together by a large number of molecular motors obeying the two-state model. In the limit of an infinite system, one can then introduce densities $P^i(\xi) \geq 0$ with $i = 1, 2$ which give the probability to find a motor at position ξ in state i, as suggested in [57], [105]. These densities are not independent but obey $P^1(\xi) + P^2(\xi) = 1/l$, reflecting the fact that a motor is always either in state 1 or in state 2. The moving filament is at position $x(t)$, with velocity $v(t) = \frac{d}{dt}x(t)$, given by the collective work of all motors attached to it. The one-row model, given in [56], expresses this motion as a transport equation on $P = P^1$, namely:

$$\begin{cases} \partial_t P(\xi,t) + v(t)\partial_\xi P(\xi,t) = -(\omega_1+\omega_2)P(\xi,t) + \omega_2/\ell \\ v(t) = \dfrac{1}{\eta}\left(\displaystyle\int_0^\ell d\xi P(\xi,t)\partial_\xi \Delta W(\xi) - kx(t)\right), \end{cases} \tag{5.1}$$

where $\omega_i = \omega_i(\xi;\Omega)$ and $\Delta W(\xi) = W_2(\xi) - W_1(\xi)$.

This system has a non moving and stationary solution:

$$P_{eq}(\xi;\Omega) = \frac{\omega_2}{\ell(\omega_1+\omega_2)}, \quad v_{eq} = 0, \quad x_{eq} = \frac{1}{k}\int_0^l d\xi\, P_{eq}(\xi;\Omega)\partial_\xi \Delta W(\xi).$$

Depending on the chosen expressions for transitions rates ω_i and potentials W_i, a threshold value $\Omega = \Omega_0$ may exist, above which this solution becomes unstable and oscillates.

Notice that, in the one-row model, even without any external force, there is a non-zero equilibrium displacement x_{eq} leading to a bending of the tail at rest. Jülicher and Camalet mentioned this issue in [29], solving it by choosing symmetrical potentials and transition rates when modeling chemistry. Instead, in this work, we keep the chemistry in its general formulation and introduce a second row of molecular motors, as in Figure 5.3(a), 5.3(b). The two-row model is a simplified version of the axoneme, which forms a cylinder with only two microtubule pairs linked by two motor rows, as shown in Figure 5.3(a). This simplification acts like Sartori's two-dimensional projection of the axoneme [89], and enables the simplified axoneme to create a curvature in both directions, as motors on opposite sides of the axoneme generate bends in opposite directions [91].

This *two-row model* is also a first step to the real model, which we study via an N-row model in section 5.4 (where N corresponds here to the quantity of motor rows), as shown in Figure 5.1.

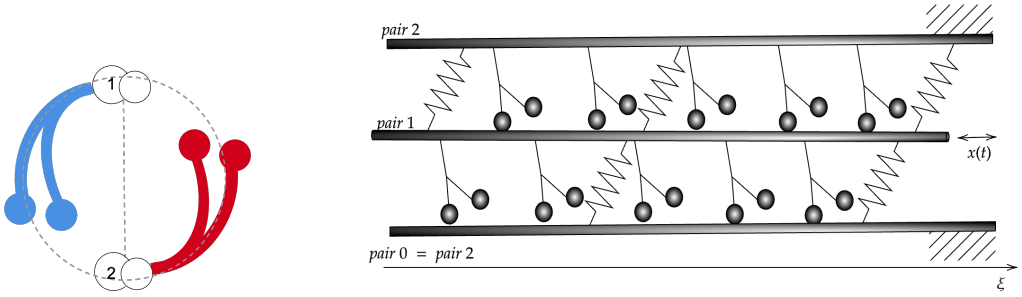

(a) **(b)**

Figure 5.3. (a) Cross section of the partial axoneme with two opposite microtubule pairs. (b) Side view of the partial axoneme with two opposite microtubule pairs.

As one can see in Figure 5.3(b), we call $x(t)$ the relative displacement of the tubule pairs. Following the same principles as for the one row of molecular motors, we introduce P_i as the probability that a motor attached to tubule pair i is in state 1.

Let $P(\xi,t) = P_1(\xi,t)$ and $Q(\xi,t) = P_2(\xi + x(t),t)$. Then, we obtain (see section 5.3) the following system of equations, for $\xi \in [0,\ell]$ and $t > 0$:

$$\begin{cases} \dfrac{\partial P}{\partial t}(\xi,t) + v(t)\dfrac{\partial P}{\partial \xi}(\xi,t) = -(\omega_1(\xi;\Omega)+\omega_2(\xi;\Omega))P(\xi,t) + \dfrac{\omega_2(\xi;\Omega)}{\ell}, \\ \dfrac{\partial Q}{\partial t}(\xi,t) - v(t)\dfrac{\partial Q}{\partial \xi}(\xi,t) = -(\omega_1(\xi;\Omega)+\omega_2(\xi;\Omega))Q(\xi,t) + \dfrac{\omega_2(\xi;\Omega)}{\ell}, \\ v(t) = \dfrac{1}{2\eta}\left(\displaystyle\int_0^\ell (P(\xi,t)-Q(\xi,t))\partial_\xi \Delta W(\xi)d\xi - 2kx(t)\right), \\ P(0,t) = P(\ell,t), \quad Q(0,t) = Q(\ell,t), \end{cases} \tag{5.2}$$

with ℓ-periodic ω_i and ΔW.

The goal of this paper is twofold. On the one hand, we rigorously prove an existence and uniqueness result for the solution of (5.2). Furthermore, we show the existence of a Hopf bifurcation for that same system when reasonable formulas are taken for potentials W_i and transition rates ω_i, depending on the ATP concentration via Ω.

On the other hand, we provide the reader with numerical simulations of (5.2). An upwind scheme is considered to handle both transport equations. Theoretical results are illustrated numerically, and simulations with more general potentials are also given. Moreover, the numerical method extends to the more realistic N-row model described in Figure 5.1.

Before stating the theoretical results, we point out thata we assume (see [29], [47]),

$$\omega_1(\xi;\Omega) + \omega_2(\xi;\Omega) = a_0(\Omega), \tag{5.3}$$

where $a_0(\Omega) > 0$. The first theorem reads as follows:

THEOREM 5.1.1 · *Existence and uniqueness*

Let us fix $\ell > 0$. Assume $\omega_1(\xi;\Omega)$ and $\omega_2(\xi;\Omega)$ as in (5.3). Moreover, assume ω_2 and ΔW to be at least $C^1([0,\ell])$. If the initial data $P(\xi,0)$ and $Q(\xi,0)$ are $C^1([0,\ell])$ and $x(0) = 0$, then the system of equations (5.2), admits a unique solution P, $Q \in C^1([0,\ell]\times\mathbb{R}_+)$ and $x \in C^1(\mathbb{R}_+)$.

For the second result we define $\Delta W(\xi) = U\cos\left(\dfrac{2\pi\xi}{\ell}\right)$, as in [29]. Moreover, since the two motor heads are identical, then $\omega_2(\xi) = \omega_1(\xi+\ell/2)$. Taking the transition rates' periodicity into account, we use the following Fourier expansion

$$\omega_2(\xi;\Omega) = \frac{a_0(\Omega)}{2} + \sum_{n=2k+1,\, k\geq 0} \left(a_n(\Omega)\cos\frac{2n\pi\xi}{\ell} + b_n(\Omega)\sin\frac{2n\pi\xi}{\ell}\right), \tag{5.4}$$

with $a_n(\Omega)$ and $b_n(\Omega)$ real coefficients.

THEOREM 5.1.2 · *Hopf bifurcation*

In addition to the hypothesis above, assume that $a_0(\Omega) = a_0^0\Omega^{\alpha_0}$, $a_1(\Omega) = a_1^0\Omega^{\alpha_1}$, $b_1(\Omega) = a_1^0\Omega^{\alpha_1}$ for $a_1^0 \in \mathbb{R}$ and $\alpha_0, \alpha_1, a_0^0, \Omega \in \mathbb{R}_+$. Furthermore, let us define

$$\tau(\Omega) := -\frac{1}{4}(2a_0^0\Omega^{\alpha_0} + \frac{\zeta\ell}{\pi} + 2\lambda\frac{a_1^0}{a_0^0\ell}\Omega^{\alpha_1-\alpha_0}), \tag{5.5}$$

with $\zeta = 2\pi k/\eta\ell$ and $\lambda = 2\pi^2 U/\eta\ell$. Suppose there exists $\Omega_0 \in \mathbb{R}_+$ such that $\tau(\Omega_0) = 0$ and $\tau'(\Omega_0) > 0$, then the solutions $P(\xi, t; \Omega)$, $Q(\xi, t; \Omega)$ and $x(t; \Omega)$ of the system (5.2) show a super-critical Hopf bifurcation in time near the bifurcation value Ω_0 and near the fixed point

$$(P_{eq}(\xi;\Omega), Q_{eq}(\xi;\Omega), x_{eq}(\Omega)) = \left(\frac{\omega_2(\xi;\Omega)}{a_0(\Omega)l}, \frac{\omega_2(\xi;\Omega)}{a_0(\Omega)l}, 0\right).$$

In particular, the fixed point is asymptotically stable for $\Omega < \Omega_0$, and unstable for $\Omega > \Omega_0$. Moreover there exists an asymptotically stable periodic orbit for $\Omega > \Omega_0$ with radius

$$\rho = \sqrt{-\frac{(\Omega - \Omega_0)\tau'(\Omega_0)}{\tilde{\tau}}} + o\left(\sqrt{\Omega - \Omega_0}\right), \tag{5.6}$$

where $\tilde{\tau} = -\dfrac{3\pi\zeta}{4\ell}\left(\dfrac{\pi a_0^0\Omega_0^{\alpha_0} + \ell\zeta}{\pi a_0^0\Omega_0^{\alpha_0} + 2\ell\zeta}\right)$.

The methods introduced to prove the theorems can be also used to demonstrate similar results for the one-row model, and might prove useful to consider the general N-row structure.

The paper is organized as follows. In the first section we give a brief overview on the one-row model, describing the chemistry and outlining the main properties of the model. We are going to do so through numerical simulations achieved by an upwind numerical scheme, also explained in this section. The second section is entirely dedicated to the two-row model, where we prove theorems 5.1.1, 5.1.2 and perform numerical simulations to confirm the theoretical results. In the third and last section, we open new questions by extending our model to the N-row structure.

5.2 *Numerical simulations of the one-row model*

In this section, we describe the numerical scheme used throughout the whole paper. It is used here to compute the solution to the one-row model (5.1) but can easily be extended to N-row models, for $N > 1$. We also show that well-known results for the 1-row model are recovered using our numerical scheme.

5.2.1 *Numerical method*

For numerical simulations of the whole 1-row PDE system (5.1), we write a first-order upwind scheme for the density P where, after each step, we update the velocity v. Let us take Δx such that $\ell = J\Delta x$ for $J \in \mathbb{N}^*$, and Δt the time step. We define $P_j^n := P(j\Delta x, n\Delta t)$, for $n \geq 1$ and $1 \leq j \leq J$. Being ℓ-periodic, we may extend P_j^n for all $j \in \mathbb{Z}$ by setting $P_{j+J}^n = P_j^n$ for all $j \in \mathbb{Z}$ and all $n \in \mathbb{N}$. At a fixed time step $t = n\Delta t$, $n \geq 1$, the velocity v^n of the central tubule pair being known, we compute, for $j \in \mathbb{Z}$

$$\begin{cases} S_j^n = -a_0 P_j^n + \omega_2(j\Delta x)/\ell, \\ P_j^{n+1} = \left(1 - v^n \dfrac{\Delta t}{\Delta x}\right) + v^n \dfrac{\Delta t}{\Delta x} P_{j-1}^n + \Delta t S_j^n \quad \text{if } v^n > 0, \\ P_j^{n+1} = \left(1 + v^n \dfrac{\Delta t}{\Delta x}\right) - v^n \dfrac{\Delta t}{\Delta x} P_{j+1}^n + \Delta t S_j^n \quad \text{if } v^n < 0. \end{cases} \tag{5.7}$$

and $(x^{n+1},\, v^{n+1})$ are

$$\begin{cases} \eta v^{n+1} = \Delta x \sum\limits_{j=1}^{J} \left(P_j^{n+1} \partial_\xi \Delta W(j\Delta x) \right) - k x^n, \\ x^{n+1} = x^n + v^{n+1} \Delta t. \end{cases} \tag{5.8}$$

Notice that, in (5.7), only one of the two updates is used for all j. Moreover, due to the stability of the upwind scheme, we need to check at each iteration that $\left| v^n \dfrac{\Delta t}{\Delta x} \right| < 1$.

5.2.2 *Numerical results*

All simulations are carried out defining the model functions that satisfy the hypotheses from theorem 5.1.2: $\Delta W(\xi) = U\cos(2\pi\xi/\ell)$, $a_0(\Omega) = a_0^0\sqrt{\Omega}$, $a_1(\Omega) = b_1(\Omega) = a_1^0\Omega$ and $a_n(\Omega) = b_n(\Omega) = 0$, if $n > 1$, with $\alpha_0 = 1/2$ and $\alpha_1 = 1$. All parameters values used for all simulations (unless specified otherwise) are shown in Table 5.1, matching F. Jülicher's [29]. We have taken for k_BT the value at $36°C$ (human body temperature). We compute a_1^0 such that the threshold of value of the system remains Ω_0, which is given. These choices will be justified in section 5.3.

Table 5.1. Values of the parameters used in numerical simulations.

Parameter	Value
ℓ	$10\,nm$
k_BT	$4.2668 \cdot 10^{-3}\,nN \cdot nm$
η	$1.0 \cdot 10^{-7}\,kg/s$
k	$9.5 \cdot 10^{-5}\,kg/s^2$
U	$10k_BT$
a_0^0	$1.0 \cdot 10^{3}\,s^{-1}$
Ω_0	$15k_BT$

As written above, in [29], the transition rates were taken symmetric to reflect the symmetry of the three dimensional body. Namely, ω_is are symmetric in the sense of [29] if $|\omega_i(\xi + l/2)| = |\omega_i(-\xi + l/2)|$. To point out what happens if the system is not symmetric we choose $b_1 \neq 0$, as in [47].

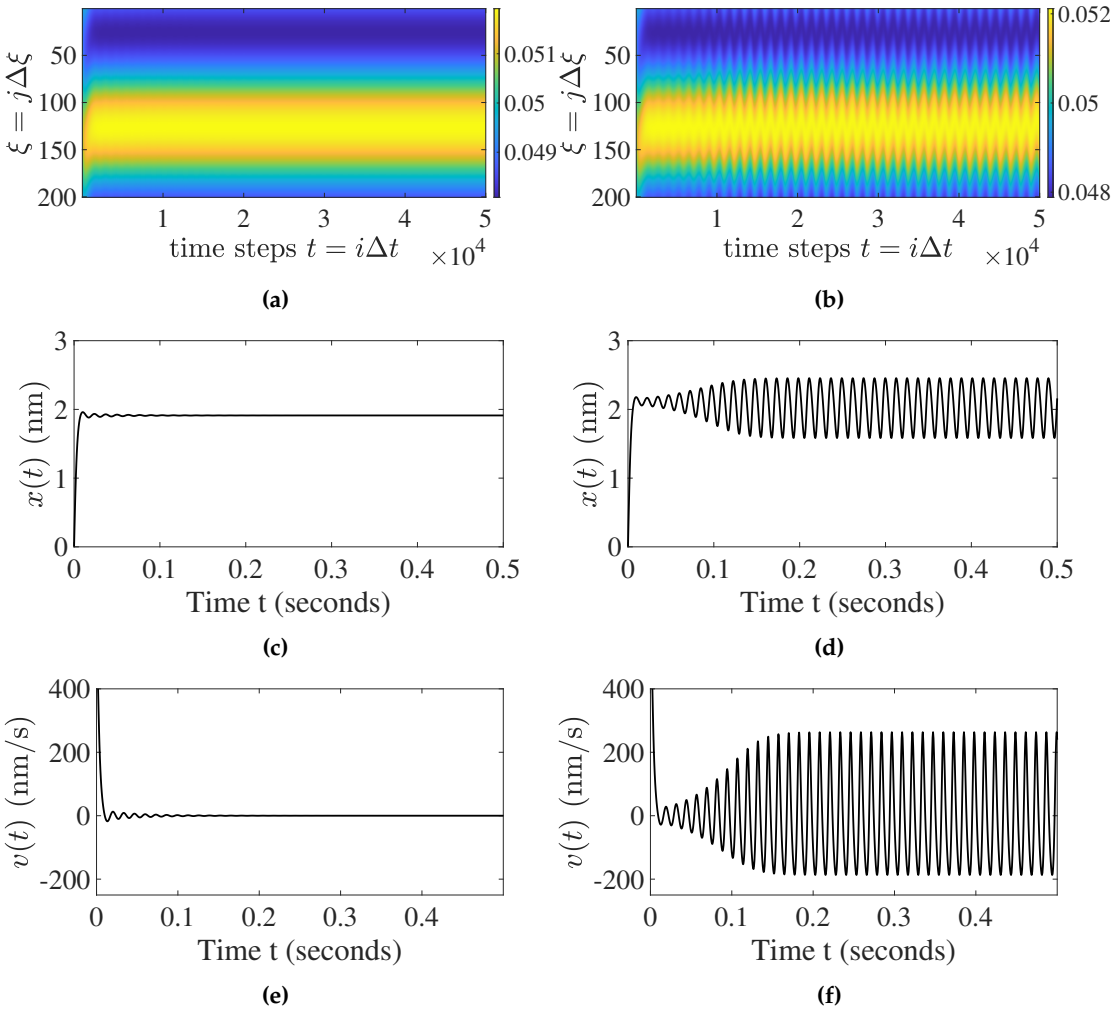

Figure 5.4. One-row model. On the left ((a), (c), (e)) we observe $P(\xi, t)$, $x(t)$ and $v(t)$ when the ATP concentration Ω is less then Ω_0, the system reach its non moving equilibrium. On the right ((b), (d), (f)), we see the same quantities with $\Omega > \Omega_0$, all of them oscillate in time.

The system needs a specific ATP concentration Ω_0 to start moving. This can be observed in Figure 5.4. Here, we plot the graphs of $P(\xi, t)$ in the periodicity cell $[0, \ell]$ for the space variable ξ. When $\Omega < \Omega_0$, the system quickly goes to its equilibrium state. The filament does not move and maintains a non-zero displacement, $x_0 \neq 0$, as shown in Figures 5.4(a), 5.4(c) and 5.4(e). In this regime, the quantity $P(\xi, t)$, which is the probability of finding a motor with the right head attached to the filament and the left head detached from it, is constant in time. Lastly, due to our choices for the transition rates, the natural equilibrium configuration of the motor's heads is not independent from the position in space.

As soon as the system with elastic links attains enough chemical energy (namely, $\Omega > \Omega_0$), the position of the filament, together with the motor density P, oscillate around their equilibrium positions, as in Figures 5.4(d) and 5.4(f).

Notice that, since the transition rates are not symmetric, the equilibrium displacement for the one-row model is different from zero (Figures 5.4(c) and 5.4(d)).

It is also known that the dynamical behavior of the filament depends on the presence of elastic elements. They are defined through the elastic force $-kx(t)$, with $k \neq 0$. If enough chemical ATP is given to the system, namely $\Omega > \Omega_0$, then the filament is expected to deviate from its equilibrium position. If no elastic elements are present, i.e. $k = 0$, then the motors walk and the filament slides, with $v(t) \neq 0$, in one arbitrary direction. In this case, $|x|$ keeps growing until both filaments are not connected to one another (through the motors) anymore. Instead, if $k \neq 0$, the filament starts to oscillate.

5.3 *Introducing the two-row model*

5.3.1 *Model structure*

We now derive in detail the system (5.2), which is depicted in Figure 5.3(b). We consider three pairs of filaments, numbered from 0 to 2. The pairs 0 and 2 are identical, and fixed, while the (central) pair 1, may move. We call $x(t)$ its displacement, and $v(t) = \frac{d}{dt}x(t)$ its velocity. We define $P_1(\xi, t)$ and $P_2(\xi, t)$ as the probabilities for the motors to be in state one at position ξ and time t, when attached to the pair 1 (bottom row) or to the pair 2 (top row), respectively. We obtain for $\xi \in [0, \ell]$ and $t > 0$, two transport equations (still assuming (5.3)):

$$\begin{cases} \dfrac{\partial P_1}{\partial t}(\xi, t) + v(t)\dfrac{\partial P_1}{\partial \xi}(\xi, t) = -a_0(\Omega)P_1(\xi, t) + \dfrac{\omega_2(\xi; \Omega)}{\ell}, \\ \dfrac{\partial P_2}{\partial t}(\xi, t) = -a_0(\Omega)P_2(\xi, t) + \dfrac{\omega_2(\xi - x(t); \Omega)}{\ell}. \end{cases} \tag{5.9}$$

Moreover, the force balance equation reads:

$$f_{ext} - 2\eta v - 2kx + f_{mot} = 0,$$

where f_{ext} is the external force applied on the central filament and f_{mot} is the force exerted by the motors on it, which is defined as

$$f_{mot}(t) = \int_0^\ell (P_1(\xi, t)\partial_\xi \Delta W(\xi) - P_2(\xi, t)\partial_\xi \Delta W(\xi - x(t)))d\xi. \tag{5.10}$$

For the purpose of our work, we do not consider any external forcing, which means $f_{ext} = 0$. Let $P(\xi,t) = P_1(\xi,t)$ and $Q(\xi,t) = P_2(\xi + x(t), t)$. Then, (5.9) becomes

$$\begin{cases} \dfrac{\partial P}{\partial t}(\xi,t) + v(t)\dfrac{\partial P}{\partial \xi}(\xi,t) = -a_0(\Omega)P(\xi,t) + \dfrac{\omega_2(\xi)}{\ell}, \\ \dfrac{\partial Q}{\partial t}(\xi,t) - v(t)\dfrac{\partial Q}{\partial \xi}(\xi,t) = -a_0(\Omega)Q(\xi,t) + \dfrac{\omega_2(\xi)}{\ell}. \end{cases} \tag{5.11}$$

The periodicity of P_1 and P_2, enables us to rewrite the motor force as

$$f_{mot}(t) = \int_0^\ell (P(\xi,t) - Q(\xi,t))\partial_\xi \Delta W(\xi) d\xi \,,$$

and obtain

$$v(t) = \dot{x}(t) = \frac{1}{2\eta}\left(\int_0^\ell (P(\xi,t) - Q(\xi,t))\partial_\xi \Delta W(\xi) d\xi - 2kx(t)\right). \tag{5.12}$$

Finally, we recover the system of equations (5.2), which will then be studied both theoretically and numerically, before generalizing it to an arbitrary number of layers N.

5.3.2 *Proof of Theorem 5.1.1 (existence and uniqueness)*

The proof follows a classical scheme in two steps: we first show local existence of the solutions in time, and then extend it globally in $\mathbb{R}_+$.

Step 1: local existence. Let $T > 0$ be a time to be chosen afterwards and define the map $\psi : C^0([0,T]) \to C^0([0,T])$ as $\psi[x(\cdot)](t) = \displaystyle\int_0^t F[x(\cdot)](s)\, ds$, where

$$F[x(\cdot)](s) = \frac{1}{2\eta}\left(\int_0^\ell (P_x(\xi,s) - Q_x(\xi,s))\partial_\xi \Delta W(\xi) d\xi - 2kx(s)\right), \tag{5.13}$$

and the functions $P_x(\xi,t)$ and $Q_x(\xi,t)$ are defined as the solutions of (5.11) and $v(t) = \dot{x}(t)$. Notice that P_x and Q_x are explicitly given in their integral form by

$$P_x(\xi,t) = e^{-a_0 t}P(\xi - x(t) + x(0), 0) + \frac{e^{-a_0 t}}{\ell}\int_0^t e^{a_0 s}\omega_2(\xi + x(s) - x(t))\, ds. \tag{5.14}$$

and

$$Q_x(\xi,t) = e^{-a_0 t}Q(\xi + x(t) - x(0), 0) + \frac{e^{-a_0 t}}{\ell}\int_0^t e^{a_0 s}\omega_2(\xi - x(s) + x(t))\, ds, \tag{5.15}$$

which remain well-defined when x is only in $C^0([0,T])$.

Notice that $(\tilde{x}, P_{\tilde{x}}, Q_{\tilde{x}})$ is a solution of the system (5.11, 5.12) if and only if $\tilde{x}(t)$ is a fixed point of ψ, i.e. $\psi[\tilde{x}(\cdot)] = \tilde{x}(\cdot)$. In order to proceed, we prove that $\psi : C^0([0,T]) \to$

$C^0([0,T])$ is a strict contraction for T sufficiently small.

Let us take two functions x_1 and x_2 in $C^0([0,T])$, with $x_1(0) = x_2(0) = 0$ and with the corresponding P_{x_1}, Q_{x_1} and P_{x_2}, Q_{x_2} defined by the integral formulations (5.14, 5.15). The initial conditions are identical $P_{x_1}(\xi,0) = P_{x_2}(\xi,0) = P(\xi)$ and $Q_{x_1}(\xi,0) = Q_{x_2}(\xi,0) = Q(\xi)$. We want to estimate the quantity

$$\psi[x_1(\cdot)](t) - \psi[x_2(\cdot)](t) = \int_0^t F[x_1(\cdot)](s) - F[x_2(\cdot)](s)\, ds. \tag{5.16}$$

Using (5.13), we get

$$\begin{aligned} F[x_1(\cdot)](s) - F[x_2(\cdot)](s) = \frac{1}{2\eta}\Bigg(\int_0^\ell \Big(& P_{x_1}(\xi,s) - P_{x_2}(\xi,s) \\ & - \big(Q_{x_1}(\xi,s) - Q_{x_2}(\xi,s)\big)\Big)\partial_\xi \Delta W(\xi) d\xi \Bigg) - \frac{k}{\eta}(x_1(s) - x_2(s)). \end{aligned} \tag{5.17}$$

Now, we have from (5.14)

$$\begin{aligned} P_{x_1}(\xi,t) - P_{x_2}(\xi,t) = {} & e^{-a_0 t}(P_{x_1}(\xi - x_1(t),0) - P_{x_2}(\xi - x_2(t),0)) \\ & + \frac{e^{-a_0 t}}{\ell}\int_0^t e^{a_0 s}(\omega_2(\xi + x_1(s) - x_1(t)) - \omega_2(\xi + x_2(s) - x_2(t))\, ds. \end{aligned} \tag{5.18}$$

We have the estimate

$$\begin{aligned} & \|P_{x_1}(t,\xi) - P_{x_2}(t,\xi)\|_{L_t^\infty L_\xi^\infty} \\ & \le \|\partial_\xi P\|_{L_\xi^\infty} \|x_1(t) - x_2(t)\|_{L_t^\infty} \\ & \quad + \frac{1}{\ell}\left\| \int_0^t e^{a_0(s-t)} \|\partial_\xi \omega_2\|_{L_\xi^\infty} |x_1(s) - x_1(t) - x_2(s) + x_2(t))|\, ds \right\|_{L_t^\infty} \\ & \le \left(\|\partial_\xi P\|_{L_\xi^\infty} + \frac{2}{a_0 \ell}\|\partial_\xi \omega_2\|_{L_\xi^\infty} \right) \|x_1(t) - x_2(t)\|_{L_t^\infty}, \end{aligned}$$

The same goes for the difference $Q_{x_1}(\xi,t) - Q_{x_2}(\xi,t)$, and we deduce

$$\|P_{x_1}(t,\xi) - P_{x_2}(t,\xi) - Q_{x_1}(t,\xi) + Q_{x_2}(t,\xi)\|_{L_t^\infty L_\xi^\infty} \le C_1 \|x_1(t) - x_2(t)\|_{L_t^\infty}. \tag{5.19}$$

with $C_1 = 4\max\left\{ \|\partial_\xi Q\|_{L_\xi^\infty}, \|\partial_\xi P\|_{L_\xi^\infty}, \frac{2}{a_0 \ell}\|\partial_\xi \omega_2\|_{L_\xi^\infty} \right\}$.

We now deduce from (5.17)

$$\|F[x_1(\cdot)] - F[x_2(\cdot)]\|_{L_t^\infty} \le \left(\frac{C_1 \ell}{2\eta}\|\partial_\xi \Delta W\|_{L_\xi^\infty} + \frac{k}{\eta} \right) \|x_1(t) - x_2(t)\|_{L_t^\infty}, \tag{5.20}$$

and obtain

$$\|\psi[x_1(\cdot)] - \psi[x_2(\cdot)]\|_{L_t^\infty} \le C_2 T \|x_1 - x_2\|_{L_t^\infty}, \tag{5.21}$$

with $C_2 = \frac{C_1 \ell}{2\eta}\|\partial_\xi \Delta W\|_{L_\xi^\infty} + k/\eta$.

Taking $T = \frac{1}{2C_2}$, this proves that ψ is a contraction, as claimed. Then, there exists a unique fixed point $\tilde{x}(\cdot) \in C^0([0,T])$ which satisfies (5.12).

Step 2: global solutions. The previous construction can be extended as long as P_x and Q_x remain bounded in $C^1([0,\ell])$, as shown by the formulas for C_1 and C_2. But from (5.14, 5.15) we have

$$\|P_x(\cdot,t)\|_{C^1_\xi} \leq e^{-a_0 t}\|P\|_{C^1_\xi} + (1-e^{-a_0 t})\frac{1}{a_0\ell}\|\omega_2\|_{C^1_\xi},$$

which shows that

$$\|P_x\|_{C^1_\xi, L^\infty_t} \leq \max\left(\|P\|_{C^1_\xi}, \frac{1}{a_0\ell}\|\omega_2\|_{C^1_\xi}\right),$$

and the same goes for Q_x. We thus obtain that there is a unique global solution $(x,\, P_x,\, Q_x)$ to (5.11, 5.12) for all time $t \geq 0$.

In fact, $x \in C^1(\mathbb{R}_+)$ and $P_x,\, Q_x \in C^1([0,\ell]\times\mathbb{R}_+)$ as shown by the following bootstrap argument: From equations (5.14, 5.15), we know that P_x and Q_x are continuous in time, which enables us to deduce that $F[x(\cdot)] \in C^0(\mathbb{R}_+)$. Therefore, $\psi[x(\cdot)] \in C^1(\mathbb{R}_+)$. But, since $x = \psi[x(\cdot)]$, we deduce that $x \in C^1(\mathbb{R}_+)$. Re-using equations (5.14, 5.15), we may then deduce that P_x and Q_x are in fact C^1 in time (and they actually have the minimal regularity of the initial conditions P, Q and of ω_2).

5.3.3 *Proof of Theorem 5.1.2 (Hopf bifurcation)*

The functions $\xi \mapsto P(\xi,t)$ and $\xi \mapsto Q(\xi,t)$ are periodic with period l, and they can be then expanded in Fourier series

$$\begin{cases} P(\xi,t) = \dfrac{p_0(t)}{2} + \displaystyle\sum_{n>0}\left(p_n^c(t)\cos\frac{2n\pi\xi}{\ell} + p_n^s(t)\sin\frac{2n\pi\xi}{\ell}\right), \\ Q(\xi,t) = \dfrac{q_0(t)}{2} + \displaystyle\sum_{n>0}\left(q_n^c(t)\cos\frac{2n\pi\xi}{\ell} + q_n^s(t)\sin\frac{2n\pi\xi}{\ell}\right). \end{cases} \tag{5.22}$$

We insert this expansion and the one for the transition rates (5.4) into the system (5.2). By matching same order terms, we get an infinite number of ordinary differential equations for the coefficients of P and Q. Namely, for $n = 0$ we get two decoupled equations for p_0 and q_0:

$$\dot{p_0}(t) = -a_0(\Omega)p_0(t) + a_0(\Omega)/2\ell, \quad \dot{q_0}(t) = -a_0(\Omega)q_0(t) + a_0(\Omega)/2\ell. \tag{5.23}$$

For $n \neq 0$ we obtain:

$$\begin{cases} \dot{p_n^c}(t) + \frac{2\pi n}{\ell}v(t)p_n^s(t) = -a_0(\Omega)p_n^c(t) + a_n(\Omega)/\ell\,, \\ \dot{p_n^s}(t) - \frac{2\pi n}{\ell}v(t)p_n^c(t) = -a_0(\Omega)p_n^s(t) + b_n(\Omega)/\ell\,, \\ \dot{q_n^c}(t) - \frac{2\pi n}{\ell}v(t)q_n^s(t) = -a_0(\Omega)q_n^c(t) + a_n(\Omega)/\ell\,, \\ \dot{q_n^s}(t) + \frac{2\pi n}{\ell}v(t)q_n^c(t) = -a_0(\Omega)q_n^s(t) + b_n(\Omega)/\ell\,, \end{cases} \tag{5.24}$$

together with the force balance equation

$$2\eta\dot{x}(t) + 2kx(t) + \pi U(p_1^s - q_1^s) = 0\,. \tag{5.25}$$

Note that the coupling between the probabilities evolution and the force equilibrium equation takes place only for the first order coefficients. We are going to prove the existence of a Hopf bifurcation by treating order $n = 0$ first, then $n = 1$ and lastly $n > 1$. Combining all three results will complete the proof.

Step 1. Zeroth order coefficients. It is clear that (5.23) gives

$$p_0(t) = e^{-a_0 t}\left(p_0(0) - \frac{1}{2l}\right) + \frac{1}{2\ell}\,, \quad q_0(t) = e^{-a_0 t}\left(q_0(0) - \frac{1}{2l}\right) + \frac{1}{2\ell}\,,$$

and both converge to $\frac{1}{2\ell}$ exponentially fast.

Step 2. First order coefficients. We now prove the onset of oscillatory patterns for the first order coefficients $p_1^{c,s}(t)$, $q_1^{c,s}(t)$, and for the position $x(t)$.

From (5.24) and (5.25) we obtain a first-order five-dimensional ODE:

$$\begin{cases} \dot{p_1^c} = -a_0(\Omega)p_1^c + \big(\zeta x + \dfrac{\lambda}{2}(p_1^s - q_1^s)\big)p_1^s + \dfrac{a_1(\Omega)}{\ell}, \\ \dot{p_1^s} = -a_0(\Omega)p_1^s - \big(\zeta x + \dfrac{\lambda}{2}(p_1^s - q_1^s)\big)p_1^c + \dfrac{b_1(\Omega)}{\ell}, \\ \dot{q_1^c} = -a_0(\Omega)q_1^c - \big(\zeta x + \dfrac{\lambda}{2}(p_1^s - q_1^s)\big)q_1^s + \dfrac{a_1(\Omega)}{\ell}, \\ \dot{q_1^s} = -a_0(\Omega)q_1^s + \big(\zeta x + \dfrac{\lambda}{2}(p_1^s - q_1^s)\big)q_1^c + \dfrac{b_1(\Omega)}{\ell}, \\ \dot{x} = -\dfrac{\ell}{2\pi}\big(\zeta x + \dfrac{\lambda}{2}(p_1^s - q_1^s)\big)\,, \end{cases} \tag{5.26}$$

where $\zeta = 2\pi k/\eta\ell$ and $\lambda = 2\pi^2 U/\eta\ell$.

We linearize the system around its equilibrium point

$$p_{eq} = (p_{1,\mathrm{eq}}^c(\Omega), p_{1,\mathrm{eq}}^s(\Omega), q_{1,\mathrm{eq}}^c(\Omega), q_{1,\mathrm{eq}}^s(\Omega), x_{\mathrm{eq}}(\Omega)),$$

where

$$p_{1,eq}^c = q_{1,eq}^c = \frac{a_1(\Omega)}{a_0(\Omega)\ell}\,,\ \ p_{1,eq}^s = q_{1,eq}^s = \frac{b_1(\Omega)}{a_0(\Omega)\ell}\,,\ \ x_{eq} = 0\,.$$

We observe that the Jacobian matrix has five eigenvalues: three of them are equal to $-a_0(\Omega) < 0$ while the other two are of the form $\tau(\Omega) \pm \frac{1}{2\sqrt{\pi}}\sqrt{-2\zeta\ell a_0(\Omega) + \pi\,\tau^2(\Omega)}\,$, where $\tau(\Omega)$ is given by (5.5). Since, by hypothesis, there exists a real and positive $\Omega = \Omega_0$ such that $\tau(\Omega_0) = 0$, then $-2\zeta\ell a_0(\Omega_0) + \pi\,\tau^2(\Omega_0) < 0$, and we deduce that the pair of complex eigenvalues can be written as $\tau(\Omega) \pm i\omega(\Omega)$ where

$$\omega(\Omega) := -\frac{1}{2\sqrt{\pi}}\sqrt{2\zeta\ell a_0(\Omega) - \pi\,\tau^2(\Omega)}, \tag{5.27}$$

and they cross the imaginary axis at $\Omega = \Omega_0$.

In the following proposition, we are going to study the non-linear behavior of the vector field solution to (5.26) by exploiting the center manifold theorem; the orbit structure near the fixed point and Ω_0 is determined by the restriction of the non linear system to the center manifold. In particular, system (5.26) restricted to the center manifold will show a super-critical Hopf bifurcation near p_{eq} and Ω_0.

PROPOSITION 5.3.1 · *First order coefficients*

With the hypothesis of Theorem 5.1.2, the non-linear system (5.26) has a supercritical Hopf bifurcation near (p_{eq}, Ω_0).

Proof. **Change of variables.**
In the first part of the proof we restrict the dynamical system to the center manifold. To compute the latter, we bring the system to a more suitable formulation.

Let us first transform the fixed point of (5.26) to the origin. We define the new variables as

$$\delta p_1^c = p_1^c - p_{1,eq}^c,\ \delta p_1^s = p_1^s - p_{1,eq}^s,\ \delta q_1^c = q_1^c - q_{1,eq}^c,\ \delta q_1^s = q_1^s - q_{1,eq}^s.$$

We then use the following linear and invertible change of variables

$$r = \tfrac{a_1}{b_1}\delta p_1^c + \delta p_1^s, \quad s = \tfrac{a_1}{b_1}\delta q_1^c + \delta q_1^s, \quad z = \tfrac{1}{2}(\delta p_1^s + \delta q_1^s), \quad y = \tfrac{1}{2}(\delta p_1^s - \delta q_1^s).$$

This choice for the change of variables and the various steps to reach this result are justified in more detail in the Appendix 5.7. We now shorten the notation by taking $X = (r, s, z)^T$, and $Y = (y, x)^T$ to transform the system (5.26) into

$$\frac{d}{dt}\begin{pmatrix} X \\ Y \end{pmatrix} = \mathbb{M}(\Omega)\begin{pmatrix} X \\ Y \end{pmatrix} + \begin{pmatrix} G(X,Y) \\ F(X,Y) \end{pmatrix}, \tag{5.28}$$

where

$$\mathbb{M}(\Omega) = \begin{pmatrix} \mathbb{B}(\Omega) & 0 \\ 0 & \mathbb{A}(\Omega) \end{pmatrix}$$

is a block diagonal matrix, with

$$\begin{aligned} \mathbb{B}(\Omega) &:= -a_0^0\Omega^{\alpha_0}\mathrm{Id}_{3,3}\,, \\ \mathbb{A}(\Omega) &:= \begin{pmatrix} -a_0^0\Omega^{\alpha_0} - \frac{\lambda}{\ell}\frac{a_1^0}{a_0^0}\Omega^{\alpha_1-\alpha_0} & -\frac{a_1^0}{a_0^0}\frac{\zeta}{\ell}\Omega^{\alpha_1-\alpha_0} \\ -\frac{\lambda\ell}{2\pi} & -\frac{\zeta\ell}{2\pi} \end{pmatrix}, \end{aligned} \tag{5.29}$$

and the non linear part is defined as

$$G(X,Y) = (\zeta x + \lambda y)\begin{pmatrix} \frac{a_1^0}{b_1^0}(y+z) + \frac{b_1^0}{a_1^0}(-r+y+z) \\ \frac{a_1^0}{b_1^0}(y-z) + \frac{b_1^0}{a_1^0}(s+y-z) \\ -\frac{b_1^0}{a_1^0}\frac{(r-s-2y)}{2} \end{pmatrix},$$

and

$$F(X,Y) = (\zeta x + \lambda y)\begin{pmatrix} -\frac{b_1^0}{a_1^0}\frac{(r+s-2z)}{2} \\ 0 \end{pmatrix}. \tag{5.30}$$

Computation of the center manifold.

The center manifold can then be computed by using standard techniques reported, for example, in [106]. We start by rewriting the system in such a way that Ω_0 is moved to the origin through the change of variable $\delta\Omega = \Omega - \Omega_0$. As it is classical, we treat $\delta\Omega$ as a variable of the system. This means that we add the equation $\delta\dot{\Omega} = 0$ to the dynamical system and that the non linear part of the system includes all the products $\delta\Omega\, r$, $\delta\Omega\, s$, $\delta\Omega\, z$ etc.

Since the terms in the matrix $\mathbb{M}$ are nonlinear in Ω, we expand them defining

$$(\Omega_0 + \delta\Omega)^\alpha = \Omega_0^\alpha + c(\alpha)\,\delta\Omega + O(\delta\Omega^2),$$

where $c(\alpha) = \alpha\Omega_0^{\alpha-1}$.

The system becomes

$$\frac{d}{dt}\begin{pmatrix} X \\ Y \\ \delta\Omega \end{pmatrix} = \mathbb{M}(\Omega_0)\begin{pmatrix} X \\ Y \\ 0 \end{pmatrix} + \begin{pmatrix} g(X,Y,\delta\Omega) \\ f(X,Y,\delta\Omega) \\ 0 \end{pmatrix}, \tag{5.31}$$

with

$$g(X,Y,\delta\Omega) = -a_0^0 c(\alpha_0)\delta\Omega X + G(X,Y)$$

and

$$f(X,Y,\delta\Omega) = -\begin{pmatrix} \left(a_0^0 c(\alpha_0) y + \frac{\lambda}{\ell}\frac{a_1^0}{a_0^0}c(\alpha_1-\alpha_0)\right)\delta\Omega\, y + \frac{\zeta}{\ell}c(\alpha_1-\alpha_0)\delta\Omega\, x \\ 0 \end{pmatrix} + F(X,Y).$$

We can define a center manifold as

$$W^c(0) = \{(X,Y,\delta\Omega) : X = \mathbf{h}(Y,\delta\Omega), |Y| < \varepsilon, |\delta\Omega| < \bar{\varepsilon}, \mathbf{h}(0,0) = 0,\ \nabla\mathbf{h}(0,0) = 0\},$$

for ε and $\bar{\varepsilon}$ sufficiently small and $\mathbf{h} = (h_1, h_2, h_3)$ smooth enough.

In order for $\mathbf{h}$ to be the center manifold for the system (5.31), the graph of $\mathbf{h}(Y, \delta\Omega)$ has to be invariant under the dynamics generated by (5.31). Hence, by plugging $\mathbf{h}$ into the system and compute its derivative, we get the following quasilinear differential equation

$$\nabla_Y \mathbf{h} \cdot (\mathbb{A}(\Omega_0)Y + f(\mathbf{h}, Y, \delta\Omega)) = \mathbb{B}(\Omega_0)\mathbf{h} + g(\mathbf{h}, Y, \delta\Omega). \tag{5.32}$$

The solution $\mathbf{h}(Y, \delta\Omega)$ of (5.32) can be approximated with a power series expansion up to any desired degree of accuracy (see [106]). In our case we expand them up to order two defining

$$h_i(Y, \delta\Omega) := a_{i1}y^2 + a_{i2}yx + a_{i3}y\delta\Omega + a_{i4}x^2 + a_{i5}x\delta\Omega + a_{i6}\delta\Omega^2 + O(Y^3, \delta\Omega^3). \tag{5.33}$$

To completely determine (locally) the center manifold, we have to compute the coefficients a_{ij} knowing that the functions defined in (5.33) must solve (5.32). For the detailed computations, we refer the reader to Appendix 5.6.

Restricted to the center manifold, the original system (5.28) has the following form:

$$\frac{d}{dt}Y = \mathbb{A}(\Omega)Y + f(\mathbf{h}(Y), Y) + O(Y^3, \delta\Omega^3)\,. \tag{5.34}$$

A complete formula for $f(\mathbf{h}(Y), Y))$ in terms of $Y = (y, x)^T$ follows from our computations and reads

$$f(\mathbf{h}(Y), Y) = \begin{pmatrix} \dfrac{2\pi a_0^0 \ell(\lambda y + \zeta x)\left(\pi a_1^0 \Omega_0^{\alpha_1-\alpha_0}\left(\lambda^2 y^2 + \zeta^2 x^2\right) + \zeta a_0^0 \ell(\pi a_0^0 \Omega_0^{\alpha_0} - \zeta\ell)yx\right)}{\left(2\pi a_1^0 \lambda \Omega_0^{\alpha_1-\alpha_0} + \zeta a_0^0 \ell^2\right)\left(2\pi a_1^0 \lambda \Omega_0^{\alpha_1-\alpha_0} + a_0^0 \ell(\pi a_0^0 \Omega_0^{\alpha_0} - \zeta\ell)\right)} \\ 0 \end{pmatrix}.$$

Observe that $\tau(\Omega) \pm i\omega(\Omega)$ is the pair of conjugated eigenvalues of $\mathbb{A}(\Omega)$ and therefore we are in the hypothesis of the existence of a Hopf bifurcation for a two-dimensional system.

Normal form.

The next step is to bring system (5.34) into its normal form, from which we deduce the type of Hopf bifurcation that the system is attaining.

In order to proceed, we apply a further change of coordinates, such that $\mathbb{A}(\Omega)$ is transformed to its real Jordan form. Namely, we define the transformation matrix

$$\mathbb{P} = \begin{pmatrix} P_{11} & P_{12} \\ 1 & 0 \end{pmatrix},$$

where

$$P_{11} = \frac{\pi}{\lambda\ell}\left(\frac{a_1^0 \lambda \Omega_0^{\alpha_1-\alpha_0}}{a_0^0 \ell} + a_0^0 \Omega_0^{\alpha_0}\right) - \frac{\zeta}{2\lambda}$$

and

$$P_{12} = -\frac{1}{\lambda\ell}\sqrt{\pi\zeta\ell\left(a_0^0\Omega_0^{\alpha_0} - \frac{a_1^0\lambda\Omega_0^{\alpha_1-\alpha_0}}{a_0^0\ell}\right) - \left(\frac{\pi a_1^0\lambda\Omega_0^{\alpha_1-\alpha_0}}{a_0^0\ell} + \pi a_0^0\Omega_0^{\alpha_0}\right)^2 - \frac{\zeta^2\ell^2}{4}}.$$

The matrix $\mathbb{P}$ defines the new coordinates $Y = \mathbb{P}\tilde{Y}$ thanks to which equation (5.34) can be expressed in its normal form

$$\frac{d}{dt}\tilde{Y} = \begin{pmatrix}\tau(\Omega) & -\omega(\Omega)\\ \omega(\Omega) & \tau(\Omega)\end{pmatrix}\tilde{Y} + \mathbb{P}^{-1}f(\mathbf{h}(\mathbb{P}\tilde{Y}), \mathbb{P}\tilde{Y}) + O(Y^3, \delta\Omega^3). \tag{5.35}$$

To compute key properties of the system, such as the amplitude of the limit cycles, we change coordinates to the polar ones $\tilde{Y}^T = \rho(\sin(\theta), \cos(\theta))$, and get

$$\begin{cases}\dot{\rho}(t) = \tau'(\Omega_0)\delta\Omega\rho(t) + \tilde{\tau}\rho^3(t) + O(\delta\Omega^2\rho, \delta\Omega\rho^3),\\ \dot{\theta}(t) = \omega(\Omega_0) + \omega'(\Omega_0)\delta\Omega + \tilde{\omega}\rho^2(t) + O(\delta\Omega^2, \delta\Omega\rho^2).\end{cases}, \tag{5.36}$$

that is the normal form of (5.34) in polar coordinates around Ω_0.

The non linear part $\mathbb{P}^{-1}f(\mathbf{h}(\mathbb{P}\tilde{Y}), \mathbb{P}\tilde{Y})$ determines the constants $\tilde{\tau}$ and $\tilde{\omega}$. The first one is involved in the expression for the limit cycle amplitude, and we compute it using a formula given in [106]. We obtain

$$\tilde{\tau} = -\frac{3\pi\zeta}{4\ell}\left(\frac{\pi a_0^0\Omega_0^{\alpha_0} + \ell\zeta}{\pi a_0^0\Omega_0^{\alpha_0} + 2\ell\zeta}\right)$$

Since $\tilde{\tau}$ is negative and

$$\tau'(\Omega_0) = -\frac{1}{2}\left(\frac{a_1^0\lambda\alpha_1 - \alpha_0\Omega^{\alpha_1-\alpha_0-1}}{a_0^0\ell} + \alpha_0 a_0^0\Omega^{\alpha_0-1}\right),$$

is positive by hypothesis, the reduced system (5.34), and hence, the whole system (5.28), shows a supercritical Hopf bifurcation near the bifurcation parameter Ω_0.

In particular, for Ω sufficiently near and greater then Ω_0 there exists an asymptotically stable periodic orbit with radius as in (5.6). This finishes the proof of Proposition 5.3.1 □

Step 3. Higher order terms. Lastly, we are going to prove that, after large times, the solutions of (5.24) $p_n^{c,s}(t)$ and $q_n^{c,s}(t)$, with $n > 1$ are periodic with the same period as $x(t)$. We remark again that, since the dynamics of x (5.25) is independent of p_n^c, p_n^s, q_n^c, q_n^s for $n > 1$, we may assume that $x(t)$ is given and periodic, and split the system into pairs of coupled equations as stated in the following Proposition.

PROPOSITION 5.3.2 · *Higher order coefficients*

For $n > 1$ consider the infinite system of four equations:

$$\begin{cases} \dot{p}_n^c(t) + \dfrac{2\pi n}{\ell}\dot{x}p_n^s(t) = -a_0(\Omega)p_n^c(t) + a_n(\Omega)/\ell, \\ \dot{p}_n^s(t) - \dfrac{2\pi n}{\ell}\dot{x}p_n^c(t) = -a_0(\Omega)p_n^s(t) + b_n(\Omega)/\ell. \end{cases} \tag{5.37}$$

and

$$\begin{cases} \dot{q}_n^c(t) - \dfrac{2\pi n}{\ell}\dot{x}q_n^s(t) = -a_0(\Omega)q_n^c(t) + a_n(\Omega)/\ell, \\ \dot{q}_n^s(t) + \dfrac{2\pi n}{\ell}\dot{x}q_n^c(t) = -a_0(\Omega)q_n^s(t) + b_n(\Omega)/\ell. \end{cases} \tag{5.38}$$

Suppose that, for $t \geq 0$, the function $t \mapsto x(t)$ is periodic of period T. Then, the solutions to the systems (5.37) and (5.38) may have two behaviors: they either converge in time to periodic solutions of the same period T if n is odd, or they go to zero for large times when n is even.

Proof. We introduce $z_n = p_n^c + ip_n^s$. The first two equations of (5.37) then become:

$$\dot{z}_n + \left(a_0(\Omega) - \frac{2in\pi}{\ell}\dot{x}\right) z_n = c_n \tag{5.39}$$

with $c_n = \dfrac{a_n(\Omega) + ib_n(\Omega)}{\ell}$ is constant. We thus deduce the following expression for $z_n(t)$

$$z_n(t) = c_n \int_0^t e^{-\int_u^t (a_0(\Omega) - i\bar{v}(s))ds} du + z_n(0) e^{-\int_0^t (a_0(\Omega) - i\bar{v}(s))ds}, \tag{5.40}$$

where $\bar{v} = \frac{2n\pi}{\ell}\dot{x}$.

Let us first notice that the second term, $z_n(0)e^{-\int_0^t (a_0(\Omega) - i\bar{v}(s))ds}$ goes to zero when t goes to infinity. This, together with the fact that $a_n = b_n = 0$ if n is even (see (5.4)), gives $c_n = 0$ and the solutions $p_n^{c,s}$ go to zero for large times when n is even.

Let us now focus on the case where n is odd. We want to prove that, when $\bar{v}$ is periodic of period T, z_n converges towards a T-periodic solution after a transitory regime. We again notice that the second term of (5.40) converges to 0, and the result will follow by studying only the first term.

We thus denote by $\tilde{z}_n(t) = \int_0^t e^{-\int_u^t (a_0 - i\bar{v}(s))ds} du$, and compute

$$\begin{aligned}\tilde{z}_n(T+t) - \tilde{z}_n(t) &= \int_0^{t+T} e^{-\int_u^{t+T} (a_0 - i\bar{v}(s))ds} du - \int_0^t e^{-\int_u^t (a_0 - i\bar{v}(s))ds} du \\ &= \int_0^T e^{-\int_u^{t+T} (a_0 - i\bar{v}(s))ds} du + \int_T^{t+T} e^{-\int_u^{t+T} (a_0 - i\bar{v}(s))ds} du \\ &\quad - \int_0^t e^{-\int_u^t (a_0 - i\bar{v}(s))ds} du\,.\end{aligned} \tag{5.41}$$

Using the fact that $\bar{v}$ is T-periodic, the last two terms cancel and we obtain

$$\begin{aligned}\tilde{z}_n(T+t) - \tilde{z}_n(t) &= \int_0^T e^{-\int_u^{t+T} (a_0 - i\bar{v}(s))ds} du \\ &= e^{-(t+T)a_0} \int_0^T e^{ua_0 + \int_u^{t+T} i\bar{v}(s)ds} du\end{aligned}$$

which goes to 0 when t goes to infinity.

We therefore proved that z_n converges to a T-periodic function. The same result holds for (q_n^c, q_n^s) solution to (5.38). □

Finally, if we have initial conditions that are close to the equilibrium point of system (5.2), and an amount of ATP Ω, which is close to Ω_0, we know exactly how the solution of the system evolves in time. The first order coefficients of (5.22) go quickly to the constant term $1/l$, the first order coefficients starts to oscillate in a limit cycle, and the higher order terms either go to zero or have the same patterns as $p_1^{c,s}$ and $q_1^{c,s}$ with same period of oscillation. Globally, the solution of (5.2), shows a supercritical Hopf-bifurcation in time, close enough to the parameter Ω_0.

Remark 5.3.1. We remark that, up until the computation of the center manifold, the coefficients a_0, a_1 and b_1 may remain general: there is no need for the power laws to obtain three negative eigenvalues and two complex eigenvalues in system (5.26). To facilitate the application of center manifold techniques, we have opted to explicitly express the dependence of a_0, a_1, and b_1 on Ω. The selection of power laws is somewhat intuitive, as it extends previous findings ([29],[47]) and proves to be advantageous for our analysis.

Remark 5.3.2. It is worth mentioning the role of b_1 in the dynamics of the two-row system, since we introduce it to point out that x_{eq} for the two-row model is always zero, while for the one-row model this is not the case. First notice that b_1^0 does not appear in $\mathbb{M}$. Moreover, after the restriction to the center manifold, the non linear part $f(\mathbf{h}(Y), Y)$ is independent on b_1^0 too, at least up to third order expansion. Since $\dot{x}(t)$ only depends on Y, the effect of $b_1(\Omega)$ on the displacement solution and its velocity is negligible.

We also remark how the two systems (5.37) and (5.38) depends on $x(t)$ and therefore won't depend on $b_1(\Omega)$, but rather on $a_0(\Omega)$, on $a_n(\Omega)$ with $n > 0$ odd, and on $b_n(\Omega)$ with $n > 1$ odd. On the other hand, we expect the probabilities P and Q to be sensitive to $b_1(\Omega)$, through their first order coefficients.

5.3.4 *Numerical simulations*

Conditions on α_0 and α_1 · In order to implement the numerical simulations, we have to characterize ω_1 and ω_2 by fixing their coefficients. We first set the values for a_0^0 and Ω_0. For simplicity, we impose that $a_n = b_n = 0$ for $n > 1$ since, as observed in Theorem 5.1.2, they have no significant influence over the system's oscillations. We now want to find some a_1^0, α_0, α_1, that verify $\tau(\Omega_0) = 0$ from equation (5.5) and $\tau'(\Omega_0) > 0$. Starting with α_0 and α_1, we search for sufficient conditions such that $\tau'(\Omega_0) > 0$. This inequality reads

$$\frac{1}{2}a_0^0\alpha_0\Omega_0^{\alpha_0-1} - (\alpha_0 - \alpha_1)\frac{\lambda a_1^0}{2a_0^0\ell}\Omega_0^{\alpha_1-\alpha_0-1} < 0,$$

Substituting a_1^0 into it we get

$$a_0^0(2\alpha_0 - \alpha_1)\Omega_0^{\alpha_0} + (\alpha_0 - \alpha_1)\frac{\ell\zeta}{2\pi} < 0. \tag{5.42}$$

The condition (5.42) is fulfilled with different choices for α_0, α_1. A particularly simple solution that we will use hereafter is $\alpha_0 = 1/2$ and $\alpha_1 = 1$. Then, to recover $a_1^0 = a_1^0(\Omega_0)$, we solve $\tau(\Omega_0) = 0$, from equation (5.5), which leads to

$$a_1^0 = -\frac{a_0^0\ell}{2\pi\lambda}\Omega_0^{\alpha_0-\alpha_1}(2a_0^0\Omega_0^{\alpha_0}\pi + \ell\zeta). \tag{5.43}$$

Finally, using the parameter values presented in Table 5.1, we compute a_1^0 at the instability a,d get $a_1^0(\Omega_0) = -56.4588\, s^{-1}$.

Complete PDE simulations · We adapt the numerical scheme presented in section 5.2.1 to the two-row system (5.2). The behaviour of the two-row model with respect to the ATP concentration is comparable with the one for the one-row model.
When the ATP concentration Ω is lower than Ω_0, the central pair does not move from its zero equilibrium position. On the contrary, when the ATP concentration is enough, we observe an oscillatory displacement between microtubules and in the probabilities, as in Figure 5.5.
The main difference between the one-row model and the two-row one concerns the equilibrium position around which the solution $x(t)$ oscillates, as expected. This is clearly illustrated in Figure 5.5(b), where the displacement takes place around zero. The equilibrium position does not create any curvature, meaning it has the potential to bend equally in both directions.

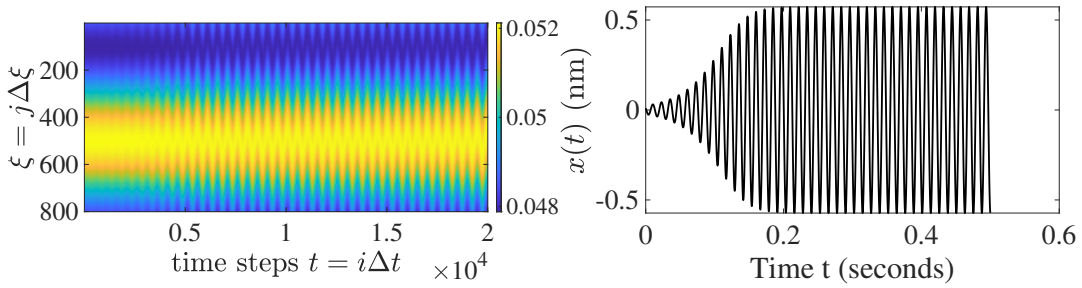

(a) **(b)**

Figure 5.5. Two-row model: (a) Probability density $P_1(\xi, t)$ of the top layer of being in state 1 over time in a periodicity cell, in steady-state regime. (b) Relative tubule shift x (in nm) over time (in s). The probability density $P_2(\xi, t)$ of the bottom layer of being in state 1 is similar to $P_1(\xi, t)$.

Illustrating Theorem 5.1.2 · In the following section, we are going to test the results of Theorem 5.1.2 against numerical simulations of the ordinary differential equations system (5.26) and the partial differential equations system (5.2).

All constants are chosen as described in Table 5.1, and in Section 5.3.4. The parameter δ indicates the relative distance from the instability Ω_0; therefore, the point where the simulations is performed is $\Omega_0(1+\delta)$.

We compute solutions to (5.26) and (5.2) for $\Omega = \Omega_0(1+\delta)$, $\delta > 0$ and focus on the amplitude of oscillations for the displacement. From (5.6), the asymptotic expansion of the theoretical amplitue is

$$\rho(\Omega) = \sqrt{\delta \frac{\ell^2}{6\pi^2} \left(\frac{\pi a_0^0 \Omega_0^{1/2} + 2\ell\zeta}{\pi a_0^0 \Omega_0^{1/2} + \ell\zeta} \right)} + o\left(\sqrt{\Omega - \Omega_0}\right). \tag{5.44}$$

The numerical amplitude is computed by taking the maximum and minimum values of the solution, subtracting them and dividing the result by two. The values are taken after some time $\bar{t}$, when the numerical solution enters in its limit cycle.
In Figure 5.6(a), we observe the amplitude of $x(t)$ computed with the PDE, taken as a reference, the ODE, and the analytical result. In Figure 5.6, simulations only start after $\delta = 0.05$. This is related to the fact that the closer we are to Ω_0, the slower the solution enters into its limit cycle. For this reason, we should have taken a time $\bar{t} = t(\delta)$ after which evaluating the amplitude of $x(t)$. In this case, when δ goes to zero, $\bar{t}(\delta) \to \infty$. In the simulations this was not reasonable, so we chose a time $\bar{t}$ independently from δ, but large enough so that the solution enters in its steady-state regime for all δs. As expected, the last loses its prediction capability the more we go away from the instability; and subsequently, the relative error between the truncated formula (5.44) and the one measured from the PDE increases, as we can see in Figure 5.6(b). This is due to the contribution of the non linear terms, which play a role in determining the amplitude of oscillations even when the system is close to Ω_0.

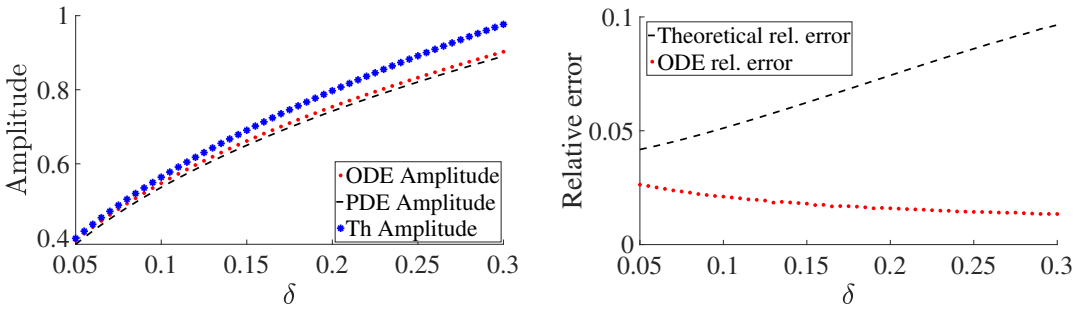

(a) **(b)**

Figure 5.6. Two-row model. (a) Displacement amplitude depending on relative distance to the instability. In blue, the one computed by numerically solving the ODE (5.26) and, in red, the one computed by numerically solving the PDE (5.2) while, in black, the one described by formula (5.44). (b) Relative error between theoretical displacement amplitude and the one measured by the ODE (5.26) in red, and in black between theoretical one and measured one from PDE (5.2).

Comment on the amplitude · The expansion (5.44) of the amplitude ρ can also be adapted to the ODE formulation of the one-row model (5.1). In Figure 5.7, the two-row model does not only center the equilibrium point for the oscillations around zero, but it also influences important physical quantities such as the amplitude of oscillations.

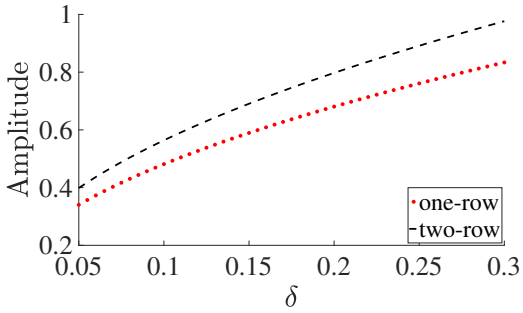

Figure 5.7. Theoretical amplitude for the 2-row model computed with formula (5.44) in black and its equivalent for the 1-row model, in green, against the distance from instability δ.

5.4 *Towards modeling the axoneme: N-layer model with fixed extremities*

Starting from two rows of molecular motors, we extend the model from section 5.3 to $N \geq 2$ rows of molecular motors, without any explicit form of inhibition in the system. The system is then composed of $N+1$ microtubule doublets on the outside, arranged in a circle, and no central pair. All filaments have the same polarity, meaning that between two microtubule pairs, motors move towards the base. To take the bridge of an axoneme into account (as shown in Figure 5.1) in our N-layer model, filament pairs 0 and N are considered to be the same pair. They have no shift between each other, as shown in the split view Figure 5.8. Moreover, all microtubule pairs are assumed inextensible, rigid and at a constant distance from each other. They are held together by elastic and viscous

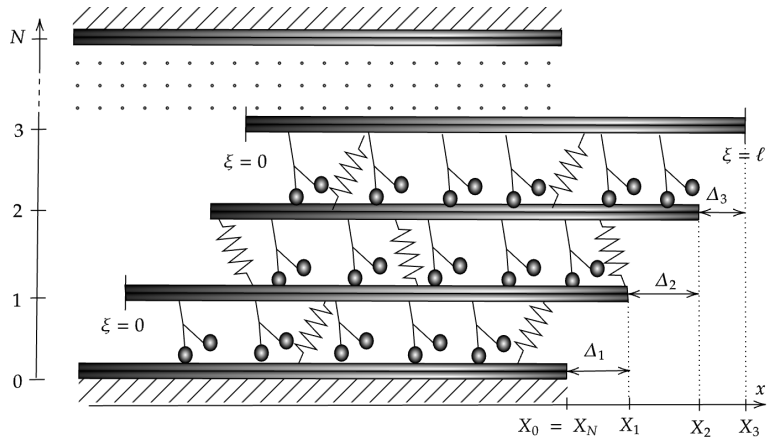

Figure 5.8. Motors and tubule shift in the N-row model (here the horizontal axis x shows absolute tubule displacement instead of motor position ξ in a periodicity cell).

elements that do not permit infinite sliding between them. We look at molecular motors in a periodicity cell of an N-axoneme, of length ℓ.

5.4.1 *Full mathematical model*

For $i \in \{1, \dots, N\}$, we denote by X_i the horizontal shift of the i-th tubule, as shown in Figure 5.8. We measure displacement with respect to the 0-th filament: $X_0 = X_N = 0$. For $1 \leq i \leq N$, we introduce $\Delta_i = X_i - X_{i-1}$, the relative displacement between filaments i and $i-1$. It follows that $\sum_{i=1}^{N} \Delta_i(t) = 0$. The shifting speed of the i-th filament is defined by $V_i = \dot{X}_i - \dot{X}_{i-1} = \dot{\Delta}_i$, and we have

$$\sum_{i=1}^{N} V_i = \sum_{i=1}^{N} \dot{\Delta}_i(t) = 0. \tag{5.45}$$

Once again, the variable $\xi \in [0, \ell]$ represents the local variable along one pair, as in the two-row model. We denote by $Q_i(\xi, t)$ the density of molecular motors at position ξ and time t attached to the i-th filament and who are in state 1, walking on the $(i-1)$-th filament.

As for the two-row model, in section 5.3, $(Q_i,\, \Delta_i)$ are solution to, for $\xi \in [0, \ell]$ and $t > 0$

$$\begin{cases} \partial_t Q_j(\xi, t) = -(\omega_1(\xi - \Delta_j(t), t) + \omega_2(\xi - \Delta_j(t)))Q_j(\xi, t) \\ \qquad\qquad + \omega_2(\xi - \Delta_j(t)))/\ell, \quad \text{for } j \in \{1, \dots, N\}, \\ \eta(V_i(t) - V_{i+1}(t)) = \displaystyle\int_0^\ell (Q_i(\xi, t)\partial_\xi \Delta W(\xi) - Q_{i+1}(\xi, t)\partial_\xi \Delta W(\xi - \Delta_i(t)))d\xi \\ \qquad\qquad - k(\Delta_i(t) - \Delta_{i+1}(t)), \quad \text{for } i \in \{1, \dots, N-1\}. \end{cases} \tag{5.46}$$

Where the first equation is a Fokker-Planck equation for the motors, and the second one is the force balance on the i-th filament. Shifting speed is measured by looking at the current filament, as well as the one above. We thus obtain the second equation in system (5.46) by writing the force balance on the i-th filament with the motors and springs around it. We then have $N-1$ force-balance equations that determine the filaments' motion, in which we impose the external forces to be zero.

Following again section 5.3, for $j \in \{1,\dots,N\}$, $t>0$ and $\xi \in [0,\ell]$, we define P_j as $P_j(\xi,t) = Q_j(\xi+\Delta_j(t),t)$. We then observe that $\partial_t P_j(\xi+\Delta_j,t) = V_j(t)\partial_\xi Q_j(\xi,t) + \partial_t Q_j(\xi,t)$, and we finally obtain the system at any $t>0$ and $\xi\in[0,\ell]$

$$\begin{cases} \partial_t P_j + V_j \partial_\xi P_j = -(\omega_1+\omega_2)P_j + \omega_2/\ell, & \text{for } j\in\{1,\dots,N\}, \\ \eta(V_i - V_{i+1}) = \displaystyle\int_0^\ell (P_i - P_{i+1})\partial_\xi \Delta W - k(\Delta_i - \Delta_{i+1}), & \text{for } i\in\{1,\dots,N-1\}, \\ \displaystyle\sum_{i=1}^N \dot\Delta_i(t) = 0 \text{ and } \dot X_n = 0. \end{cases} \tag{5.47}$$

Like in previous models, the equilibrium state is, for all $1\le i\le N-1$ and $1\le j\le N$

$$\begin{cases} V_i = 0, \\ X_i = 0, \\ P_j = P^0 = \dfrac{\omega_2}{\ell(\omega_1+\omega_2)}. \end{cases}$$

5.4.2 *Theoretical considerations*

In this situation we want to investigate the existence of a Hopf bifurcation in time, as it was done with the two-row model. To do so, we consider a linearized system arising from the N-row model (5.47), in order to have a general idea of the system's dynamics, as in (5.22). We expand in Fourier series $P_1,\dots,P_N$ and treat order by order the Fourier coefficients of the probabilities. For the first order coefficients, we obtain a $3N-1$ dimensional ODE system with unknowns:

$$p_j^{c,s}, \quad j=1,\dots,N, \qquad x_i,\ i=1,\dots,N-1.$$

We then perform some linear change of variables, similarly to (5.54), in order to write the Jacobian of the system as a block matrix. The first block is a $N+1$ diagonal matrix with real and negative entries $-a_0(\Omega)$. The rest of the linearized system is defined by the following equations

$$\begin{pmatrix} \dot q_i \\ \dot w_i \end{pmatrix} = \begin{pmatrix} -\frac{2\pi^2}{\ell\eta}Up_e - a_0 & -\frac{2\pi}{\ell\eta}kp_e \\ -\pi U/\eta & -k/\eta \end{pmatrix} \begin{pmatrix} q_i \\ w_i \end{pmatrix} \tag{5.48}$$

for $i = \{1, \dots, N-1\}$, where $p_e = a_1/(a_0\ell)$, $q_i = p_i^s - p_{i+1}^s$ for $i = 1, \dots, N-1$, and

$$\begin{pmatrix} w_1 \\ \vdots \\ w_{N-1} \end{pmatrix} = \begin{pmatrix} 2 & -1 & & & \\ -1 & 2 & -1 & & \\ & & \ddots & & \\ & & -1 & 2 & -1 \\ & & & -1 & 2 \end{pmatrix} \begin{pmatrix} x_1 \\ \vdots \\ x_{N-1} \end{pmatrix}. \tag{5.49}$$

It follows that the Jacobian has $N+1$ real and negative eigenvalues $-a_0(\Omega)$, and $N-1$ identical pairs of complex and conjugated ones $\mu_i(\Omega)$ for $i = 1, \dots, N-1$ which come from (5.48). We observe that the $\mu_i(\Omega) = \tau(\Omega) + i\omega(\Omega)$, with τ and ω defined as in Theorem 5.1.2 by equations (5.5) and (5.27). Then, if there exists $\Omega = \Omega_0$ such that $\tau(\Omega_0) = 0$ and $\tau'(\Omega_0) > 0$, then the eigenvalues cross the imaginary axis all at the same bifurcation parameter. Thus, there is a suggestion of a bifurcation in the dynamics at Ω_0, indicated by the linear part of the complete dynamical system. We won't investigate the theoretical aspects of this model further in this paper, as the Central Manifold Theorem used here was only of a 3D system. However, numerical simulations still suggest a potential pattern in the oscillations and hint that there is indeed a bifurcation.

5.4.3 *Numerical results*

In the following section, the N-layer model was tested for $N = 8$, to match the 8 motor rows of an axoneme with a bridge and nine microtubule doublets, as in Figure 5.1. We used the same parameter values as for the previous systems, as specified in Table 5.1. The initial conditions are such that $P_i(t = 0) = P^0$ for all i, and we destabilize the X_is randomly in $[-x_0, x_0]$, where $x^0 = 0.01\,nm$.

Using the same notations as before, i.e. $\Omega = (1 + \delta)\Omega_0$, we measure distance to bifurcation point Ω_0 using δ.

Figure 5.9(a) shows the absence of oscillations before instability ($\Omega = 0.9\Omega_0$), exactly as expected. Even though the system is put out of equilibrium by the initial conditions, since some tubule shifts are nonzero, they all quickly go back to zero and stop moving.

In Figure 5.9(b), we look at the system past the instability point, for $\Omega = 1.1\Omega_0$. Here, the system clearly reaches a steady-state oscillating regime after a short amount of time. All oscillations also remain centered in zero. As expected from the linear study in section 5.4.2, all Δ_is have the same amplitude and oscillation frequency, but their phase difference varies depending on initial conditions. In the particular case shown in Figure 5.9(b), one group of tubule pairs is synchronized with pair 7, and the other group with pair 8. In fact, when looking at all layers separately, one can see that odd layers (respectively even layers) oscillate in sync. The other possible outcome when running the simulation with random initial conditions was groups $\{1, 2, 7, 8\}$ and $\{3, 4, 5, 6\}$ oscillating together, as shown in Figure 5.9(c). This influence of the initial conditions is understandable since there is no external force taking the whole axonemal structure and filament into account, resulting in limited coupling between layers at this level. The layers thus tend to keep their original phase difference. The synchronization shown in

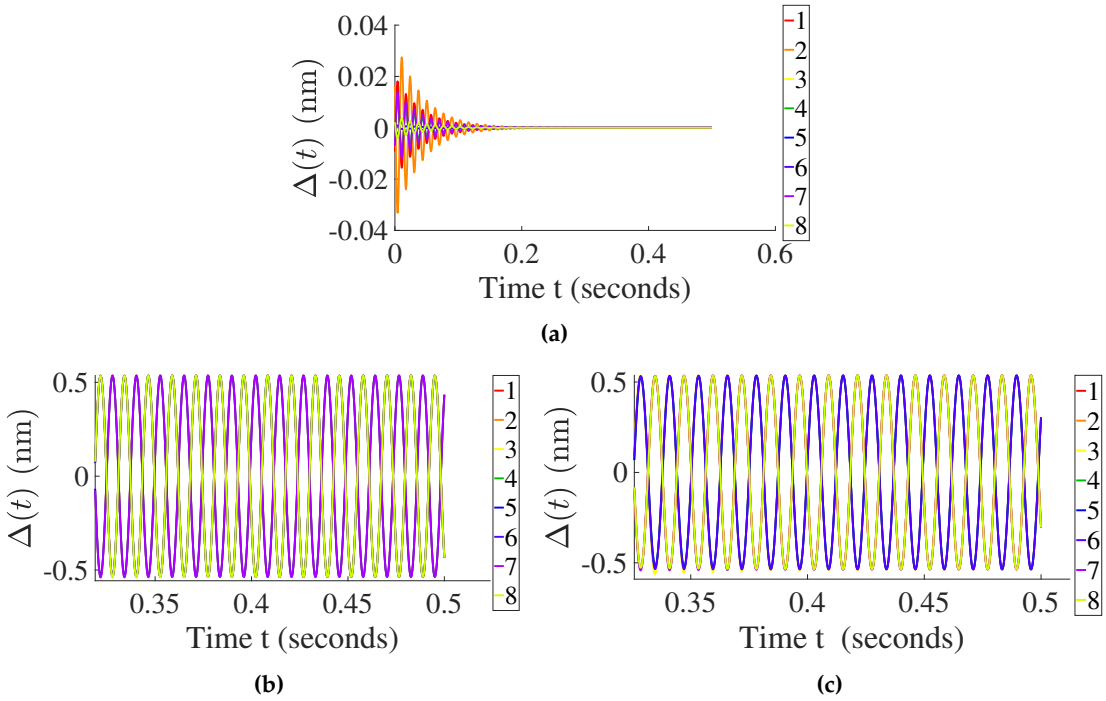

Figure 5.9. N-row model ($N = 8$). Relative tubule displacement (in nm) with respect to time (in seconds) for random initial conditions (a) before bifurcation point, for $\delta = -0.1$ ($\Omega = 0.9\Omega_0$) and (b) and (c) after bifurcation point , for $\delta = 0.1$ ($\Omega = 1.1\Omega_0$), for two iterations of random initial conditions.

Figure 5.9(c) was predicted by Howard et al. [51], and proves the importance of having a bridge around which the system alternates between positive and negative displacement. In the general case, since there is no theory behind the bifurcation of this system of $3N - 1$ equations, formally understanding the coupling between phase difference and initial conditions remains an open question.

A similar problem has recently been numerically studied in Kuramoto oscillators [18]. The Kuramoto model is fairly different from ours, by the fact that each oscillator has its own velocity, whereas all of our layers have one common velocity value. Our system of equations cannot thus be easily reduced to a Kuramoto model, but the behaviors of the two systems in terms of synchronization and dependence on initial conditions are very much alike. Some first steps, only modelling individual motors along a single row, have been presented in [32].

5.5 *Conclusion and outlook*

In this paper, we presented a new model for the axoneme, the cytoskeleton of cilia and flagella, focusing on the presence of spontaneous oscillations and potential synchronization of microtubule doublets under varying ATP concentrations. We called this model N-row model, where N represents the number of rows of motors walking between two microtubule doublets that are arranged in a circular configuration. Molecular motors are put into motion thanks to a chemical reaction involving ATP, thus inducing

microtubule sliding. This specific structural arrangement results in all microtubule doublets having a zero equilibrium position. The dynamic is governed by N transport equations, coming from a stochastic two-state model, and $N-1$ force balance equations, collectively forming a PDE system with $2N-1$ equations. We analyzed this model using both theoretical methods and numerical simulations. Our first studies focused on the $N=2$ configuration, revealing the existence and uniqueness of the displacement solution. Moreover, under sufficient chemical energy, the middle microtubule doublet exhibits spontaneous oscillations, corresponding to the existence of a super-critical Hopf-bifurcation in the dynamical system. Theoretical results are corroborated by numerical simulations. Subsequently, we conduct numerical analysis of the N-row model, focusing particularly on the case $N=8$. Here too, we observe that the system starts to oscillate once the ATP concentration surpasses a critical threshold. Remarkably, under appropriate initial conditions, we note the emergence of two out-of-phase groups among the microtubules, oscillating around the zero position with opposite shifting directions.

The first result on our model can be appreciated starting from the $N=2$ case. The cylindrical structure answers the problem of the axonemal symmetrization proposed in [29], previously solved by choosing symmetric transition rates. Instead, in of this paper, asymmetric transition rates have been used all along. More in general, even in the N-row model, we observed that the equilibrium displacement with null external force was zero, independently from the potentials and the transition rates. This means that the desired symmetry of the axoneme is always preserved: at equilibrium, with no external forces, each microtubule has the same role and there is no initial shifting in the structure. We underline that this is made possible in our model without imposing specific symmetry for the potentials.

From a more theoretical point of view, both Theorem 5.1.1 (well-posedness) and Theorem 5.1.2 (existence of a Hopf bifurcation) give a complete mathematical description on the two-row model. The same results can be proven for the one-row model as well, formalizing the work done in [47]. With the N-row model with fixed extremes, we set up a framework that is useful to gain insights on the microscopic structure of the axoneme. In particular, we comment on the specific case $N=8$, which is the closest representation of the real axoneme in terms of number of microtubule doublets. With the aid of the numerical scheme presented in the first section, we observed the onset of oscillations at a critical value of ATP. To perturb the system we tried several random initial conditions. We then noticed that imposing an opposite shift on each half of the model immediately led to robust and realistic patterns, potentially leading to planar flagellar beating patterns, as discussed in [71].

A natural extension to our work would be to take into account the presence of the central microtubule pair and, therefore, of the radial spokes coming from outer doublets towards the axonemal center. Moreover, this model can be thought of as a building block that, coupled with mechanics of an elastic flagellum, gives the feedback that generates

oscillatory patterns following in the footsteps of [30], [80] and [104] for the planar case and of [90] for the three dimensional case.

5.6 *Appendix: Center manifold computation*

In practice, equation (5.32) is a system of three equations. With the first equation below we aim to find the coefficients a_{1j}, with $j = 1, \dots, 6$

$$\begin{aligned}(2a_{11}y + a_{12}x + a_{13}\delta\Omega\,)\Bigg(&-a_0^0\Omega_0^{\alpha_0}y - \frac{\lambda}{\ell}\frac{a_1^0}{a_0^0}\Omega_0^{\alpha_1-\alpha_0}y - \frac{a_1^0}{a_0^0}\frac{\zeta}{\ell}\Omega_0^{\alpha_1-\alpha_0}x\\ &-a_0^0c(\alpha_0)\delta\Omega\ y - \frac{\lambda}{\ell}\frac{a_1^0}{a_0^0}c(\alpha_1-\alpha_0)\delta\Omega\ y - \frac{\zeta}{\ell}c(\alpha_1-\alpha_0)\delta\Omega\ x\\ &-\frac{b_1^0(r+s-2z)}{2a_1^0}(\zeta x+\lambda y)\Bigg)\\ &+(a_{12}y+2a_{14}x+a_{15}\delta\Omega\,)(-\frac{\beta\ell}{2\pi}y-\frac{\alpha\ell}{2\pi}x)\\ &+a_0^0\Omega_0^{\alpha_0}h_1 + a_0^0c(\alpha_0)\delta\Omega\ h_1\\ &-(\zeta x+\lambda y)\left(\frac{(a_1^0)^2(y+z)+(b_1^0)^2(-r+y+z)}{a_1^0b_1^0}\right)=0.\end{aligned}$$

Since we only need terms x, y and $\delta\Omega$ up to order two, we get rid of all the third order terms, getting

$$\begin{aligned}(2a_{11}y + a_{12}x + a_{13}\delta\Omega\,)\Bigg(&-a_0^0\Omega_0^{\alpha_0}y - \frac{\lambda}{\ell}\frac{a_1^0}{a_0^0}\Omega_0^{\alpha_1-\alpha_0}y - \frac{a_1^0}{a_0^0}\frac{\zeta}{\ell}\Omega_0^{\alpha_1-\alpha_0}x\Bigg)\\ &+(a_{12}y+2a_{14}x+a_{15}\delta\Omega\,)(-\frac{\beta\ell}{2\pi}y-\frac{\alpha\ell}{2\pi}x)\\ &+a_0^0\Omega_0^{\alpha_0}h_1-(\zeta x+\lambda y)\left(\frac{(a_1^0)^2y+(b_1^0)^2y}{a_1^0b_1^0}\right)=0.\end{aligned}\tag{5.50}$$

We then proceed by matching the terms x, y and $\delta\Omega$ with same order, and solve the resulting system of equations for a_{1j}. Notice we could have kept only the zero order term in the Taylor expansion, since all the higher order terms disappear during this approximation.

We do the same for the second and third equation, solving for the power series of h_2 and h_3.

For $i = 1, 2$, we obtain

$$\begin{aligned}a_{i1} &= -\frac{2\pi^2\lambda^2a_0^0\ell\left((a_1^0)^2+(b_1^0)^2\right)\Omega_0^{\alpha_1-\alpha_0}}{b_1^0\left(2\pi a_1^0\lambda\Omega_0^{\alpha_1-\alpha_0}+\zeta a_0^0\ell^2\right)\left(2\pi a_1^0\lambda\Omega_0^{\alpha_1-\alpha_0}+a_0^0\ell(\pi a_0^0\Omega_0^{\alpha_0}-\zeta\ell)\right)}\\ a_{i2} &= \frac{2\pi\zeta(a_0^0)^2\ell^2\left((a_1^0)^2+(b_1^0)^2\right)(\zeta l-\pi a_0^0\Omega_0^{\alpha_0})}{a_1^0b_1^0\left(2\pi a_1^0\lambda\Omega_0^{\alpha_1-\alpha_0}+\zeta a_0^0\ell^2\right)\left(2\pi a_1^0\lambda\Omega_0^{\alpha_1-\alpha_0}+a_0^0\ell(\pi a_0^0\Omega_0^{\alpha_0}-\zeta\ell)\right)}\\ a_{i3} &= 0,\quad a_{i4} = -\frac{2\pi^2\zeta^2a_0^0\ell\left((a_1^0)^2+(b_1^0)^2\right)\Omega_0^{\alpha_1-\alpha_0}}{b_1^0\left(2\pi a_1^0\lambda\Omega_0^{\alpha_1-\alpha_0}+\zeta a_0^0\ell^2\right)\left(2\pi a_1^0\lambda\Omega_0^{\alpha_1-\alpha_0}+a_0^0\ell(\pi a_0^0\Omega_0^{\alpha_0}-\zeta\ell)\right)}\\ a_{i5} &= 0,\quad a_{i6} = 0.\end{aligned}$$

For $i = 3$ we get

$$
\begin{aligned}
a_{31} &= -\frac{2\pi^2\lambda^2 a_0^0 b_1^0 \ell \Omega_0^{\alpha_1-\alpha_0}}{\left(2\pi a_1^0\lambda\Omega_0^{\alpha_1-\alpha_0}+\zeta a_0^0\ell^2\right)\left(2\pi a_1^0\lambda\Omega_0^{\alpha_1-\alpha_0}+a_0^0\ell(\pi a_0^0\Omega_0^{\alpha_0}-\zeta\ell)\right)}\\
a_{32} &= \frac{2\pi\zeta c^2 b_1^0\ell^2(\pi a_0^0\Omega_0^{\alpha_0}-\zeta\ell)}{a_1^0\left(2\pi a_1^0\lambda\Omega_0^{\alpha_1-\alpha_0}+\zeta a_0^0\ell^2\right)\left(2\pi a_1^0\lambda\Omega_0^{\alpha_1-\alpha_0}+c\ell(\pi a_0^0\Omega_0^{\alpha_0}-\zeta\ell)\right)}\\
a_{33} &= 0, \quad a_{34} = -\frac{2\pi^2\zeta^2 a_0^0 b_1^0\ell\Omega_0^{\alpha_1-\alpha_0}}{\left(2\pi a_1^0\lambda\Omega_0^{\alpha_1-\alpha_0}+\zeta a_0^0\ell^2\right)\left(2\pi a_1^0\lambda\Omega_0^{\alpha_1-\alpha_0}+a_0^0\ell(\pi a_0^0\Omega_0^{\alpha_0}-\zeta\ell)\right)}\\
a_{35} &= 0, \quad a_{36} = 0.
\end{aligned}
$$

5.7 *Appendix: Change of variables*

$$
\begin{cases}
\dot{p_1^c} = -a_0(\Omega)p_1^c + \left(\zeta x + \dfrac{\lambda}{2}(p_1^s - q_1^s)\right)p_1^s + \dfrac{a_1(\Omega)}{\ell},\\
\dot{p_1^s} = -a_0(\Omega)p_1^s - \left(\zeta x + \dfrac{\lambda}{2}(p_1^s - q_1^s)\right)p_1^c + \dfrac{b_1(\Omega)}{\ell},\\
\dot{q_1^c} = -a_0(\Omega)q_1^c - \left(\zeta x + \dfrac{\lambda}{2}(p_1^s - q_1^s)\right)q_1^s + \dfrac{a_1(\Omega)}{\ell},\\
\dot{q_1^s} = -a_0(\Omega)q_1^s + \left(\zeta x + \dfrac{\lambda}{2}(p_1^s - q_1^s)\right)q_1^c + \dfrac{b_1(\Omega)}{\ell},\\
\dot{x} = -\dfrac{\ell}{2\pi}\left(\zeta x + \dfrac{\lambda}{2}(p_1^s - q_1^s)\right),
\end{cases}
\tag{5.51}
$$

First step: shift to the origin

$$
\delta p_1^c = p_1^c - \frac{a_1}{a_0\ell}, \delta p_1^s = p_1^s - \frac{b_1}{a_0\ell}, \delta q_1^c = q_1^c - \frac{a_1}{a_0\ell}, \delta q_1^s = q_1^s - \frac{b_1}{a_0\ell}, \delta x = x, \tag{5.52}
$$

the system becomes

$$
\begin{cases}
\dot{\delta p_1^c} = -a_0\delta p_1^c + \left(\zeta x + \dfrac{\lambda}{2}(\delta p_1^s - \delta q_1^s)\right)(\delta p_1^s + \dfrac{b_1}{a_0\ell}),\\
\dot{\delta p_1^s} = -a_0\delta p_1^s - \left(\zeta x + \dfrac{\lambda}{2}(\delta p_1^s - \delta q_1^s)\right)(\delta p_1^c + \dfrac{a_1}{a_0\ell}),\\
\dot{\delta q_1^c} = -a_0\delta q_1^c - \left(\zeta x + \dfrac{\lambda}{2}(\delta p_1^s - \delta q_1^s)\right)(\delta q_1^s + \dfrac{b_1}{a_0\ell}),\\
\dot{\delta q_1^s} = -a_0\delta q_1^s + \left(\zeta x + \dfrac{\lambda}{2}(\delta p_1^s - \delta q_1^s)\right)(\delta q_1^c + \dfrac{a_1}{a_0\ell}),\\
\dot{\delta x} = -\dfrac{\ell}{2\pi}\left(\zeta\delta x + \dfrac{\lambda}{2}(\delta p_1^s - \delta q_1^s)\right),
\end{cases}
\tag{5.53}
$$

Second step: change of variable

$$
r = \tfrac{a_1}{b_1}\delta p_1^c + \delta p_1^s, \quad s = \tfrac{a_1}{b_1}\delta q_1^c + \delta q_1^s, \quad z = \tfrac{1}{2}(\delta p_1^s + \delta q_1^s), \quad y = \tfrac{1}{2}(\delta p_1^s - \delta q_1^s). \tag{5.54}
$$

In matrix form we have

$$\begin{pmatrix} r \\ s \\ z \\ y \end{pmatrix} = \begin{pmatrix} \frac{a_1}{b_1} & 1 & 0 & 0 \\ 0 & 0 & \frac{a_1}{b_1} & 1 \\ 0 & \frac{1}{2} & 0 & \frac{1}{2} \\ 0 & \frac{1}{2} & 0 & -\frac{1}{2} \end{pmatrix} \begin{pmatrix} \delta p_1^c \\ \delta p_1^s \\ \delta q_1^c \\ \delta q_1^s \end{pmatrix}, \tag{5.55}$$

and its inverse

$$\begin{pmatrix} \delta p_1^c \\ \delta p_1^s \\ \delta q_1^c \\ \delta q_1^s \end{pmatrix} = \begin{pmatrix} \frac{b_1}{a_1} & 0 & -\frac{b_1}{a_1} & -\frac{b_1}{a_1} \\ 0 & 0 & 1 & 1 \\ 0 & \frac{b_1}{a_1} & -\frac{b_1}{a_1} & \frac{b_1}{a_1} \\ 0 & 0 & 1 & -1 \end{pmatrix} \begin{pmatrix} r \\ s \\ z \\ y \end{pmatrix}. \tag{5.56}$$

$$\delta p_1^c = \tfrac{b_1}{a_1}(r - z - y), \quad \delta p_1^s = z + y, \quad \delta q_1^c = \tfrac{b_1}{a_1}(s - z + y), \quad \delta p_1^s = z - y. \tag{5.57}$$

Third step: sum equations to easily obtain the change of variable. For example, let us sum the first two equations in this way $\frac{a_1}{b_1}\delta p_1^c + \delta p_1^s$, we get

$$\dot{r} = -a_0 r + \big(\zeta x + \frac{\lambda}{2}(\delta p_1^s - \delta q_1^s)\big)\big(\frac{a_1}{b_1}\delta p_1^s - \delta p_1^c\big), \tag{5.58}$$

the same can be done for $\frac{a_1}{b_1}\delta q_1^c + \delta q_1^s$ and the system becomes

$$\begin{cases} \dot{r} = -a_0 r + \big(\zeta x + \frac{\lambda}{2}(\delta p_1^s - \delta q_1^s)\big)\big(\frac{a_1}{b_1}\delta p_1^s - \delta p_1^c\big), \\ \dot{s} = -a_0 s + \big(\zeta x + \frac{\lambda}{2}(\delta p_1^s - \delta q_1^s)\big)\big(-\frac{a_1}{b_1}\delta q_1^s + \delta q_1^c\big) \\ \dot{\delta p_1^s} = -a_0 \delta p_1^s - \big(\zeta x + \frac{\lambda}{2}(\delta p_1^s - \delta q_1^s)\big)(\delta p_1^c + \frac{a_1}{a_0 \ell}), \\ \dot{\delta q_1^s} = -a_0 \delta q_1^s + \big(\zeta x + \frac{\lambda}{2}(\delta p_1^s - \delta q_1^s)\big)(\delta q_1^c + \frac{a_1}{a_0 \ell}), \\ \dot{\delta x} = -\frac{\ell}{2\pi}\big(\zeta \delta x + \frac{\lambda}{2}(\delta p_1^s - \delta q_1^s)\big), \end{cases} \tag{5.59}$$

Now let us do the same with z and y, getting

$$\begin{cases} \dot{r} = -a_0 r + \big(\zeta x + \frac{\lambda}{2}(\delta p_1^s - \delta q_1^s)\big)\big(\frac{a_1}{b_1}\delta p_1^s - \delta p_1^c\big), \\ \dot{s} = -a_0 s + \big(\zeta x + \frac{\lambda}{2}(\delta p_1^s - \delta q_1^s)\big)\big(-\frac{a_1}{b_1}\delta q_1^s + \delta q_1^c\big) \\ \dot{z} = -a_0 \delta z - \big(\zeta x + \frac{\lambda}{2}(\delta p_1^s - \delta q_1^s)\big)\frac{1}{2}(-\delta p_1^c + \delta q_1^c), \\ \dot{y} = -a_0 \delta y - \big(\zeta x + \frac{\lambda}{2}(\delta p_1^s - \delta q_1^s)\big)\frac{1}{2}(\delta p_1^c + \delta q_1^c + 2\frac{a_1}{a_0 \ell}), \\ \dot{\delta x} = -\frac{\ell}{2\pi}\big(\zeta \delta x + \frac{\lambda}{2}(\delta p_1^s - \delta q_1^s)\big), \end{cases} \tag{5.60}$$

Fourth step: Complete with the change of variables and its inverse

$$\begin{cases} \dot{r} = -a_0 r + \big(\zeta x + \lambda y\big)\big(\frac{a_1}{b_1}(z+y) - \frac{b_1}{a_1}(r-z-y)\big), \\ \dot{s} = -a_0 s + \big(\zeta x + \lambda y\big)\big(-\frac{a_1}{b_1}(z-y) + \frac{b_1}{a_1}(s-z+y)\big) \\ \dot{z} = -a_0 \delta z - \big(\zeta x + \lambda y\big)\frac{1}{2}\big(\frac{b_1}{a_1}(-r+2y+s)\big), \\ \dot{y} = -a_0 \delta y - \big(\zeta x + \lambda y\big)\frac{1}{2}\big(\frac{b_1}{a_1}(r-2z+s) + 2\frac{a_1}{a_0 \ell}\big), \\ \dot{\delta x} = -\frac{\ell}{2\pi}\big(\zeta x + \lambda y\big)\,, \end{cases} \tag{5.61}$$

5.8 *Additional chemistry considerations*

The following section is an unpublished work investigating the accuracy of our models in terms of the chemical structure of the problem.

5.8.1 *Changing potentials*

In this section, we highlight the influence of our choice for the potentials W_i and transition rates ω_i. To do so, let us consider once again the one-row model. In Jülicher's first models [54], transitions rates are directly derived from chemical considerations, by looking at reaction speed in ATP hydrolysis. In the case of a two headed motor, the reactions can be written as:

$$\begin{cases} M_1 + ATP \underset{k_{-1}}{\overset{k_1}{\rightleftharpoons}} M_2 + ADP + P \\ M_1 + ADP + P \underset{k_{-2}}{\overset{k_2}{\rightleftharpoons}} M_2 + ATP \end{cases}$$

Which leads to the following reaction speed, where μ_i represents the chemical potential of a chemical component i

$$\begin{aligned} \frac{d[M_1]}{dt} &= -k_1[M_1] + k_{-1}[M_2] - k_2[M_1] + k_{-2}[M_2] \\ &= -\delta(x) e^{\frac{W_1(x)+\mu_{ATP}}{kT}}[M_1] + \delta(x) e^{\frac{W_2(x)+\mu_{ADP}+\mu_P}{kT}}[M_2] \\ &- \delta(x+\ell/2) e^{\frac{W_1(x)+\mu_{ADP}+\mu_P}{kT}}[M_1] + \delta(x+\ell/2) e^{\frac{W_2(x)+\mu_{ATP}}{kT}}[M_2] \\ &= -\omega_1[M_1] + \omega_2[M_2], \end{aligned}$$

where

$$\begin{cases} \omega_1(\xi) = [\delta(\xi) e^{\frac{\mu_{ATP}}{kT}} + \delta(\xi+\ell/2)] e^{W_1(\xi)/k_B T} \\ \omega_2(\xi) = [\delta(\xi) + \delta(\xi+\ell/2) e^{\frac{\mu_{ATP}}{kT}}] e^{W_2(\xi)/k_B T} \end{cases} \tag{5.62}$$

which directly and explicitly depend on both ATP and physical potentials. Here, δ is a Gaussian centered around the minimum of W_1, which helps favor transition at a specific

point in the periodicity cell. For W_1, we chose an arbitrary periodic potential that was highly nonlinear in ξ, so as to ensure it was not symmetric around $\ell/2$:

$$\begin{cases} W_1(\xi) = U\cos\big(2\pi/\ell(0.6\xi^3 + 0.4\xi)\big) \\ W_2(\xi) = W_1(\xi + \ell/2) \end{cases} \tag{5.63}$$

We also introduce, as previously done by [57], the local deviation from the chemical equilibrium of the system $\tilde{\Omega}(\xi)$, to model the dependence of the system on ATP concentration, depending on our parameter Ω:

$$\tilde{\Omega}(\xi) = \frac{\omega_1(\xi)}{\omega_2(\xi)} - \exp[(W_1(\xi) - W_2(\xi))/k_B T], \tag{5.64}$$

where k_B is the Boltzmann constant and T is the temperature of the system. We use the amplitude of this function, defining it as $\Omega := \sup_{\xi\in[0,\ell]} |\tilde{\Omega}(\xi)|$.

In practice, we will only work with ΔW and its usual assumptions, as well as the ones we originally made on ω_2 in the introduction. Moreover, using both our previous conditions and our chemical expressions (5.62), we can arrive to a series of equations on both Ω and α, which could eventually prove that there exists a solution that combines all our assumptions. The system is explained in further detail in 5.8.2.

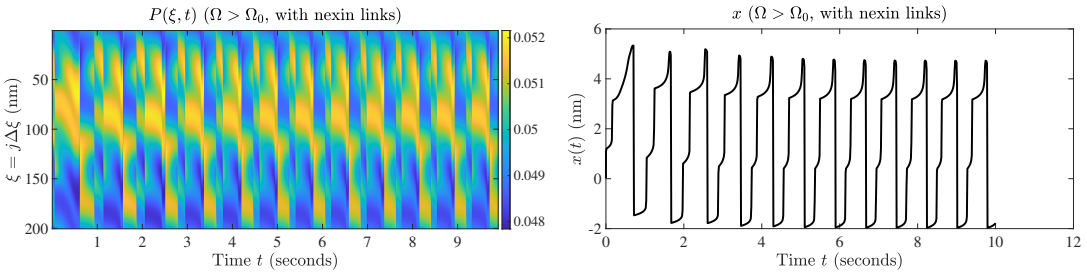

(a) **(b)**

Figure 5.10. One-row model for potentials (5.63) and transition rates (5.62). (a) Probability density and (b) displacement of the filament over time.

We can thus clearly observe in Figure 5.10 our choice has had an influence on the solution, as displacement x becomes highly nonlinear, and of much larger periodicity in time.

5.8.2 *Conditions on transition rates to match chemical reaction speeds*

The goal of this section is to match chemical transition rates (5.62) with our classic assumptions on our transition rates, i.e. uniformity (5.3) and expansion in Fourier series (5.4), knowing potentials W_1 and W_2.

Let us first denote by $F_i(\xi) = e^{\frac{W_i(\xi)}{kT}}$, and $\bar{\delta}(\xi) = \delta(\xi + \ell/2)$ for $\xi \in [0, \ell]$. Moreover, we also know that $\xi \mapsto \delta(\xi)$ is ℓ-periodic, from microtubule structure. We can then rewrite our local deviation from equilibrium (5.64) as:

$$\Omega\theta(\xi) = \frac{F_1}{F_1}\left(\frac{\delta(\xi)e^{\frac{\mu_{ATP}}{kT}} + \bar{\delta}(\xi)}{\delta(\xi) + \bar{\delta}(\xi)e^{\frac{\mu_{ATP}}{kT}}} - 1\right).$$

From this last equation, since for all $\xi \in [0, \ell]$, $|\theta(\xi)| \leq 1$, we can define:

$$\begin{aligned}\Omega &= \sup_{\xi\in[0,\ell]}\left|\frac{F_1}{F_1}\left(\frac{\delta(\xi)e^{\frac{\mu_{ATP}}{kT}} + \bar{\delta}(\xi)}{\delta(\xi) + \bar{\delta}(\xi)e^{\frac{\mu_{ATP}}{kT}}} - 1\right)\right|,\\ \theta(\xi) &= \frac{1}{\Omega}\frac{F_1}{F_1}\left(\frac{\delta(\xi)e^{\frac{\mu_{ATP}}{kT}} + \bar{\delta}(\xi)}{\delta(\xi) + \bar{\delta}(\xi)e^{\frac{\mu_{ATP}}{kT}}} - 1\right).\end{aligned}$$

Then, at fixed Ω, $\omega_1 + \omega_2 = a_0$ is constant. We can thus write:

$$0 = \partial_\xi a_0 = \partial_\xi\left[\delta(\xi)\left(e^{\frac{\mu_{ATP}}{kT}}F_1(\xi) + F_2(\xi)\right) + \bar{\delta}(\xi)\left(F_1(\xi) + e^{\frac{\mu_{ATP}}{kT}}F_2(\xi)\right)\right].$$

Expressing δ as a function of $\bar{\delta}$, W_1 and W_2, we finally arrive to the following differential equation:

$$\begin{cases}\delta' + G(\xi)\delta = F(\xi),\\ G(\xi) = \frac{F_1 e^{\frac{\mu_{ATP}}{kT}}W_1' + W_2'F_2}{kT\left(F_1 e^{\frac{\mu_{ATP}}{kT}} + F_2\right)},\\ F(\xi) = -\left(\frac{F_1}{F_2}\left(\frac{W_1'}{kT}\bar{\delta} + \bar{\delta}'\right) - \left(\frac{W_2'}{kT}\bar{\delta} + \bar{\delta}'\right)e^{\frac{\mu_{ATP}}{kT}}\right)H(\xi),\\ H(\xi) = \left(\frac{F_1}{F_2}e^{\frac{\mu_{ATP}}{kT}} + 1\right)^{-1}.\end{cases} \tag{5.65}$$

We can thus express δ in terms of G and F as:

$$\delta(\xi) = \left(A + \int_0^\xi F(s)e^{-\mathcal{G}(s)}ds\right)e^{\mathcal{G}(\xi)},$$

with $\mathcal{G} = -\int_0^\xi G(u)du$ and $A = \delta(0)e^{-\mathcal{G}(0)} \in \mathbb{R}$.

We can then observe that only F depends on $\bar{\delta}$. Moreover, by definition we also have that:

$$\bar{\delta}(\xi) = \left(A + \int_0^{\xi+\ell/2} F(s)e^{-\mathcal{G}(s)}ds\right)e^{\mathcal{G}(\xi+\ell/2)}.$$

By re-inserting the expression for δ in the equation, we finally obtain an integro-differential equation on $\bar{\delta}$ in both ξ and $\xi + \ell/2$, only depending on W_1 and W_2:

$$\bar{\delta}'(\xi)+G(\xi+\ell/2)\bar{\delta}(\xi)=H(\xi+\ell/2)\left[\frac{-F_1}{F_2}\left(\frac{W_1'}{kT}\bar{\delta}+\bar{\delta}'\right)-\left(\frac{W_2'}{kT}\bar{\delta}+\bar{\delta}'\right)e^{\frac{\mu_{ATP}}{kT}}\right](\xi+\ell/2).$$

This equation is not studied in more detail here. However, tools from Floquet theory might lead to additionnal results.

Essayons de converser sans nous exalter, puisque nous sommes incapables de nous taire.

Samuel Beckett, En Attendant Godot

6 *Conclusion et perspectives*

Au cours de cette thèse, nous avons modélisé des micro-nageurs dotés de bras ou de flagelles, à différentes échelles. Nous nous sommes à la fois intéressés à des considérations purement mathématiques, et nous avons fait de la modélisation directement basée sur la structure biophysique d'un flagelle.

Dans les deux premiers chapitres, nous avons présenté des modèles mathématiques de nageurs à un bras actif et plusieurs bras passifs, qui vivent en une dimension. Nous avons réussi à rendre un de ces modèles à un seul bras actifs contrôlable, et nous avons étudié la propagation d'une onde le long de la queue du nageur avec N ressorts, ainsi que son modèle limite quand N tend vers l'infini. Ensuite, dans le troisième chapitre, nous avons pu prouver la convergence du modèle du N-link vers les équations d'un filament élastohydrodynamique passif, et son caractère bien posé, constitutant ainsi un premier pas vers la justification de ce modèle discret d'un point de vue à la fois physique et mathématique. Cela apporte un outil robuste et simple à mettre en œuvre du point de vue des simulations numériques. Enfin, dans le dernier chapitre, on a modélisé la structure de l'axonème, qui garantit la présence d'activation le long d'un flagelle, et crée le battement caractéristique que l'on observe en biologie.

Les perspectives liées à l'ensemble de ces chapitres sont multiples, mais suivent toutes une même ligne directrice, à savoir *modéliser de manière complète un spermatozoïde*, voire *construire un micro-robot flagellé pour des applications médicales*. On pourra ainsi s'intéresser à:

- **Introduire de l'activation dans les modèles de nageurs discrets.** Une première idée serait d'inclure une forme d'activation dans les ressorts passifs du nageur à N ressorts, de manière à avoir une composante active qui entretiendrait le mouvement et propagerait l'onde de long de la queue du nageur plutôt que de la laisser s'atténuer. Tout en se basant sur des valeurs de forces liées aux moteurs moléculaires comme présenté dans le chapitre 5, on pourrait ajouter un élément actif défini comme la partie *odd-elastic* du ressort, comme introduit par K. Ishimoto, C. Moreau, et K. Yasuda [53]. En d'autres termes, la raideur k du ressort deviendrait une matrice, dans laquelle les termes diagonaux resteraient sa raideur classique k, et les termes anti-diagonaux auraient une valeur non nulle représentant le terme d'activation. Cette première étape permettrait d'avoir de bonnes bases pour insérer ensuite une forme d'activation dans un modèle directement issu de la physique. Pour ce qui est du N-link, l'ajout d'une force d'activation pose de nouveau des questions du côté du caractère bien posé du modèle, ainsi que de sa convergence vers les équations continues. En effet, la preuve était basée sur une conservation de l'énergie dans le système, qui devient une dissipation d'énergie lorsqu'on y apporte une force d'activation. Mettre cette force sous forme *odd-elastic* uniquement dans les ressorts à la jointure entre deux segments pourrait donc peut être permettre

d'adapter les preuves précédentes.

◇ **Prendre en compte une tête à une extrémité du filament ou du N-link, comme dans les nageurs biologiques ou le micro-nageur de S. Régnier [37].** L'ajout d'une tête à l'extrémité proximale du N-link soulève de nombreuses interrogations. Tout d'abord, comment modéliser le *corps basal*, qui représente le lien entre le filament et la tête ? En dehors de l'influence sur les conditions au bord proximal, déjà étudiées, quel serait l'impact de la présence d'une tête dans les potentielles modifications du battement du flagelle ? De nouveau, comme dans le point précédent, cette tête change également le bilan des forces et des moments du système complet. Il faudrait donc à la fois de nouveau s'intéresser à la pertinence de l'utilisation d'un modèle N-link doté d'une tête pour représenter un filament continu, et étudier les équations discrètes et continues des points de vue théorique et numérique. Enfin, du point de vue des micro-robots, cette tête pourrait également être magnétique, afin de guider le nageur grâce à un champ électromagnétique, ce qui rajouterait un aspect de théorie du contrôle au problème.

◇ **Raffiner et étendre le modèle d'axonème à N couches.** La structure interne des flagelles est beaucoup plus complexe que ce que nous avons traité dans cette thèse. Des filaments, appelés *rayons* (ou, en anglais, *radial spokes*) dans la littérature, ainsi que les deux tubules centrales de l'axonème, pourraient avoir une importance cruciale dans le mécanisme de déformation. Pour traiter ce genre de dispositif, une première idée serait de compléter le modèle présenté en chapitre 5 en y incluant les composantes mentionnées ci-dessus, qui n'ont pas été prises en considération ici. Le premier enjeu, avant d'étudier un système d'équations final, serait de comprendre comment modéliser ces composantes de l'axonème. Par exemple, représenter les rayons comme des ressorts s'attachant à chaque paire de tubules favorise les derniers modes d'oscillation de l'axonème dans le modèle à N couches, et ne fournit donc pas un modèle pertinent. On pourrait également étudier d'un point de vue théorique et numérique l'influence des rayons et tubules centrales sur le comportement du système, et le comparer aux études expérimentales telles que celle d'E. F. Smith et P. Yang [92], qui observent notamment des changements dans l'amplitude de battement du flagelle. Le second aspect serait de modéliser l'axonème dans toute sa longueur, et non plus seulement dans une cellule de périodicité de taille $\ell > 0$. Il faudrait donc réussir à relier plusieurs cellules de notre modèle N couches côte à côte, en prenant en compte les diverses forces résultant de potentielles interactions entre les cellules de périodicité.

◇ **Coupler le modèle d'axonème et le N-link dans une simulation fluide-structure multi-échelle.** Après avoir étudié les trois points précédents, on aura d'une part, un modèle d'axonème pour tout un flagelle, et d'autre part, un modèle discret et robuste de filament attaché avec une tête, dont le caractère bien posé et la convergence seront garantis pour une bonne définition de l'activation. On

voudrait ensuite réussir à intégrer tout le modèle d'axonème dans le nageur N-link avec une tête, plutôt que d'utiliser une valeur de force approximative. Il faudra donc réussir à inclure, à N fixé, le bon nombre de cellules de périodicité dans un segment du N-link, et coupler les deux systèmes d'équations. D'un point de vue des simulations, on voudra s'assurer d'utiliser un N assez grand pour garantir une précision suffisante de nos résultats, et notamment trouver une méthode d'estimation de l'erreur adaptée. On pourra par exemple comparer le comportement du nageur à celui reproduit par E. A. Gaffney, K. Ishimoto et B. J. Walker [43] à partir de données expérimentales.

Bibliography

[1] F. Alouges, I. Anello, A. DeSimone, A. Lefebvre-Lepot, and J. Levillain, "Some mathematical models for flagellar activation mechanisms," 2024. arXiv: 2409.03506 [math.NA] (cit. on p. 93).

[2] F. Alouges, A. DeSimone, L. Giraldi, and M. Zoppello, "Self-propulsion of slender micro-swimmers by curvature control: N-link swimmers," *Int. J. of Non-Linear Mech.*, 2013 (cit. on pp. 21, 27, 69).

[3] F. Alouges, A. DeSimone, L. Giraldi, and M. Zoppello, "Can magnetic multilayers propel artificial microswimmers mimicking sperm cells?" *Soft Robotics*, vol. 2, no. 3, pp. 117–128, 2015 (cit. on p. 66).

[4] F. Alouges, A. DeSimone, and L. Heltai, "Numerical strategies for stroke optimization of axisymmetric microswimmers," *Mathematical Models and Methods in Applied Sciences*, vol. 21, no. 2, pp. 361–387, 2011 (cit. on p. 43).

[5] F. Alouges, A. DeSimone, and A. Lefebvre, "Optimal Strokes for Low Reynolds Number Swimmers: An Example," *Journal of Nonlinear Science*, vol. 18, no. 3, pp. 277–302, 2008 (cit. on pp. 31, 43, 59).

[6] F. Alouges, A. DeSimone, and A. Lefebvre, "Optimal strokes for axisymmetric microswimmers," *Eur. Phys. J. E 28, 279–284*, 2009 (cit. on pp. 21, 43).

[7] F. Alouges, A. DeSimone, A. Lefebvre-Lepot, and B. Merlet, "Optimally swimming stokesian robots," *Discrete & Continuous Dynamical Systems - B*, vol. 18, no. 5, pp. 1189–1215, 2013 (cit. on p. 43).

[8] F. Alouges and G. D. Fratta, "Parking 3-sphere swimmer I. Energy minimizing strokes," *Discrete and Continuous Dynamical Systems - B*, vol. 23, no. 4, pp. 1797–1817, 2018 (cit. on p. 41).

[9] F. Alouges and G. D. Fratta, "Parking 3-sphere swimmer: II. The long-arm asymptotic regime.," *Eur. Phys. J. E*, vol. 43, 2020 (cit. on p. 41).

[10] F. Alouges, L. Giraldi, Y. Or, and O. Wiezel, "Energy-optimal strokes for multi-link microswimmers: Purcell's loops and Taylor's waves reconciled," *New Journal of Physics*, vol. 21, no. 4, p. 043 050, 2019 (cit. on pp. 31, 43).

[11] F. Alouges, A. Lefebvre-Lepot, and J. Levillain, "A limiting model for a low reynolds number swimmer with N passive elastic arms," *Mathematics in Engineering*, vol. 5, no. 5, pp. 1–20, 2023 (cit. on pp. 26, 43).

[12] F. Alouges, A. Lefebvre-Lepot, and P. Weder, "Optimal strokes for the 4-sphere swimmer at low Reynolds number in the regime of small deformations," *MathematicS In Action*, vol. 11, pp. 167–192, 2022 (cit. on p. 41).

[13] S. Antman, *Nonlinear Problems of Elasticity* (Applied Mathematical Sciences). New York: Springer-Verlag, 2005, vol. 107 (cit. on pp. 65–67).

[14] J.-P. Aubin, "Un théoreme de compacité," *CR Acad. Sci. Paris*, vol. 256, no. 24, pp. 5042–5044, 1963 (cit. on pp. 28, 67, 80).

[15] J. E. Avron, O. Gat, and O. Kenneth, "Optimal swimming at low reynolds numbers," *Phys. Rev. Lett.*, vol. 93, p. 186 001, 2004 (cit. on pp. 31, 59).

[16] J. E. Avron, O. Kenneth, and D. H. Oaknin, "Pushmepullyou: An efficient micro-swimmer," *New Journal of Physics*, vol. 7, p. 234, 2005 (cit. on pp. 21, 31, 59).

[17] G. Batchelor, *An Introduction to Fluid Dynamics*. Cambridge University Press, 2012 (cit. on p. 33).

[18] A. Bayani, S. Jafari, H. Azarnoush, F. Nazarimehr, S. Boccaletti, and M. Perc, "Explosive synchronization dependence on initial conditions: The minimal kuramoto model," *Chaos, Solitons & Fractals*, vol. 169, p. 113 243, 2023 (cit. on p. 118).

[19] P. V. Bayly and S. K. Dutcher, "Steady dynein forces induce flutter instability and propagating waves in mathematical models of flagella," *Journal of The Royal Society Interface*, vol. 13, no. 123, p. 20 160 523, 2016 (cit. on p. 94).

[20] L. E. Becker, S. A. Koehler, and H. A. Stone, "On self-propulsion of micro-machines at low reynolds number: Purcell's three-link swimmer," *Journal of Fluid Mechanics*, vol. 490, pp. 15–35, 2003 (cit. on p. 31).

[21] K. Bente, A. Codutti, F. Bachmann, and D. Faivre, "Biohybrid and bioinspired magnetic microswimmers," *Small*, vol. 14, no. 29, p. 1 704 374, 2018 (cit. on p. 65).

[22] H. C. Berg and R. A. Anderson, "Bacteria swim by rotating their flagellar filaments," *Nature*, vol. 245, no. 5425, pp. 380–382, Oct. 1973, ISSN: 1476-4687 (cit. on p. 91).

[23] F. Boyer and P. Fabrie, *Mathematical Tools for the Study of the Incompressible Navier-Stokes Equations and Related Models*. Springer Science & Business Media, 2012, vol. 183 (cit. on pp. 28, 80).

[24] J. F. Brady and G. Bossis, "Stokesian dynamics," *Annual Review of Fluid Mechanics*, vol. 20, no. Volume 20, 1988, pp. 111–157, 1988 (cit. on p. 22).

[25] C. P. Broedersz and F. C. MacKintosh, "Modeling semiflexible polymer networks," *Reviews of Modern Physics*, vol. 86, no. 3, p. 995, 2014 (cit. on p. 65).

[26] C. J. Brokaw, "Flagellar Movement: A Sliding Filament Model: An explanation is suggested for the spontaneous propagation of bending waves by flagella.," *Science*, vol. 178, no. 4060, pp. 455–462, 1972 (cit. on p. 94).

[27] C. J. Brokaw, "Bending patterns of ATP-reactivated sea urchin sperm flagella following high salt extraction for removal of outer dynein arms," *Cell Motility and the Cytoskeleton*, vol. 42, no. 2, pp. 125–133, 1999 (cit. on p. 94).

[28] C. J. Brokaw, "Computer simulation of flagellar movement X: Doublet pair splitting and bend propagation modeled using stochastic dynein kinetics," *Cytoskeleton*, vol. 71, no. 4, pp. 273–284, 2014 (cit. on p. 94).

[29] S. Camalet and F. Jülicher, "Generic aspects of axonemal beating," *New Journal of Physics*, vol. 2, no. 1, p. 324, 2000 (cit. on pp. 94, 96, 97, 99, 100, 111, 119).

[30] J. Cass and H. Bloomfield-Gadêlha, "The reaction-diffusion basis of animated patterns in eukaryotic flagella," *Nature Communications*, vol. 14, Sep. 2023 (cit. on p. 120).

[31] S. Childress, *Mechanics of Swimming and Flying*, C. S. in Mathematical Biology, Ed. Cambridge University Press, 1981 (cit. on pp. 31, 43).

[32] G. Costantini and A. Puglisi, "Thermodynamic precision of a chain of motors: The difference between phase and noise correlation," *Journal of Statistical Mechanics: Theory and Experiment*, vol. 2024, no. 2, p. 024 003, Feb. 2024 (cit. on p. 118).

[33] A. DeSimone, L. Heltai, F. Alouges, and A. Lefebvre-Lepot, "Computing optimal Strokes for Low Reynolds Number Swimmers," *Natural Locomotion in Fluids and on Surfaces, The IMA Volumes in Mathematics and its Applications*, pp. 177–184, 2012 (cit. on p. 43).

[34] R. Dreyfus, J. Baudry, M. L. Roper, M. Fermigier, H. A. Stone, and J. Bibette, "Microscopic artificial swimmers," *Nature*, vol. 437, pp. 862–865, 2005 (cit. on p. 23).

[35] R. Dreyfus, J. Baudry, and H. Stone, "Purcell's "rotator": Mechanical rotation at low Reynolds number," *Physics of Condensed Matter*, pp. 161–164, 2005 (cit. on pp. 20, 31, 43, 59).

[36] O. Du Roure, A. Lindner, E. N. Nazockdast, and M. J. Shelley, "Dynamics of flexible fibers in viscous flows and fluids," *Annual Review of Fluid Mechanics*, vol. 51, pp. 539–572, 2019 (cit. on pp. 65, 91).

[37] Y. El Alaoui-Faris, J.-B. Pomet, S. Régnier, and L. Giraldi, "Optimal actuation of flagellar magnetic micro-swimmers," *Phys. Rev. E*, vol. 101, p. 042 604, 2020 (cit. on pp. 23, 130).

[38] J. Elgeti and G. Gompper, "Microswimmers near surfaces," *The European Physical Journal Special Topics*, vol. 225, pp. 2333–2352, 2016 (cit. on p. 66).

[39] L. C. Evans, *Partial Differential Equations, Second edition*. American Mathematical Society, 1998, vol. 19 (cit. on p. 80).

[40] P. Fuchter and H. Bloomfield-Gadêlha, "The three-dimensional coarse-graining formulation of interacting elastohydrodynamic filaments and multi-body micro-hydrodynamics," *Journal of the Royal Society Interface*, vol. 20, no. 202, p. 20 230 021, 2023 (cit. on p. 91).

[41] H. Gadêlha, E. Gaffney, D. Smith, and J. Kirkman-Brown, "Nonlinear instability in flagellar dynamics: A novel modulation mechanism in sperm migration?" *Journal of The Royal Society Interface*, vol. 7, no. 53, pp. 1689–1697, 2010 (cit. on p. 66).

[42] E. A. Gaffney, H. Gadêlha, D. Smith, J. Blake, and J. Kirkman-Brown, "Mammalian sperm motility: Observation and theory," *Annual Review of Fluid Mechanics*, vol. 43, no. 1, pp. 501–528, 2011 (cit. on p. 93).

[43] E. A. Gaffney, K. Ishimoto, and B. J. Walker, "Modelling motility: The mathematics of spermatozoa," *Frontiers in Cell and Developmental Biology*, vol. 9, 2021 (cit. on pp. 93, 131).

[44] L. Giraldi, P. Martinon, and M. Zoppello, "Controllability and optimal strokes for N-link microswimmer," in *52nd IEEE Conference on Decision and Control*, ISSN: 0191-2216, Dec. 2013, pp. 3870–3875 (cit. on p. 27).

[45] R. Golestanian and A. Ajdari, "Analytic results for the three-sphere swimmer at low reynolds number," *Phys. Rev. E*, vol. 77, p. 036 308, 3 Mar. 2008 (cit. on p. 22).

[46] J. Gray and G. J. Hancock, "The propulsion of sea-urchin spermatozoa," *Journal of Experimental Biology*, vol. 32, 4 1955 (cit. on pp. 21, 65, 93).

[47] T. Guérin, J. Prost, and J.-F. Joanny, "Dynamical behavior of molecular motor assemblies in the rigid and crossbridge models," *The European Physical Journal E*, vol. 34, pp. 1–21, 2011 (cit. on pp. 97, 100, 111, 119).

[48] J. Happel and H. Brenner, *Low Reynolds Number Hydrodynamics: With Special Applications to Particulate Media* (Prentice-Hall international series in the physical and chemical engineering sciences). Prentice-Hall, 1965, ISBN: 9789024728770 (cit. on p. 22).

[49] M. Hines and J. Blum, "Bend propagation in flagella. i. derivation of equations of motion and their simulation," *Biophysical Journal*, vol. 23, no. 1, pp. 41–57, 1978 (cit. on p. 66).

[50] J. Howard, "Mechanical signaling in networks of motor and cytoskeletal proteins," *Annual Review of Biophysics*, vol. 38, no. 1, pp. 217–234, 2009 (cit. on p. 95).

[51] J. Howard, A. Chasteen, X. Ouyang, V. F. Geyer, and P. Sartori, "Predicting the locations of force-generating dyneins in beating cilia and flagella," *Frontiers in Cell and Developmental Biology*, vol. 10, 2022 (cit. on p. 118).

[52] T. Hu and P. V. Bayly, "Finite element models of flagella with sliding radial spokes and interdoublet links exhibit propagating waves under steady dynein loading," *Cytoskeleton*, vol. 75, no. 5, pp. 185–200, 2018 (cit. on p. 94).

[53] K. Ishimoto, C. Moreau, and K. Yasuda, "Self-organized swimming with odd elasticity," *Phys. Rev. E*, vol. 105, p. 064 603, 6 Jun. 2022 (cit. on p. 129).

[54] F. Jülicher, "Force and motion generation of molecular motors: A generic description," in *Lecture Notes in Physics, Berlin Springer Verlag*, S. C. Müller, J. Parisi, and W. Zimmermann, Eds., vol. 532-532, 1999, p. 46 (cit. on pp. 94, 123).

[55] F. Jülicher, A. Ajdari, and J. Prost, "Modeling molecular motors," *Rev. Mod. Phys.*, vol. 69, pp. 1269–1282, 4 1997 (cit. on pp. 28, 94, 95).

[56] F. Jülicher and J. Prost, "Cooperative molecular motors," *Phys. Rev. Lett.*, vol. 75, pp. 2618–2621, 13 1995 (cit. on pp. 28, 94, 95).

[57] F. Jülicher and J. Prost, "Spontaneous oscillations of collective molecular motors," *Phys. Rev. Lett.*, vol. 78, pp. 4510–4513, 23 1997 (cit. on pp. 24, 28, 94, 95, 124).

[58] F. Jülicher and J. Prost, "Molecular Motors: From Individual to Collective Behavior," *Progress of Theoretical Physics Supplement*, vol. 130, pp. 9–16, 1998 (cit. on pp. 28, 94).

[59] E. Lauga, *The Fluid Dynamics of Cell Motility* (Cambridge Texts in Applied Mathematics). Cambridge: Cambridge University Press, 2020 (cit. on pp. 65, 66).

[60] E. Lauga and T. R. Powers, "The hydrodynamics of swimming microorganisms," *Reports on Progress in Physics*, no. 9, p. 096 601, 2009 (cit. on pp. 21, 31, 43).

[61] A. Lefebvre, F. Alouges, and A. DeSimone, "Biological fluid dynamics: Swimming at low reynolds numbers," in *Encyclopedia of Complexity and System Science, Springer Verlag*, 2009 (cit. on p. 20).

[62] S. Leibler and D. A. Huse, "Porters versus rowers: A unified stochastic model of motor proteins," *The Journal of cell biology*, vol. 121, pp. 1357–1368, 6 1993 (cit. on p. 94).

[63] J. Levillain, F. Alouges, A. DeSimone, A. Choudary, S. Nambiar, and I. Bochert, "Bi-directional low reynolds number swimmers with passive elastic arms," *To be published in ESAIM:ProcS, CJC-MA 2023*, 2024 (cit. on pp. 25, 31).

[64] M. J. Lighthill, "On the squirming motion of nearly spherical deformable bodies through liquids at very small reynolds numbers," *Communications on Pure and Applied Mathematics*, vol. 5, no. 2, pp. 109–118, 1952 (cit. on p. 21).

[65] C. B. Lindemann, "A "geometric clutch" hypothesis to explain oscillations of the axoneme of cilia and flagella," *Journal of Theoretical Biology*, vol. 168, no. 2, pp. 175–189, 1994 (cit. on p. 95).

[66] C. B. Lindemann, "Testing the geometric clutch hypothesis," *Biology of the Cell*, vol. 96, no. 9, pp. 681–690, 2004 (cit. on p. 95).

[67] C. B. Lindemann, "The geometric clutch as a working hypothesis for future research on cilia and flagella," *Annals of the New York Academy of Sciences*, vol. 1101, no. 1, pp. 477–493, 2007 (cit. on p. 95).

[68] C. B. Lindemann, "Chapter one: Experimental evidence for the geometric clutch hypothesis," in *Current Topics in Developmental Biology*, ser. Forces and Tension in Development, M. Labouesse, Ed., vol. 95, Academic Press, 2011, pp. 1–31 (cit. on p. 95).

[69] C. B. Lindemann and K. S. Kanous, "Geometric clutch hypothesis of axonemal function: Key issues and testable predictions," *Cell Motility and the Cytoskeleton*, vol. 31, no. 1, pp. 1–8, 1995 (cit. on p. 95).

[70] C. B. Lindemann and K. A. Lesich, "The geometric clutch at 20: Stripping gears or gaining traction?" *Reproduction*, vol. 150, R45–R53, 2015 (cit. on p. 95).

[71] C. B. Lindemann and K. A. Lesich, "The many modes of flagellar and ciliary beating: Insights from a physical analysis," *Cytoskeleton*, vol. 78, no. 2, pp. 36–51, 2021 (cit. on pp. 95, 119).

[72] A. Lindner and M. Shelley, "Elastic Fibers in Flows," in *Fluid–Structure Interactions in Low-Reynolds-Number Flows*, The Royal Society of Chemistry, Nov. 2015, ISBN: 978-1-84973-813-2 (cit. on p. 65).

[73] K. E. Machin, "Wave Propagation along Flagella," *Journal of Experimental Biology*, no. 4, pp. 786–806, 1958 (cit. on pp. 24, 27, 62, 93).

[74] A. Montino and A. DeSimone, "Three-sphere low-Reynolds-number swimmer with a passive elastic arm," *The European Physical Journal E*, pp. 1–10, 2015 (cit. on pp. 22, 23, 25, 27, 31–35, 39, 41, 44, 45, 56, 59, 61).

[75] C. Moreau, L. Giraldi, and H. Gadêlha, "The asymptotic coarse-graining formulation of slender-rods, bio-filaments and flagella," *Journal of the Royal Society Interface*, vol. 15, no. 144, p. 20 180 235, 2018 (cit. on pp. 27, 66, 69).

[76] Y. Mori and L. Ohm, "Well-posedness and applications of classical elastohydrodynamics for a swimming filament," en, *Nonlinearity*, vol. 36, no. 3, pp. 1799–1839, Mar. 2023 (cit. on pp. 66, 91).

[77] A. Najafi and R. Golestanian, "Simple swimmer at low Reynolds number: Three linked spheres," *Phys. Rev. E*, no. 6, p. 062 901, 2004 (cit. on pp. 20, 22, 25, 31, 32, 43, 45).

[78] E. Nazockdast, A. Rahimian, D. Zorin, and M. Shelley, "A fast platform for simulating semi-flexible fiber suspensions applied to cell mechanics," *Journal of Computational Physics*, vol. 329, pp. 173–209, 2017 (cit. on p. 65).

[79] L. Ohm, "Well-posedness of a viscoelastic resistive force theory and applications to swimming," *arXiv preprint arXiv:2209.14160*, 2022 (cit. on p. 90).

[80] D. Oriola, H. Gadêlha, and J. Casademunt, "Nonlinear amplitude dynamics in flagellar beating," *Royal Society open science*, vol. 4, no. 3, p. 160 698, 2017 (cit. on p. 120).

[81] C. Oseen, *Hydrodynamik* (Mahtematik in Monographien und Lehrbüchern). Akademische Verlagsgesellschaft, 1927 (cit. on p. 22).

[82] N. Oulmas A. Andreff and S. Régnier, "3D closed-loop swimming at low reynolds numbers," *Int. J. Robotics Res.*, vol. 37, 11 2018 (cit. on p. 23).

[83] E. Passov and Y. Or, "Dynamics of Purcell's three-link microswimmer with a passive elastic tail," *The European Physical Journal E*, no. 8, p. 78, 2012 (cit. on pp. 22, 23, 31, 32, 44).

[84] C. Pauer, O. Du Roure, J. Heuvingh, T. Liedl, and J. Tavacoli, "Programmable design and performance of modular magnetic microswimmers," *Advanced Materials*, vol. 33, no. 16, p. 2 006 237, 2021 (cit. on p. 66).

[85] O. Pironneau and D. F. Katz, "Optimal swimming of flagellated micro-organisms," *Journal of Fluid Mechanics*, vol. 66, no. 2, pp. 391–415, 1974 (cit. on p. 94).

[86] J. Prost, J.-F. Chauwin, L. Peliti, and A. Ajdari, "Asymmetric pumping of particles," *Phys. Rev. Lett.*, vol. 72, pp. 2652–2655, 16 1994 (cit. on pp. 28, 94).

[87] E. M. Purcell, "Life at low Reynolds Number," *American Journal of Physics*, pp. 3–11, 1977 (cit. on pp. 20, 31, 41, 43, 61, 93).

[88] P. Raviart and J.-M. Thomas, *Introduction à l'analyse numérique des équations aux dérivées partielles*. Masson, 1988 (cit. on pp. 27, 49).

[89] P. Sartori, V. F. Geyer, A. Scholich, F. Jülicher, and J. Howard, "Dynamic curvature regulation accounts for the symmetric and asymmetric beats of *Chlamydomonas* flagella," *eLife*, vol. 5, R. E. Goldstein, Ed., e13258, 2016 (cit. on pp. 94, 96).

[90] P. Sartori, V. F. Geyer, J. Howard, and F. Jülicher, "Curvature regulation of the ciliary beat through axonemal twist," *Phys. Rev. E*, vol. 94, p. 042 426, 4 Oct. 2016 (cit. on p. 120).

[91] P. Satir and T. Matsuoka, "Splitting the ciliary axoneme: Implications for a "switch-point" model of dynein arm activity in ciliary motion," *Cell Motility*, vol. 14, no. 3, pp. 345–358, 1989 (cit. on p. 96).

[92] E. F. Smith and P. Yang, "The radial spokes and central apparatus: Mechano-chemical transducers that regulate flagellar motility," *Cell Motility*, vol. 57, no. 1, pp. 8–17, Nov. 2003 (cit. on p. 130).

[93] S. E. Spagnolie and P. T. Underhill, "Swimming in complex fluids," *Annual Review of Condensed Matter Physics*, vol. 14, pp. 381–415, 2023 (cit. on pp. 66, 90).

[94] J. M. Squire, "Muscle contraction: Sliding filament history, sarcomere dynamics and the two huxleys," *Global cardiology science and practice*, vol. 2, 2016 (cit. on p. 94).

[95] H. A. Stone and A. D. T. Samuel, "Propulsion of microorganisms by surface distortions," *Phys. Rev. Lett.*, vol. 77, pp. 4102–4104, 19 Nov. 1996 (cit. on p. 31).

[96] K. E. Summers and I. R. Gibbons, "Adenosine triphosphate-induced sliding of tubules in trypsin-treated flagella of sea-urchin sperm," *Proc. Nat. Acad. Sci. USA*, vol. 68, no. 12, pp. 3092–3096, 1971 (cit. on p. 94).

[97] D. Tam and A. E. Hosoi, "Optimal stroke patterns for purcell's three-link swimmer," *Phys. Rev. Lett.*, vol. 98, p. 068 105, 6 Feb. 2007 (cit. on p. 31).

[98] G. I. Taylor, "Analysis of the swimming of microscopic organisms," *Proc. R. Soc. Lond. A*, vol. 209, pp. 447–461, 1951 (cit. on p. 93).

[99] *The euglenoid project*. [Online]. Available: http://euglena.msu.edu/%20index.shtml (cit. on p. 19).

[100] V. Thomée, *Galerkin Finite Element Methods for Parabolic Problems*. Springer Series in Computational Mathematics, 2006, vol. 25 (cit. on pp. 27, 51, 54, 57, 61).

[101] A.-K. Tornberg and M. J. Shelley, "Simulating the dynamics and interactions of flexible fibers in stokes flows," *Journal of Computational Physics*, vol. 196, no. 1, pp. 8–40, 2004 (cit. on p. 65).

[102] M. F. Velho Rodrigues, M. Lisicki, and E. Lauga, "The bank of swimming organisms at the micron scale (boso-micro)," *PLOS ONE*, vol. 16, no. 6, pp. 1–80, Jun. 2021 (cit. on p. 93).

[103] B. J. Walker, K. Ishimoto, and E. A. Gaffney, "Efficient simulation of filament elastohydrodynamics in three dimensions," *Physical Review Fluids*, vol. 5, no. 12, p. 123 103, 2020 (cit. on pp. 66, 90, 91).

[104] B. J. Walker, S. Phuyal, K. Ishimoto, C.-K. Tung, and E. A. Gaffney, "Computer-assisted beat-pattern analysis and the flagellar waveforms of bovine spermatozoa," *R. Soc. Open Sci.*, vol. 7, no. 6, 2020 (cit. on p. 120).

[105] H. Wang, "Several issues in modeling molecular motors," *Journal of Computational and Theoretical Nanoscience*, vol. 5, no. 12, pp. 2311–2345, 2008 (cit. on p. 95).

[106] S. Wiggins, *Introduction to Applied Nonlinear Dynamical Systems and Chaos*. Springer, Texts in Applied Mathematics, 2003 (cit. on pp. 29, 107–109).

[107] L. G. Woodhams, Y. Shen, and P. V. Bayly, "Generation of ciliary beating by steady dynein activity: The effects of inter-filament coupling in multi-filament models," *Journal of The Royal Society Interface*, vol. 19, no. 192, p. 20 220 264, 2022 (cit. on p. 94).

[108] T. Yagi and R. Kamiya, "Novel mode of hyper-oscillation in the paralyzed axoneme of a chlamydomonas mutant lacking the central-pair microtubules," *Cell Motility*, vol. 31, no. 3, pp. 207–214, 1995 (cit. on p. 94).

[109] R. Yanagimachi, "The movement of golden hamster spermatozoa before and after capacitation," *Reproduction*, vol. 23, no. 1, pp. 193–196, 1970 (cit. on p. 91).

[110] Y.-N. Young, "Hydrodynamic interactions between two semiflexible inextensible filaments in stokes flow," *Physical Review E*, vol. 79, no. 4, p. 046 317, 2009 (cit. on p. 91).

[111] T. S. Yu, E. Lauga, and A. Hosoi, "Experimental investigations of elastic tail propulsion at low reynolds number," *Physics of Fluids*, vol. 18, no. 9, 2006 (cit. on p. 65).

ECOLE
DOCTORALE
DE MATHEMATIQUES
HADAMARD

Titre : Modèles de filaments pour la natation à l'échelle microscopique

Mots clés : Micro-nageurs, Equations aux dérivées partielles, Simulation numérique, Théorie du Contrôle

Résumé : Les mathématiques associées à la natation à l'échelle microscopique constituent un domaine de recherche actif depuis une quinzaine d'années, avec de nombreuses applications en biologie et en physique. En effet, les micro-organismes se déplaçant dans l'eau jouent un rôle crucial dans l'origine et le maintien de la vie, et les principes physiques régissant leurs mouvements diffèrent grandement de ceux qui gouvernent la natation humaine. Les recherches dans ce domaine peuvent aussi être appliquées à la conception de micro sous-marins, ouvrant la voie à des applications innovantes en médecine, comme la chirurgie non-invasive.
Cette thèse porte sur l'étude de tels micro-organismes, dans un contexte où les forces inertielles sont négligeables par rapport aux forces visqueuses dans le fluide environnant, phénomène caractérisé par un faible nombre de Reynolds.
Les deux premières parties traitent de modèles mathématiques de nageurs, composés de bras actifs, sphères, et ressorts passifs. Ces modèles permettent de contourner le théorème de la coquille Saint-Jacques de Purcell, qui garantit qu'un nageur dont la brassée est un mouvement réciproque ne pourra jamais se déplacer, car il revient toujours à sa position initiale en l'absence d'inertie. Le premier modèle conçu au cours de cette thèse est un nageur à quatre sphères avec deux bras élastiques passifs. Faire varier la fréquence d'oscillation du bras actif permet de changer le signe du déplacement du nageur, rendant le système contrôlable, tout en n'ayant qu'un seul degré de liberté actif. Le modèle étudié dans le deuxième chapitre comporte, quant à lui, un grand nombre de ressorts. Un modèle limite de ce nageur où le nombre de ressorts tend vers l'infini a ensuite été considéré, transformant le nageur en une queue élastique se compressant et s'étendant unidimensionnellement.
Au cours du troisième chapitre, on présente une preuve de la convergence et du caractère bien posé d'un modèle discret de micro-filament élastique à bas nombre de Reynolds. Ce modèle en trois dimensions est composé de N filaments rigides, dont le mouvement est en deux dimensions.
Enfin, dans le dernier chapitre, des modèles des mécanismes d'activation le long d'un flagelle sont présentés. Du point de vue de la biologie, ces mécanismes d'activation sont présents dans le flagelle dans une structure interne, appelée axonème, sous la forme de moteurs moléculaires arrangés en plusieurs rangées. En se basant sur un modèle de ces moteurs issu de la biophysique, deux nouveaux systèmes sont ensuite étudiés. Le premier représente une projection de l'axonème dans laquelle deux rangées de moteurs sont présentes, et est étudié aussi bien théoriquement que numériquement. Le second prend en compte la totalité des rangées de moteurs dans l'axonème, son comportement est illustré par des simulations numériques.

Title : Filament models for swimming at the microscopic scale

Keywords : Control theory, Numerical simulation, Partial differential equations, Micro-swimmers

Abstract : The mathematics associated with swimming at the microscopic scale has been an active research area for about fifteen years, with numerous applications in biology and physics. Indeed, microorganisms moving in water play a crucial role in the origin and maintenance of life, and the physical principles governing their movements differ greatly from those that govern human swimming. Research in this field can also be applied to the design of micro-robots, paving the way for innovative applications in medicine, such as non-invasive surgery.
This thesis deals with the study of such microorganisms in a context where inertial forces are negligible compared to viscous forces in the surrounding fluid, a phenomenon characterized by a low Reynolds number.
The first two parts present new mathematical models of swimmers, composed of active arms, spheres, and passive springs. These models circumvent Purcell's scallop theorem, which states that a swimmer doing a reciprocal stroke cannot move, as it always returns to its initial position in the absence of inertia. The first model developed in this thesis is a four-sphere swimmer with two passive elastic arms. By varying the oscillation frequency of the active arm, the direction of the swimmer's displacement can be changed, making the system controllable with only one active degree of freedom. The model studied in the second chapter involves a large number of springs. A limiting model of this swimmer, where the number of springs tends to infinity, was then considered, transforming the swimmer into an elastic tail that compresses and extends along one single dimension.
In the third chapter, a proof of the convergence and well-posedness of a discrete model of an elastic microfilament at low Reynolds numbers is presented. This model consists of N rigid filaments immersed in a fluid, studied in 3D and whose movement is in two dimensions.
Finally, in the last chapter, models of activation mechanisms along a flagellum are introduced. Biologically, these activation mechanisms exist in the flagellum in an internal structure called the axoneme, in the form of molecular motors arranged in several rows. Based on a model of these motors from biophysics, two new systems are then studied. The first one represents a projection of the axoneme with two rows of motors and is analyzed both theoretically and numerically. The second one takes into account all rows of motors in the axoneme; its behavior is illustrated by numerical simulations.

Institut Polytechnique de Paris
91120 Palaiseau, France